DETERMINATION OF MATERIAL CONSTITUTIVE EQUATION OF A BIOMEDICAL GRADE Ti6Al4V ALLOY FOR CROSS-WEDGE ROLLING

A Thesis Submitted to
the Graduate School of Engineering and Sciences of
İzmir Institute of Technology
in Partial Fulfillment of the Requirements for the Degree of

MASTER OF SCIENCE

in Material Science

by
Engin Kıranlı

September 2009
İZMİR

We approve the thesis of **Engin KIRANLI**

Prof. Mustafa GÜDEN
Supervisor

Assoc. Prof. Bülent YARDIMOĞLU
Committee Member

Assist. Prof. Selçuk SAATÇİ
Committee Member

29 September 2009

Prof. Mustafa GÜDEN
Head of the Department of
Material Science and Engineering

Assoc. Prof. Talat YALÇIN
Dean of the Graduate School of
Engineering and Sciences

ACKNOWLEDGEMENTS

First of all, I would like to thank my supervisor, Prof. Dr. Mustafa Güden, for his supervision, guidance, endless support, and encouragement throughout my thesis study.

I would like to express my grateful thanks to my co-supervisor Prof. Dr. Muhsin Çiftçioğlu, for his generous help and valuable comments during thesis study. I owe my thanks to Dynamic Test and Modelling laboratory staff.

I would like to thank my laboratory friends specially Ahmet Kaan Toksoy, Çağrı Ergönenç, Eren Dizlek, Metin Çakırcalı, Onur Kocatürk and Gözde Tunusoğlu for their sincere help and kindness during studies. I would like to thank my family for their motivation, support and endless encouragement, specially to my brother Deniz Kıranlı

Finally, I would like to thank the grant provided by TUBİTAK with the project number of 107M628.

ABSTRACT

DETERMINATION OF MATERIAL CONSTITUTIVE EQUATION OF A BIOMEDICAL GRADE Ti6Al4V ALLOY FOR CROSS-WEDGE ROLLING

In the present work, the JC flow stress and damage parameters of a biomedical grade Ti6Al4V alloy that contained very low levels of interstitial elements were determined for the modeling its deformation in the CWR process. The JC models were determined through quasi-static (10^{-3}-0.1 s^{-1}) and high strain rates (300-1000 s^{-1}) within the temperature range of 25-1150 ^{o}C. High strain rate tests were performed using both compression and tension SHPB testing devices. The damage model was determined using notched specimens of different stress triaxiality. The tested alloy flow stresses were found to increase with increasing strain rate for both compression and tension tests. This was proved that the alloy has a strain rate sensitive flow stress behavior. At increasing strain rates the failure strains in tension decreased. The reduced fracture strain was also confirmed by the microscopic observations. In statically tested samples the ductile fracture mode was composed of smaller but deeper dimples, while the dimples were observed to be shallow and larger in dynamically tested samples. The tensile fracture presumably started in α region and the β phase microscopically shown to deform plastically through the tensile axis. The compression failure mode of the alloy was found to be resulting from the shear band formation followed by the fracture of the shear band. High temperature test conducted at quasi-static strain rate showed that the stress values decreased greatly after about 800 ^{o}C due to $\alpha \rightarrow \beta$ transformation. Due to this two different JC material models valid between 25-600 ^{o}C and 800-1150 ^{o}C were developed. The determined JC parameters were found to be well agreed with the literature except the model obtained from the compression tests.

ÖZET

BİYOMEDİKAL Tİ6Al4V ALAŞIMININ ÇAPRAZ KAMA HADDELEME İŞLEMİ İÇİN MALZEME YAPISAL DENKLEMİNİN BELİRLENMESİ

Bu çalışmada, yüksek saflığa sahip biyomedikal Ti6Al4V alaşımının çapraz kama haddeleme sürecinin modellenmesi amacıyla JC akma gerilmeleri ve hasar parametreleri belirlenmiştir. Malzeme modelleri düşük (10^{-3}–0,1 s^{-1}) ve yüksek (300-1000 s^{-1}) deformasyon hızlarında ve 25 ve 1150 arasında değişen sıcaklıklar için belirlenmiştir. Yüksek hız deformasyon testleri basma ve çekme Split Hopkinson basınç barları kullanılarak yapılmıştır. Hasar parametrelerinin hesaplanmasında, farklı çapta çentikli numunelerin üç eksenli gerilme katsayıları kullanılmıştır.. Test edilen alaşımın akma stresinin artan deformasyon hızıyla basma ve çekme testlerinin her ikisinde de arttığı bulunmuştur. Bu sonuç alaşımın akma gerilmesinin deformasyon hızına bağlı davranış gösterdiğini kanıtlamıştır. Çekme testlerinde deformasyon hızının artması kırılma gerilmesinde düşmeye neden olmuştur. Kırılma gerilmesinde bu düşüş mikroskobik incelemeyle de doğrulanmıştır. Sünek kırılma gösteren malzemenin test edilmiş numune yüzeyleri incelendiğinde statik deformasyon hızlarında test edilen numunelerin yüzeyinde küçük ama derin çukurlar, dinamik deformasyon hızlarında test edilen numunelerin yüzeylerinde sığ ve geniş çukurlar oluştuğu gözlenmiştir. Çekme testi sonucu oluşan kırılmaların alfa fazında başladığı ve beta fazının da çekme yönü doğrultusunda plastik deformasyona uğradığı muhtemeldir. Basma testinde ise kırılmaların kesme bandlarının (shear band) oluşumu ve takip eden kesme bandlarının kırılmasıyla oluştuğu bulunmuştur. Statik deformasyon hızlarında yapılan yüksek sıcaklık testleri 800 ^{o}C den sonra $\alpha \rightarrow \beta$ faz değişimine bağlı olarak gerilme değerleri büyük düşüş göstermiştir. Bu nedenle 25-600 ^{o}C için ve 800-1150 ^{o}C arasındaki sıcaklıklar için iki farklı JC malzeme modeli oluşturulmuştur. Bulunan parametreler basma testi modeli hariç literatürdeki diğer model parametreleriyle tutarlıdır.

TABLE OF CONTENTS

LIST OF FIGURES

Figure **Page**

LIST OF TABLES

CHAPTER 1

INTRODUCTION

1.1. Cross Wedge Rolling

In the metal forming industry, it is important to produce high quality products in a relatively short time period for the increasing competitiveness arouse by the technological progress made within the several decades. The growing competitiveness unavoidably has motivated the researches to develop novel metal processing techniques. With the recent technological improvements, cross wedge rolling (CWR) metal forming technique, which was invented a century ago and started to be used industrially in 1949 (Dong, et al. 1998), has been greatly improved and emerged as an innovative metal forming technique for the manufactures. CWR differs from traditional metal forming techniques in several fundamental ways as will be elaborated in the next section.

1.1.1. Description of the Cross Wedge Rolling Process

In CWR, a cylindrical billet is deformed plastically into an axially symmetrical part by the action of wedge-shape dies moving tangentially relative to each other (Dong, et al. 1998). In this respect, it differs from the classical rolling and forging processes. Shafts with tapers, steps, shoulders and walls can be formed using CWR. There are several different types of CWR machines, but typical ones are composed of one to three rollers on which wedge-shaped tooling is mounted (Figure 1.1.). The most widely used CWR machines are the two and three-roll and flat wedge type configurations. For each machine configuration, the deformation process starts with the positioning of the preheated work-piece into the roller gap in the axial direction of the rollers. Then the work-piece sequentially deformed through four different zones of the toll; each stage corresponds to a part of the deformation step of the work-piece. The stages of the deformations are the knifing zone, guiding zone, stretching zone and sizing zone and sequentially shown in Figure 1.2.

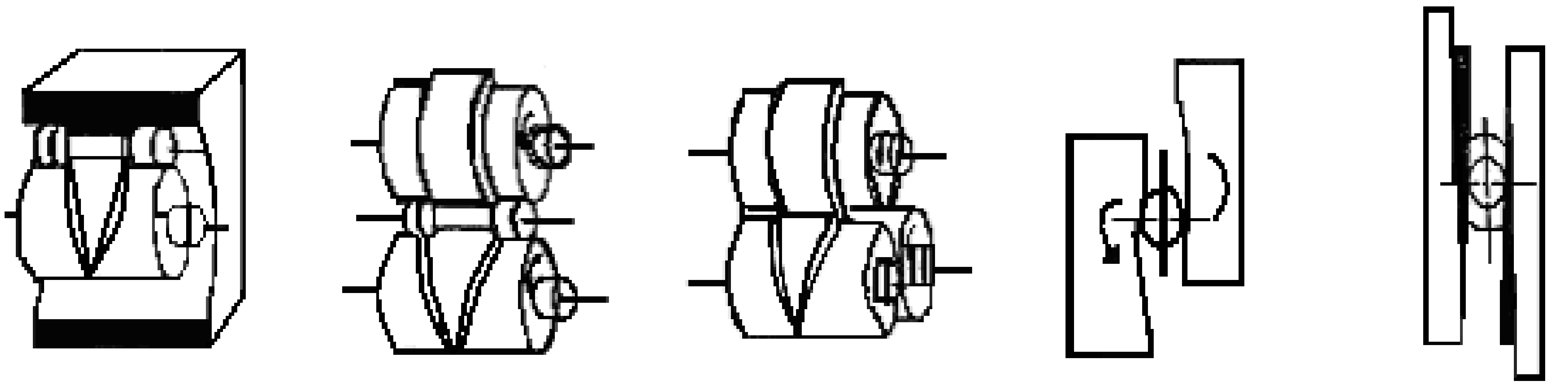

a)One-roll b)Two-roll c)Three-roll d)Concave Wedge e)Flat Wedge

Figure 1.1. Typical CWR machine configurations
(Source: Material Processing Technology 1998)

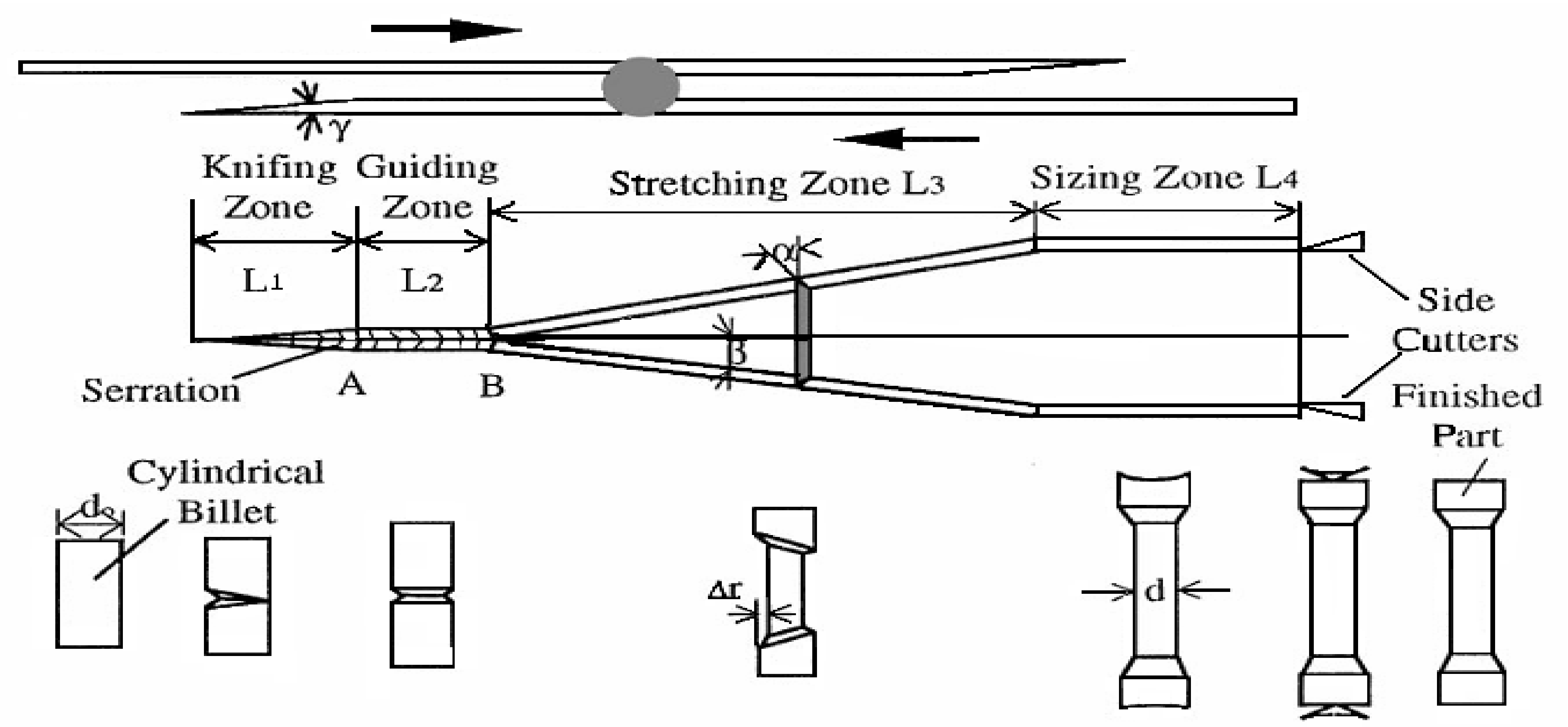

Figure 1.2. The zones of flat cross wedge rolling
(Source: Int. J. Adv. Manufacturing Technology 2007)

The work piece deformation starts with the knifing zone. Knifing zone comprises a wedge, whose height starts from zero and increases to the desired reduction of height (Δr). The main function of this part is to form a V-shaped slot over the surface of the work-piece. The angle of this V-shaped slot is determined with the forming angle (α) of the toll. The height reduction does not change in the following deformation steps. The other important role of the knifing zone is to drive the work-piece to the following deformation zones (Li and Lovell 2007). Following the knifing zone, the deformation process continues with the guiding zone. In this zone, the cross section and the forming angle of the tool does not change. V-shaped slot is enlarged and a uniform groove formed around the work-piece at the end of the guiding zone. The stretching zone is the most critical part in cross wedge tool geometry. Most of the plastic deformation of the work-piece takes place in this zone. The inclined surface of the wedge tool stretches the material to flow to the ends. The elongation and plastic deformation in the stretching zone are controlled by the stretching angle (β). As a result of this flow shoulders of the shafts are formed. In this zone, the symmetry of the contact area of the die and the work-piece is very important. Due to the asymmetric contact area, the problems with the radial and axial plastic flow of the work-piece may take place. The metal flow in the stretching zone becomes spiral as the work-piece rotates and this spiral may cause the failure of the work-piece (Dong, et al. 2000). Sizing zone is the last zone of the die. The surface quality and the uniform dimension of the work-piece are finely tuned in this zone. The cross-section of the tolls does not chance in this zone. The last part of the CWR machine is the side cutter which removes the excessive material from the end of the product.

1.1.2. Advantages of Cross Wedge Rolling

Some of the advantages CWR process as compared with traditional machining, forging and the other production methods may include the followings:

- Energy saving process; the process is efficient that it gives change to produce more parts in a short time.
- Higher productivity; the CWR process speed is 5 to 20 times faster than machining and forging. This provides higher productivity and also energy saving.
- Better environmental conditions; there are two important fundamental environmental benefits of CWR. First, the CWR mechanism does not require any oil or cooling lubricants. The second is the relatively low noise production during operation.

- Better product quality; in CWR process material achieves the desired shape by the plastic flow at elevated temperatures. The fabric of metal in CWR process continues so this also provides finer grain structure and hence stronger products.
- Higher material utilization; CWR reduces the cost of raw material as compared with the traditional techniques. In CWR, 10% of raw material is wasted but in other processes this goes up to 40%.
- Automation and lower cost; in CWR, all processes including surface refining, shape forming and end cutting are finished in a single step. This automation process provides reductions in the number of workers and the machine and the working area required for the production. As a result, the overall cost of the production decreases.

1.1.3. Failure Mechanisms in Cross Wedge Rolling

The failures in CWR are divided into three categories (Li and Lovell 2007): (i) improperly formed work-piece cross section, (ii) surface defects and (iii) internal defects. Improperly formed work-piece cross section (Figure 1.3(a)) results from the excessive slip between the work-piece and tools (Mackerle 2005). The tangential and normal forces acting on the work-piece provide the work-piece rotation between the tolls. The tangential and normal forces must be in equilibrium for the proper work-piece deformation. If the tangential force is greater than the normal forces, the rotation of the work-piece does not occur and the work-piece slips between the tool surfaces. Slip results in undesirable amount of work-piece deformation in wrong stages or undesired products can be produced (Li, et al. 2002). Surface defects are the second common defect types found in CWR process. These are the defects which include spiral groove, excessive thinning or excessive necking and overlapping of the work-piece (Figure1-3(b)). Spiral grooves in CWR occur due the formation of the cracks on the surface of the work-piece or large friction coefficient between the tool and the work-piece. The other type of surface defect knows as overlapping occurs because of the sharp forming angle (Li, et al. 2002). Internal defects such as cracks, voids (Figure1.3c) and cavities may form in CWR. The internal defects can results from large tensile stresses in the central portion of the work-piece, excessive shear stress during the knifing process and low cycle fatigue that develops during rolling process.

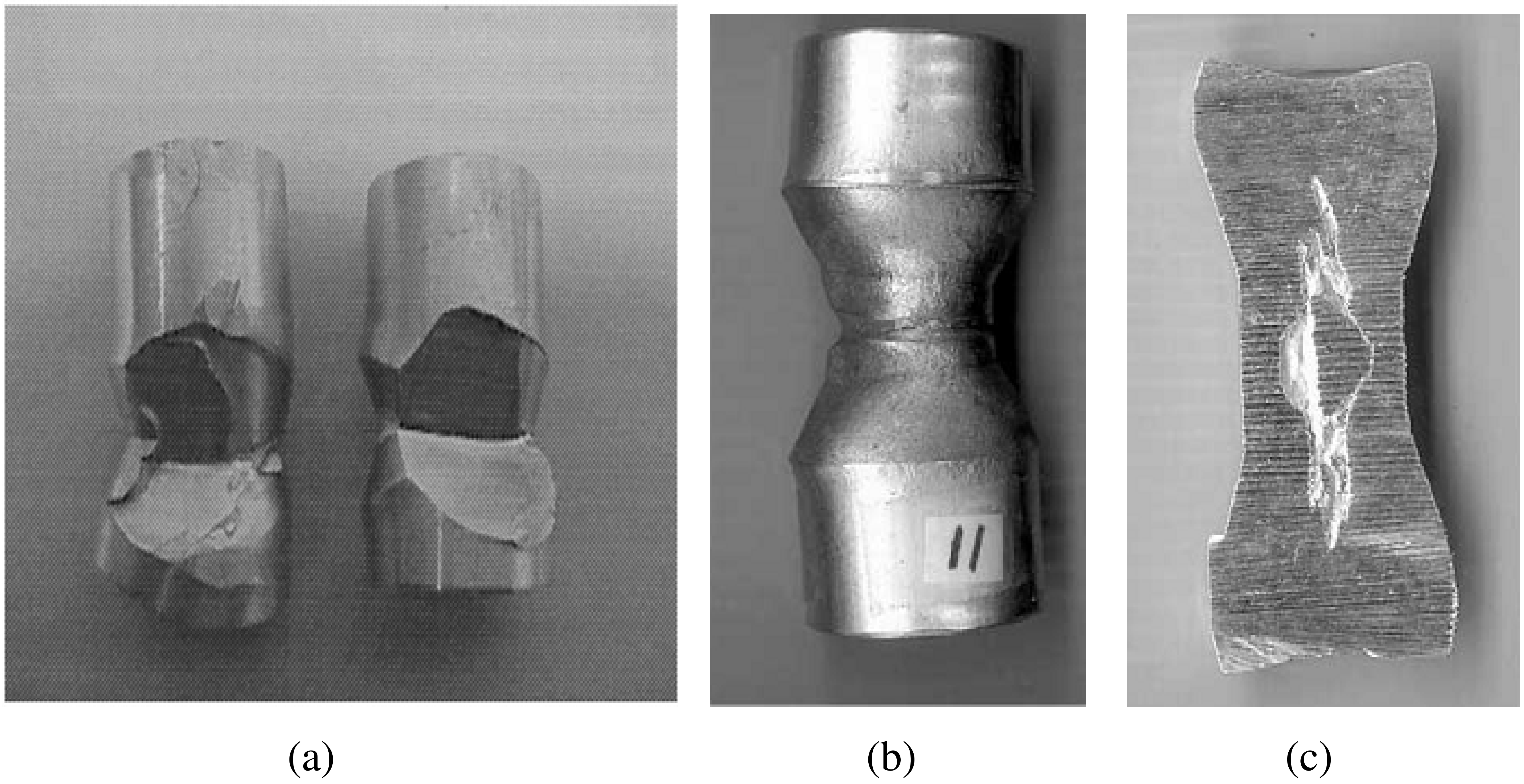

Figure 1.3. Typical defects in CWR process: (a) failed CRW work-piece due to excessive tool work-piece slip, (b) necking of the work-piece and (c) internal void formation in work-piece (Source: Journal of material processing Technology 1998-2002)

1.1.4. Numerical Models of Cross Wedge Rolling

Although CWR has attractive properties, it is not a widely used forming technique due to the less-known failure mechanisms involved in the production. CWR process has been recently subjected to experimental and numerical investigations in order to clarify the underlying mechanisms of the common failure modes of the process. Due to the complex production route of the CWR including the high strain rate plastic deformation, variable friction and high temperature, the prediction of the flow behavior of the work-piece during the process is difficult. The determination of the effects of the process parameters on the failure would significantly reduce the failure possibility of the product. For that, numerical models are excellent tools to analyze this complex production process.

Dong and his co-workers investigated an explicit finite element model of the flat wedge CWR process (Dong, et al. 1998). The model realistically characterized the interfacial slip that occurred during the real process. The important parameters of the knifing and guiding zones that caused the initial slip of the work-piece were found to include the friction coefficient, the forming angle, and the work-piece area reduction. Li and his co-workers studied a finite element model of two roll CWR process (Li, et al. 2001). With this model, the friction coefficient was shown to be the key parameter of the interfacial slip problem. The variations of global slip with forming angle, stretching angle, reduction area and forming velocity were also investigated in the same study. The results showed that the forming angle had the least influence in guiding and sizing zones and stretching angle was effective for global slip. The increase in the reduction area and forming velocity was found to increase the global slip. Dong and his co-workers investigated a finite element model of flat-wedge CWR process using the explicit finite element method (Dong, et al. 1998). It was shown that the numerical results agreed well with the experimental results. The slip between tool and work-piece was shown to increase during the forming process. Li and Lovell determined the void formation and growth mechanism in CWR process using an explicit finite element method (Li and Lovell 2004). It was shown that the effective plastic strain could be used as a criterion for predicting the internal failure in CWR. M. Wang developed a finite CWR model, in which the distributions of different field variables like strains, temperature and grain size of the work-piece in CWR were determined. Pater developed a complete model of the CWR process to determine the effects of process parameters on the process (Pater 2006). Also introduced a new method called wedge–rolls rolling and simulated the process with finite element method. The experimental and numerical results showed that it was possible to produce hollow parts using typical CWR toll. Dong and his co-workers analyzed numerically the stresses developed in CWR process (Dong, et al. 2000). The stress around internal cracks and voids were examined. It was shown that the central voids and cracks were formed due to the tensile stresses developed at the center of the work-piece. The results were also supported with experiments. Xuedao and his co-workers studied the rolling moment of the rolling mill in CWR and showed that the increase of stretching angle and rolled part size increased rolling moment, while the increase of the forming angle decreased the rolling moment (Xuedao, et al. 2007). Qiang and Song analyzed the temperature distribution on the work-piece in CWR using finite element model (Qiang and Song 2007). The contact heat conduction and plastic deformation heat determined as the main effects that changed the temperature distribution of the work-piece in the deformation zone.

CHAPTER 2

CONSTITUTIVE EQUATIONS

2.1. Applications of Constitutive Equations

Many engineering material applications occur at varying strain rates and temperatures. Examples included are the car crashes, bird impacts on aeronautic structures and engine materials exposed to extremely high temperatures. It is important to note that materials show different mechanical responses to the changing strain rates and temperatures and therefore they need to be tested at different strain rates and temperatures in order to predict their mechanical behavior. However, the testing materials at varying strain rates and temperatures are relatively expensive and time consuming; therefore, constitutive equations are developed to relate the behavior of materials as function of strain, strain rate and temperature. Constitutive equations are also main tools for the modeling of the complicated structures under structural loads.

An ideal constitutive equation should predict the material behavior at quasi-static ($1x10^{-3}$- 1 s^{-1}) and dynamic strain rates (>100 s^{-1}) at normal and elevated temperatures. Table 2.1 lists the widely applied constitutive equations together with the parameters used in these models. The constitutive equations, developed by Johnson and Cook (Lesuer 2000) and known as Johnson and Cook (JC) model, is however one of the widely used models in the simulations of high strain rate deformation. JC model is a semi empirical model and relatively easy to determine.

Table 2.1. Types of the constitutive equations
(Source: Encyclopedia of Materials)

Author(s)	**Equation**	**Parameters**
Ludwik (1909)	$\sigma = \sigma_0 + \mathrm{K}\varepsilon^{\mathrm{n}}$	$\sigma_0, K, n = \ constants$
Holloman (1945)	$\sigma = \ \mathrm{K}\varepsilon^{\mathrm{n}}$	$K, n = \ constants$
Swift (1952)	$\sigma = K(\varepsilon_1 + \varepsilon)^n$	$K, n = \ constants$ $\varepsilon_1 = predeformation$
Voce (1948)	$\sigma = \sigma_0 - (\sigma_0 - \sigma_1)\exp\,(-n\varepsilon)$	$\sigma_0, \sigma_1, n = constant$
Tome et al (1984)	$\sigma = \sigma_0 + (\sigma_1 + \theta_1\varepsilon)(1 - \exp\left(\frac{\theta_0\varepsilon}{\sigma_1}\right))$	$\sigma_0 = yield\ stress$ $\sigma_1 = \frac{d\sigma}{d\varepsilon} = constant$ $\theta_0\ and\ \theta_1 = workhard.\ coef.$
Ludwingson (1971)	$\sigma = K_1\varepsilon^{n_1} + \exp\,(K_2 + n_2\varepsilon)$	$K_1, K_2, n_1, n_2 = constants$
Gladman et al. (1970)	$\sigma = \sigma_0 + K_1 \ln\varepsilon + K_2\varepsilon$	$\sigma_0, K_1, K_2 = constants$
El-Magd and Troost (1997)	$\sigma = K\varepsilon^n\left(\frac{\dot{\varepsilon}}{\dot{\varepsilon_0}}\right)^m$	$K, n, m, \dot{\varepsilon_0} = constants$
El-Magd (1997)	$\sigma = [K_1(K_2 + \varepsilon)^n + \eta\dot{\varepsilon}]\exp\,(-\frac{\beta(T - T_0)}{T_m})$	$K_1, K_2, n, \eta, \beta = constants$
Reiff et al. (1986)	$\sigma = \left[K_1 + K_2\left(\frac{\dot{\varepsilon}}{\varepsilon}\right)^{\frac{1}{m}} + K_3\sqrt{\varepsilon}\right]$	$K_1, K_2, K_3, m = constants$
Johnson and Cook (1983)	$\sigma = [A + B\varepsilon^n]\left[1 + C\ln\frac{\dot{\varepsilon}}{\dot{\varepsilon}_0}\right][1 - (T^*)^m]$	A, B, n, C, m=constant
Cowper Symond	$\sigma_y = \left[\sigma_0 + \beta E_P\varepsilon_{eff}^P\right]\left[1 + \left(\frac{\dot{\varepsilon}_p}{D}\right)^{1/P}\right]$	$D, P = constants$ $\sigma_y = initial\ yield\ strength$ $E_p = plastic\ hardening\ modulus$
Zerilli and Armstrong (1987)	$\sigma = \sigma_0 + K_1\left(\frac{\dot{\varepsilon}_0}{\dot{\varepsilon}}\right)^{-K_3T} + \frac{K_2}{e^{-K_4T}}\varepsilon^n + K_5d^{-\frac{1}{2}}$	$\sigma_0, K_1, K_2, K_3, K_4, K_5, n, \dot{\varepsilon}_0 = const.$

2.1.1. Johnson-Cook Model

JC model uses simple forms of empirical relations of stress with strain, strain rate and temperature in the form of,

$$\sigma = \sigma_o + K\varepsilon^n \tag{2.1}$$

$$\sigma = \sigma_r \left[1 - \left(\frac{T - T_r}{T_m - T_r} \right)^m \right] \tag{2.2}$$

$$\sigma \propto \ln \dot{\varepsilon}$$

$$\sigma = [A + B\varepsilon^n][1 + C\ln(\frac{\dot{\varepsilon}}{\dot{\varepsilon}_o})][1 - (T^*)^m] \tag{2.3}$$

where, A, B, n, C and m are constants, $\dot{\varepsilon}_o$ is the reference strain rate and T^* may be expressed as

$$T^* = \frac{(T - T_r)}{(T_M - T_r)} \tag{2.4}$$

in which, r and M refer to reference and melting temperatures. The first bracket in Equation 2.3 gives the isothermal stress as a function of strain for $\dot{\varepsilon}_o = 1\ s^{-1}$ (reference strain rate for convenience). The second bracket includes the strain rate effect and the last bracket accounts for the thermal effects. The constants A, B and n can be extracted from the stress strain curve obtained at quasi-static strain rates (assuming isothermal conditions exist) at reference strain rate (usually taken as 1 s^{-1}). The determination of the constants depends on the combination of data in specific conditions and processing it on the suitable graphics. At least 3 equivalent flow stress-strain curves are needed to form the model: one quasi-static and isothermal and two at different strain rates. For temperature term calculation, one more additional curve is needed at a high temperature (Jutras 2008).

In high strain rate testing, the effect of heating due to plastic deformation of the material should be also taken into account. The heating due to high strain rate is also called thermal softening phenomenon. For most of materials, about 90% of the plastic deformation is dissipated as heat in the material (Jutras 2008). This increase in temperature can be calculated using the following equation,

$$\Delta \mathrm{T} = \frac{\alpha}{\rho c} \int \sigma(\varepsilon) d\varepsilon \tag{2.5}$$

where, ΔT is the temperature increase, α is the percentage of the plastic deformation transformed to heat, c is the heat capacity and ρ is the density .

2.1.2. Johnson-Cook Damage Model

JC damage model relates the fracture strain with strain rate, temperature and pressure. The model takes into account the loading history which is represented by the strain to fracture. The derivation of the JC damage law starts with the following fracture law;

$$\mathrm{D} = \sum \frac{\Delta\varepsilon}{\varepsilon_f} \tag{2.6}$$

where, $\Delta\varepsilon$ is the increment in plastic strain and ε_f is the strain to fracture under current conditions. Fracture occurs when D≥1.0 and for an element ε_f is

$$\varepsilon^f = [D_1 + D_2 exp D_3 \sigma^*][1 + D_4 \ln \dot{\varepsilon}^*][1 + D_5 T^*] \tag{2.7}$$

$$D_1, D_2, D_3 = triaxial\ stress\ state\ parameters$$

$$D_4 = strain\ rate\ parameter$$

$$D_5 = high\ temperature\ parameter$$

$$\sigma^* = \frac{\sigma_H}{\sigma_{eq}}$$

This general expression is valid for constant values of σ^*,$T^*$and where $\sigma^* \leq 1.5$.

At least three tests are needed to determine the parameters of JC damage model. Specimens having different notch radius were used to determine the fracture strain (Bao 2004). For the determination of D_1, D_2 and D_3, tests must be done under quasi-static and isothermal conditions. Data gathered from the test are used to draw the strain to failure as a function of triaxial state of stress (Jutras 2008, Johnson 1991). The evolution of state of stress during a tensile test should be determined because the notch radius changes during the test also. It is difficult to measure it during the test or analytically calculate. One way is to record the test specimen deformation and calculate the notch radius using an image system. The image system must be able to make precise measurements on the images and can compute the deformation of the specimen during the test (Jutras 2008). After obtaining the triaxial state of stress for each test, the fracture strain versus triaxial ratio graph is used to determine parameters D_1, D_2 and D_3. However, high strain rate tests at different strain rates are needed to obtain D_4 (strain rate parameter). Data from high strain rate tests are combined with the quasi-static test results and the strain rate versus strain to fracture graph are drawn in natural semi-log graph. Then the equation fitted to the curve to determine the value of D_4 (Jutras 2008). With the same strategy the parameter D_5 was obtained with result of the tests done at different temperatures. In this case, strain to fracture vs. temperature graph gives the value of D_5 (Jutras 2008).

CHAPTER 3

TESTING METHODS FOR CONSTITUTIVE RELATIONS

3.1. Testing Methods

The types of the tests chosen for mechanical testing depend on the desired response of the tested material. Testing methods commonly used at different strain rate regimes to determine mechanical properties. Creep and quasi-static tests are usually conducted with the constant cross-head speed testing machines in the strain rate regime of 10^{-5} s^{-1}. At increasing strain rates, >100 s^{-1} various types of testing methods can be used to test the materials; however, among them only Split Hopkinson Bar (SHB) method gives material stress-strain and strain behavior in a single test. This method is also based on the equilibrium deformation of the material and therefore the inertial effects are excluded in the test.

3.1.1. Quasi-static tests

3.1.1.1. Tension test

Tension test is one of the most widely used methods of testing materials at quasi-static strain rates. It is a simple test and provides important information about the tested material mechanical properties. The dimensions and the shape of the test specimen and the testing procedure are defined by the ASTM (American Society for Testing and Materials) standards. In tension test, the specimen is mounted on the grips of the tension test machine and elongated at a constant rate. During the test the applied load and the elongation of the specimen are recorded concurrently. The elongation measurements may also be made using video or mechanical extensometers. At the end of the test force versus elongation data are obtained and using the following formulations, engineering stress-strain response of the material can be calculated.

$$\text{engineering stress} = \sigma_{\text{eng}} = \frac{\text{P}}{\text{A}_0} \tag{3.1}$$

and

$$\text{engineering strain} = \varepsilon_{\text{eng}} = \frac{\text{l}_\text{f} - \text{l}_0}{\text{l}_0} \tag{3.2}$$

where, P is the load, A_0 is the initial cross section, l_f is the final gage length and l_0 is is the initial length. The true stress and strain are calculated using

$$\text{true stress} = \sigma_{\text{true}} = \frac{\text{P}}{\text{A}_\text{i}} \tag{3.3}$$

and.

$$\text{true strain} = \ln \frac{\text{l}_\text{f}}{\text{l}_0} \tag{3.4}$$

where, A_i is the instantenous cross section area. True stress-strain can be further related with engineering stress-strain by considering the plastic deformation as a constant volume process as

$$A_1 l_1 = A_2 l_2 = constant$$

where, $A_1$and A_2 are the initial and final cross sections and l_1 and l_2 are the initial and final length respectively. By using the constant volume relation the following true stress-strain relations can be easily obtained as,

$$\sigma_{\text{true}} = \sigma_{\text{eng}}(1 + \epsilon_{\text{eng}}) \tag{3.5}$$

and

$$\epsilon_{true} = \ln\,(\epsilon_{eng} + 1) \tag{3.6}$$

Above equations are valid until ultimate tensile strength (UTS) at which the inhomogeneous deformation of the sample starts (necking) (Figure 3.1.).

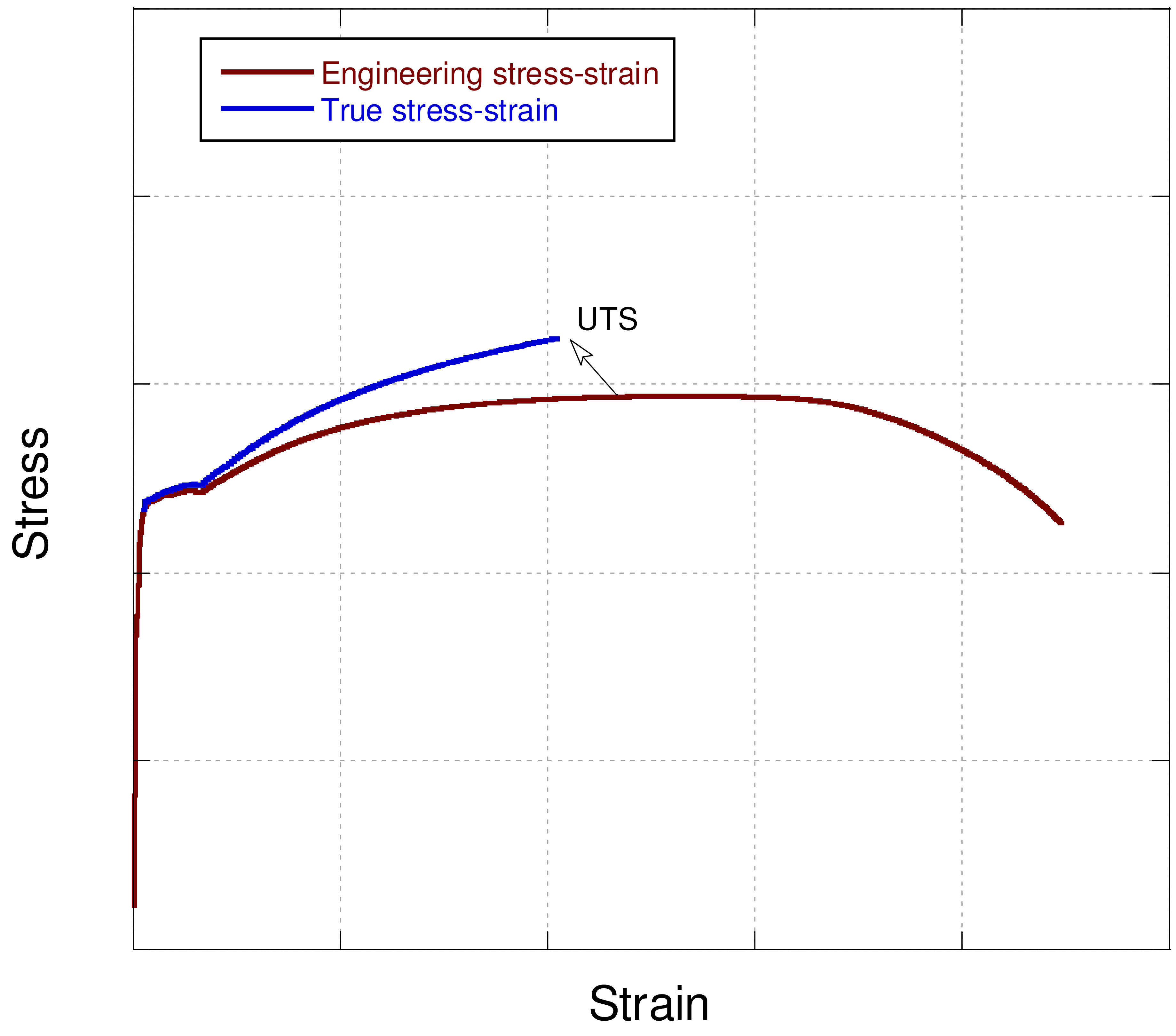

Figure 3.1. Comparison of true and engineering stress-strain curve of a material

Engineering stress-strain curves are divided/considered in two regions: elastic and plastic region. In elastic region, the stress and strain is linearly proportional to each other. The deformation in this part is irreversible in that when the load is removed, the specimen turns into its original dimensions. Elastic modulus (Young's modulus: E) of the material is determined from the slope of the stress-strain curve in the elastic region as

$$E = \frac{\sigma}{\varepsilon} \tag{3.7}$$

The point at which the plastic deformation ends is called the yielding point and the stress corresponding to the point is called yield strength. Alternative way of determining the yield strength is to draw a straight line parallel to the curve which starts from 0.2% strain. The point at which the straight line intersects the stress-strain curve is called yield strength. Ultimate tensile strength is the maximum stress that engineering stress-strain curve reaches.

3.1.2. Bridgman Correction

The data obtained in the stress-strain curve just after the necking in a tension test cannot be used to calculate true stress and true strain values using Equation 3.5 and 3.6 due to the stress localization resulting in deterioration of the uniaxial state of stress. That is, with the formation of necking, the uniaxial state of stress turns into triaxial state of stress. In order to obtain the uniaxial true strain-stress data after necking the stress values are corrected with a factor known as Bridgman Correction factor.

The equivalent stress which is also called as von Misses stress can be defined for any given stress state as;

$$\mathrm{\sigma_{eq}} = \frac{1}{\sqrt{2}}\left[\left(\mathrm{\sigma_x} - \mathrm{\sigma_y}\right)^2 + \left(\mathrm{\sigma_y} - \mathrm{\sigma_z}\right)^2 + (\mathrm{\sigma_z} - \mathrm{\sigma_x})^2 + \left({\mathrm{\tau_{xy}}}^2 + {\mathrm{\tau_{yz}}}^2 + {\mathrm{\tau_{zx}}}^2\right)\right]^{1/2} \quad (3.8)$$

During the development of Bridgman correction, it is assumed that the strain distribution in the minimum section (see Figure 3.2.) is,

$$\epsilon_\mathrm{r} = \epsilon_\mathrm{t} = -\frac{\epsilon_\mathrm{a}}{2} \quad (3.9)$$

where, ϵ_r is the radial strain, ϵ_t is the hoop strain and ϵ_a is the axial strain as shown in Figure 3.2. The deformation in the grid line after necking is given as;

$$\frac{1}{\mathrm{\rho}} = \frac{\mathrm{r}}{\mathrm{aR}} \quad (3.10)$$

where, ρ is the grid line curvature, r is the radius of actual cross section, a is the radius of smallest cross section and R is the radius of curvature at the neck (Figure 3.2.).

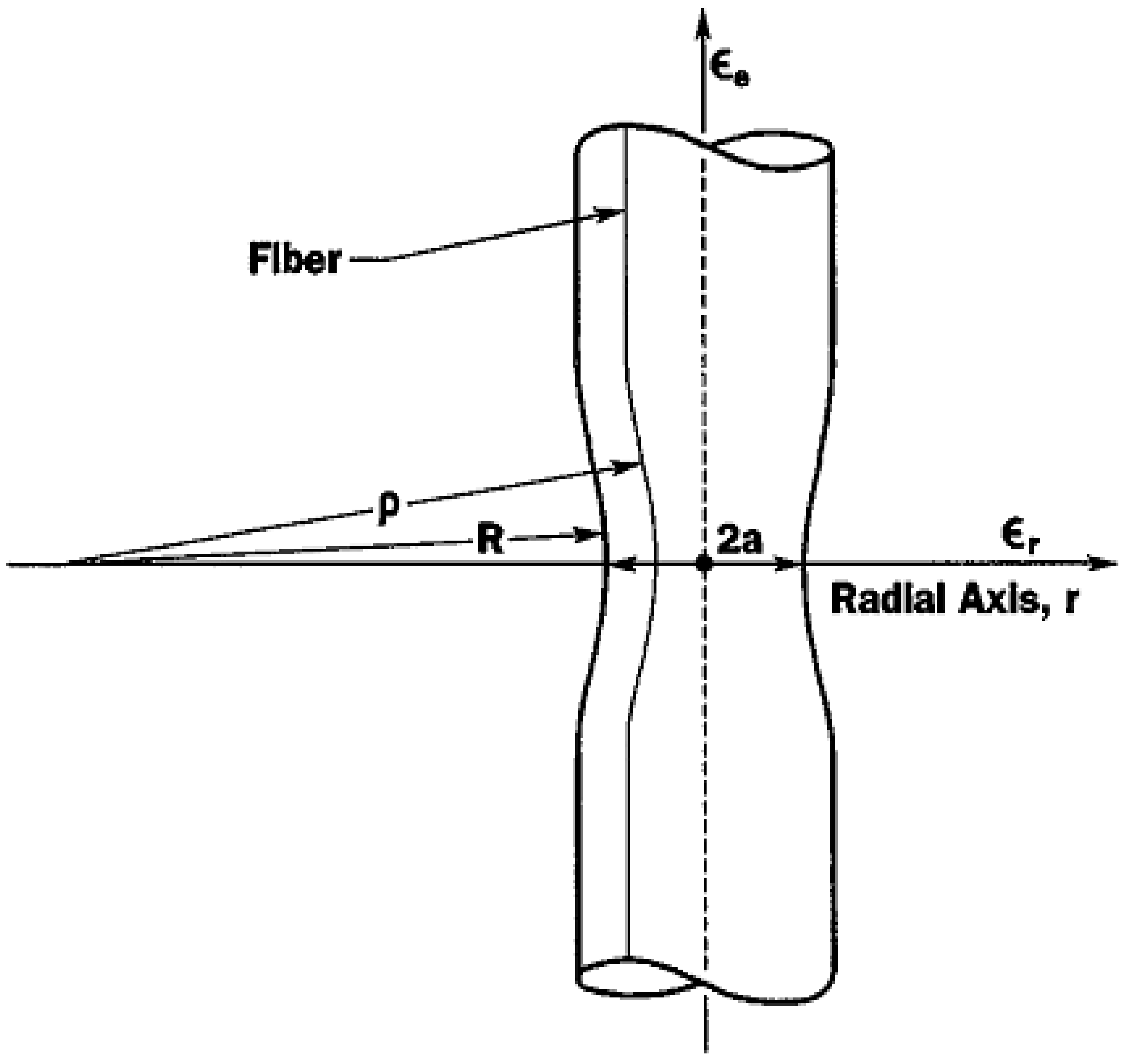

Figure 3.2. Rod specimen after necking
(Source: AMP Journal of Technology 1996)

Bridgman assumed the ratios of the principal stresses remained constant during loading for the calculation of the correction factor. Based on this assumption the equivalent uniaxial strain is defined as;

$$\epsilon_e = \int_{L_0}^{L_a} d\,\epsilon_a = \epsilon_a = \ln\frac{A_0}{A} \tag{3.11}$$

Equation 3.11 relates the equivalent strain with instantaneous dimension measurements of minimum cross section. The average axial stress at the smallest cross section is,

$$(\sigma_\mathrm{a})_\mathrm{av} = \frac{\mathrm{F}}{\mathrm{A}} \tag{3.12}$$

Note that due to the stress triaxility at the neck the hoop and the radial stresses are not zero. As a result, the stress at the neck is different from the equivalent uniaxial stress. By using Bridgman assumptions and the stress equilibrium equation, we defined stress distribution at the smallest cross section as;

$$\sigma_r = \sigma_t = \frac{(\sigma_a)_{av}}{\left(1+\frac{2R}{a}\right)}\left\{\frac{\ln\left(\frac{a^2+2aR-r^2}{2aR}\right)}{\ln\left(1+\frac{a}{2}\right)}\right\} \tag{3.13}$$

and

$$\sigma_a = \frac{(\sigma_a)_{av}}{\left(1+\frac{2R}{a}\right)}\left\{\frac{1+\ln\left(\frac{a^2+2aR-r^2}{2aR}\right)}{\ln\left(1+\frac{a}{2R}\right)}\right\} \tag{3.14}$$

Then, the equivalent uniaxial stress is,

$$\sigma_e = \frac{(\sigma_a)_{av}}{\left(1+\frac{2R}{a}\right)\ln\left(1+\frac{a}{2R}\right)} \tag{3.15}$$

In Equation 3.15., the correction factor (k) is defined as

$$k = \left[\left(1+\frac{2R}{a}\right)\ln\left(1+\frac{a}{2R}\right)\right]^{-1} \tag{3.16}$$

Due to the difficulty in stress measurement after necking, the correction factor with the experimental results cannot be verified directly. But the correction factor can be confirmed by verifying the assumptions that it depends on. With the measured a and R values, Bridgman correction formulation gives the consistent results (Ling 1996). The values of a and R are usually measured during the test by stopping and measuring manually or using a camera system that gives opportunity to measure it from the photographs.

The notched specimens such as shown in Figure 2.4 are usually used to determine the relation between stress triaxility and failure strain. By increasing the variety of notch radius the triaxiality dependency of the failure strain can also be determined. Stress triaxiality is important in damage models and given by the following normalized form,

$$\frac{\sigma_h}{\sigma_{eq}} = \frac{1}{3} + \ln\left(1+\frac{a}{2R}\right) \tag{3.17}$$

The mean stress is

$$\sigma_h = \left(\frac{\sigma_1+\sigma_2+\sigma_3}{3}\right) \tag{3.18}$$

and equivalent stress in terms of principle stresses is,

$$\sigma_{\mathrm{eq}} = \sqrt{\frac{1}{2}(\sigma_1 - \sigma_2)^2 + (\sigma_2 - \sigma_3)^2 + (\sigma_3 - \sigma_1)^2} \tag{3.19}$$

where σ_1, σ_2 and σ_3 are the principal stresses.

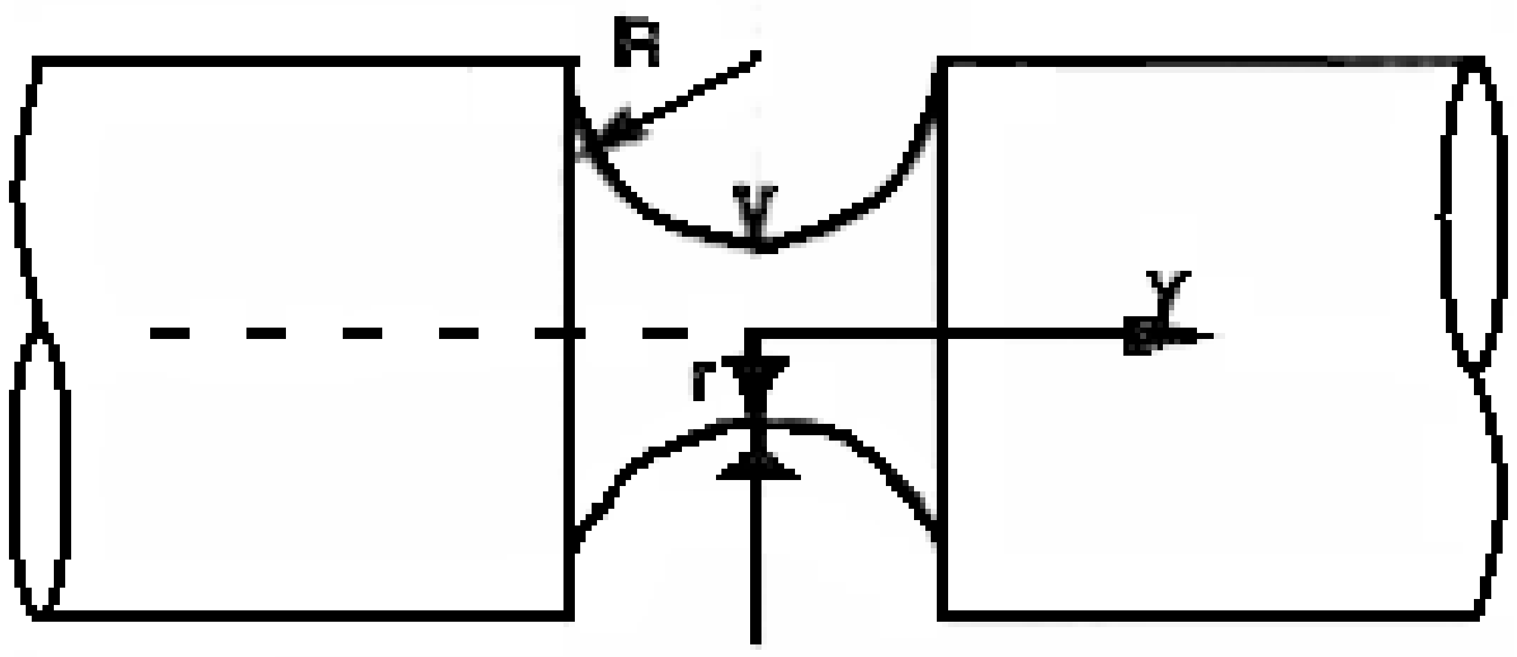

Figure 3.3. Notch tension test specimen

3.1.3. Compression Test

Compression tests are preferred in large permanent deformations such as forging and extrusion (Callister 2003). In compression test, the applied force is in the opposite direction of the force in tensile test and the length of the specimen decreases with an increase in diameter. The stress-strain curves of the tension and compression tests are very much similar until about the yield point for the ductile materials. After yielding stress strain curves of the same material show different behaviors due to the flattening of the compression specimen. Flattening increases the resistance of the material to stress and causes an increase on the stress-strain curve. When ductile materials compressed a barrel shape of the specimen occurs (Liechti 2003). Barreling is an important problem in compression and occurs as result of the friction between specimen and the surface of the dies. Lubricant usage between the specimen-die surfaces can decrease the friction.

3.2. High Strain Rate Testing

3.2.1. Split Hopkinson Bar: Historical Review

High strain rate tests are essential for the modeling and analyzing material behavior at increasing strain rates. High strain rate data for the constitutive equations are further needed particularly in applications where the deformation rates are far greater than quasi-static strain rates. SHB is one the most widely used methods of testing materials at increasingly high strain rates within the strain rate regime of 100-10000s^{-1} (Bariani, et al. 2001).

In 1913, Bertram Hopkinson introduced a technique to measure the peak pressure developed during a high strain rate deformation event. This technique was shortly based on the measuring the momentum trapped by a specimen which flied as a result of tension wave passage on a steel rod. The testing system was composed of a long steel rod, a steel specimen and a ballistic pendulum. A compression wave was created from one side of the rod. This wave passed through the rod and reached the specimen-bar interface. The specimen was fixed to the bar by grease and therefore sustained compressive loads. The tension wave reflected from the end of the specimen however flied off the specimen from the end. The specimen momentum was measured by means of a pendulum. The time of the momentum acting was equal to the time at which the wave passed through the specimen. The peak pressure was measured by the momentum measurement. Hopkinson made series of tests with using different specimens and was able to measure the peak pressures developed and the wave velocities of different specimens. However, the pressure time relations could not be determined in these experiments at those times.

Pochhammer developed wave speed dependencies on frequency in solids (Pochhammer 1876). Later, in 1941, these equations were solved by Dennisson Bancroft (Bancroft 1941). Although, Bancroft did not study directly Hopkinson Pressure Bar testing apparatus, his solutions of wave velocity of longitudinal waves in cylindrical bar were considered as the basis of the Hopkinson Pressure Bar experiments. In 1948, Davies developed a novel technique for measuring the strain on the bars using condensers. With this new method, the displacement-time and pressure-time relations were precisely determined. A further development occurred in 1949 when Kolsky added a second pressure bar to the original Hopkinson Pressure Bar testing system. In Kolsky's new design the specimen was sandwiched between two bars and the compressive wave passed through the second bar, while the specimen deformed between the bars. With this improvement, Kolsky was able to calculate the strain, stress and strain rate for the deformed specimen. This new version of Hopkinson Pressure Bar was called Split Hopkinson Pressure Bar (SHPB) or Kolsky's bar. Since, the strain, stress and strain rate are measured directly from the bars or calculated using the related equations, Split Hopkinson Pressure Bar has become a popular testing method for high strain rate testing. Following Kolsky, Lindholm and Yeakly, Gorham and Wu and Bertholf and Karnes made further contributions for the improvement of the SHPB technique (Lindholm and Yeakley 1968, Gorham 1996, Bertholf 1975). In 1954, Krafft for the first times used mounted strain gages to measure the strains from the bars of SHPB test device (Tasneem 2002). Novel improvements has also made in SHPB with the recent technological improvements. The use of the digital oscilloscopes and computers has improved the SHPB test technique significantly. Technological progresses have provided more accurate and precise measurements in SHPB technique (Tasneem 2002).

3.2.2. SHPB Apparatus

The SHPB testing apparatus shown in the Figure 3-3 consists of 3 parts

- Gun Assemble
- Bars (striker, incident, transmitted bars)
- Electronic measurement system

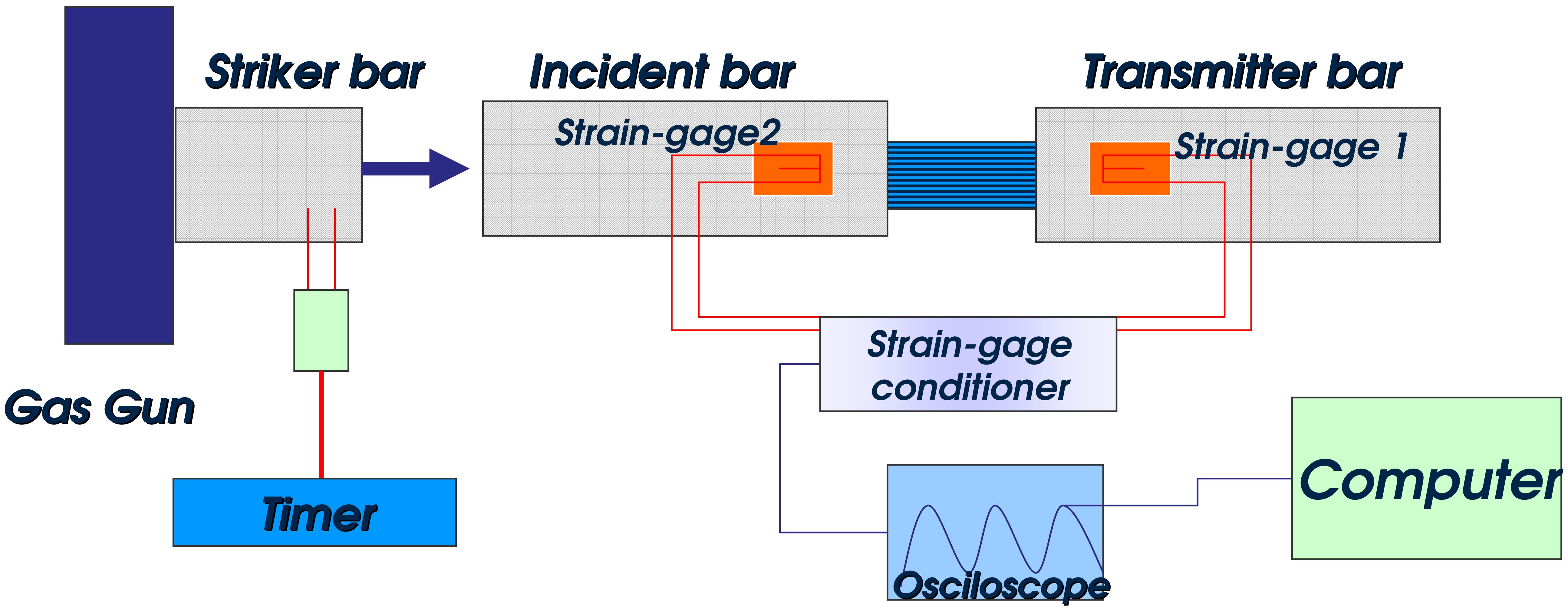

Figure 3.4. Schematic view of the Split Hopkinson Pressure Bar

Pressure gun is the part which fires the striker bar to incident bar with a initial velocity, v_o. Striker bar impact to end of the incident bar forms a compressive wave in the incident bar. The amplitude of the wave created is directly related with the speed of the striker bar. This wave propagates through the incident bar until the specimen bar interface. At the specimen bar interface, a part of the wave transmitted to the specimen and other part is reflected back. Incident and reflected strains are measured by the gage on the incident bar, transmitted strain is measured by the gage on the transmitter bar. These gages are connected to the strain gage conditioner in which the voltage signal is amplified. Oscilloscope in the measurement system is used to monitor and store the strain data.

3.2.3. SHPB Apparatus principles

When a long bar having a velocity of v_o strikes another long bar at rest and having the same elastic modulus and diameter as the impact bar, a rectangular elastic stress pulse is produced in the impacted bar. The magnitude of stress and strain in the impacted bar are direct functions of the velocity of the striking bar, modulus (*E*) and elastic wave velocity (*c*) of the impacted bar. The maximum stress (σ) and the maximum strain (□) in the bar are given as follows:

$$\sigma_b = \frac{E_b V_0}{2C_b} \tag{3.20}$$

and

$$\varepsilon_b = \frac{\sigma_b}{E_b} = \frac{V_0}{2C_b} \tag{3.21}$$

The total time period in which the incident pulse operates is called the time window (T_w) and given as

$$T_w = \frac{2L_{SB}}{C_b} \tag{3.22}$$

where, L_{SB} is the striker bar length. The displacements of the incident and transmitter bars, U_1 and $u2$ shown in Figure 2 can be found using the following equations,

$$\begin{gathered} U_1 = C_b \int_0^t (-\varepsilon_i + \varepsilon_r) d\tau \\ U_2 = -C_b \int_0^t \varepsilon_t d\tau \end{gathered} \tag{3.23}$$

where i, r and t refer to incident, reflected and transmitted waves, respectively. The strain in the specimen is then,

$$\varepsilon_s = \frac{U_2 - U_1}{L_s} = \frac{C_0}{L_s} \int_0^t (\varepsilon_t + \varepsilon_i - \varepsilon_r)\, d\tau \tag{3.24}$$

where, L is the length and s refers to the specimen. The loads on each interface, incident bar/specimen (1) and specimen/transmitter bar (2), are

$$\begin{gathered} P_1 = A_b E_b (\varepsilon_i + \varepsilon_r) \\ P_2 = A_b E_b \varepsilon_t \end{gathered} \tag{3.25}$$

It is assumed that the wave propagation effect in the small sample may be neglected, so that $P_1 = P_2$. Therefore, strain and strain rate equations can be written as

$$\varepsilon_s = \frac{-2C_b}{L_s} \int_0^t \varepsilon_r d\tau$$

$$\dot{\varepsilon}_s = \frac{-2C_b}{L_s}\varepsilon_r \tag{3.26}$$

Accordingly, the stress in the specimen is

$$\sigma_s = \frac{P_1}{A_s} = \frac{P_2}{A_s} = \frac{A_b}{A_s}E_b\varepsilon_t = \frac{A_b}{A_s}E_b(\varepsilon_i + \varepsilon_r) \tag{3.27}$$

Typical strain gage readings from SHPB test and the resultant stress-strain and strain rate curves are shown in Figure 3.6 (a) and (b), respectively.

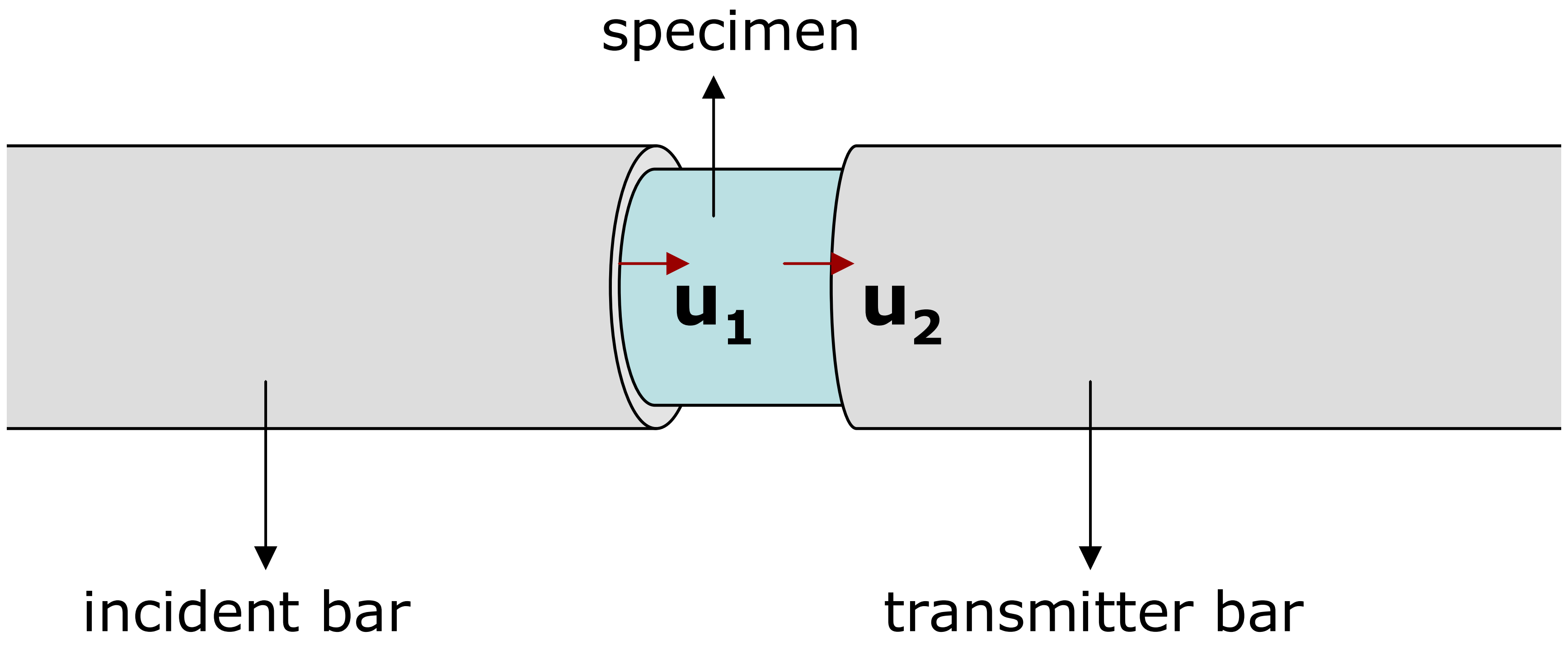

Figure 3.5. Incident-transmitter bar

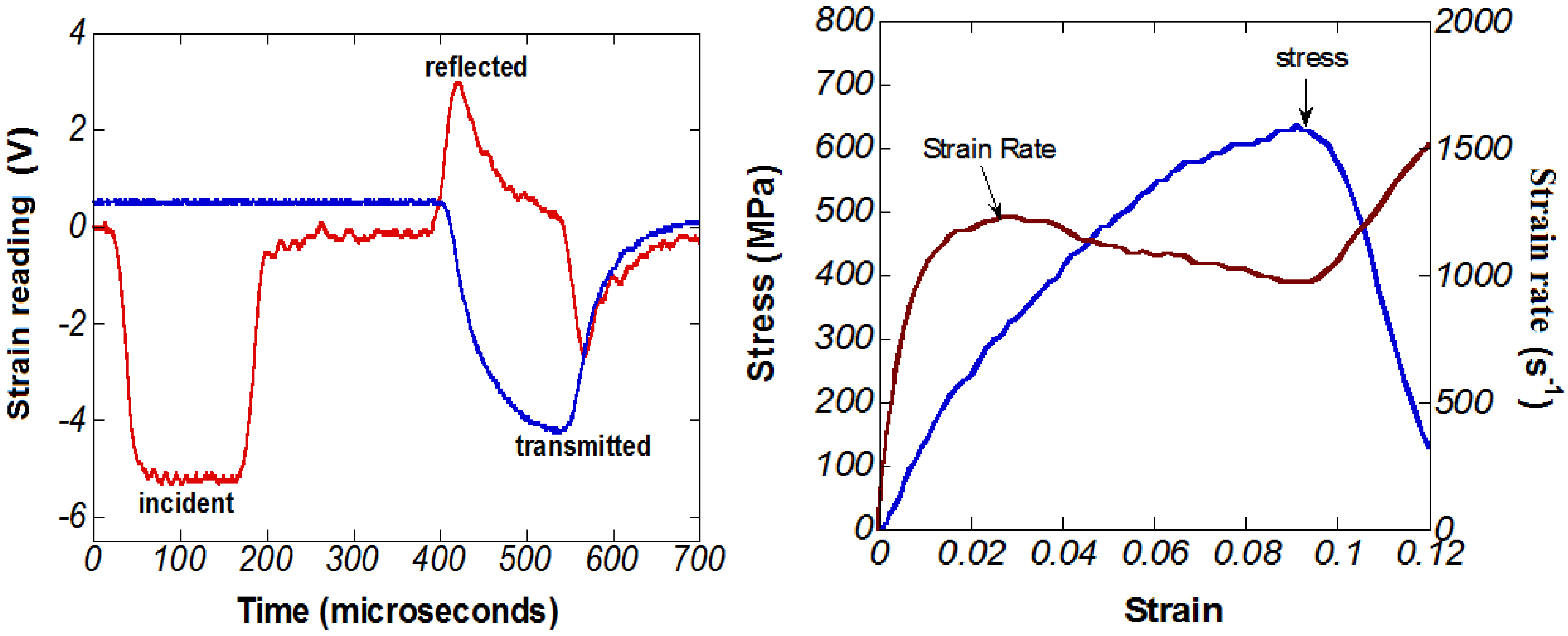

(a) (b)

Figure 3.6. (a) Strain readings from a SHPB testing and (b) Calculated stress and strain rate variation with strain in the specimen

3.2.4. Split Hopkinson Tension bar

In 1968 Lindholm & Yeakley used a hollow tube output bar at the end of incident bar and developed the tensional SHPB as shown in Figure 2.4. (Tasneem 2002). In tensional SHPB, gas gun fires the hollow impactor which has the same inner diameter with input bar. As a result of impactor hit to the bolt head, a compressive wave created on the bolt head. This compressive wave turns in to tensile wave as it reflected from the free end of the bolt head. This tensile wave created on the input bar travels and reach the specimen bar interface. At the interface a part of the wave pass to the specimen and the other part reflected back from the interface due to the cross section difference of incident and specimen. The reflected part of the wave turns into compressive wave, transmitted wave continue as tensile wave and pass to the transmitter bar. Strain, stress and strain rate can be calculated with the same formulation that are used in compression SHPB.

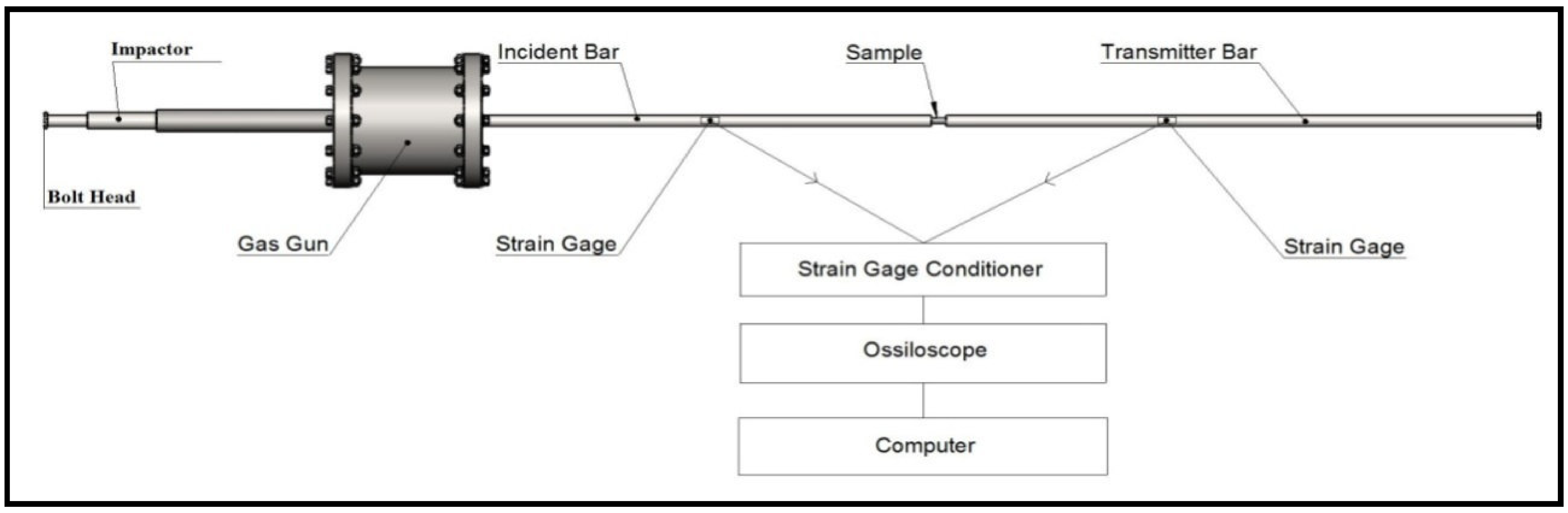

Figure 3.7. Schematic view of SHTB

CHAPTER 4

TITANIUM AND IT IS ALLOYS

4.1. Historical review

Titanium is the fourth most abundant element on the earth's crust. The most important two mineral sources are ilmenite ($FeTiO_3$) and rutile (TiO_2) (Lütjering 2003). The first discovery of the titanium was done in 1791 by Gregor who was an amateur mineralogist in Cornwall (UK); he reported titanium as unknown element in ilmenite ($FeTiO_3$). In 1795, Klaproth found out the same unknown element with Gregor in rutile and named this element as titanium. The name of titanium comes from the Greek mythology. After the discovery of the titanium studies continue with production of high purity titanium.

Production of high purity titanium is difficult due to its tendency to react with oxygen. The first process to produce pure titanium was discovered by Kroll in Luxembourg (1937-1940) (Lütjering 2003). His process involved the reduction of titanium tetrachloride with magnesium in an inert gas atmosphere. This process still preserves its importance and it's still an important production process.

4.2. Crystal Structure and Deformation Modes

Titanium indicates allotropic phase transformation at 882 ^{o}C, its structures changes from body centered cubic crystal structure (β phase) to hexagonal closed packed structure (α phase). The transformation temperature is influenced by the interstitial and substitutional elements. The percentages of alpha and beta phases have important effects on the elastic properties of titanium and its alloys. Alpha phase has an important effect on the elastic property due to its crystal structure. Hexagonal closed packed crystal structure of alpha phase titanium has an anisotropic elastic property, its elastic modulus and shear modulus changes due to the axis of the unit cell and the stress axis. The alpha phase titanium exhibits strain rate sensitivity behavior in dynamic testing. The variation of the elastic and shear modulus decreases as the polycrystalline alpha titanium with crystallographic texture.

The mechanical properties of the beta phase cannot be measured directly because of its unstable phase. Its properties can only be measured from titanium alloys which contain large percentage of beta phase. But in general beta phase has lower elastic modulus than alpha phase (Lütjering 2003). The deformation mechanisms of pure titanium show variation with the phases. High purity alpha phase titanium deforms by twinning in addition to slip by dislocations. The major deformation mode in alpha phase is twinning at low temperatures and the density of the twining depends on the strain rate. Density of the twining increases with the strain rate at low temperatures. In beta phase rich titanium twinning and slip can be observed. But the twining is limited due to its single phase state (Lütjering 2003).

4.3. Basic Properties and Application Areas

Titanium has important application areas due to its excellent properties. Some of its important properties can be listed as;

- High Strength
- Low Density
- Excellent Corrosion Resistance
- Good Creep Resistance
- Good compatibility with human body (for implants)

Due to the requirements for industrial usage some important properties of the titanium can be changed by addition of alloying elements. Adding alloying elements to titanium provides a wide range of physical and mechanical properties. Alloying elements can be classified in to two groups α or β stabilizing addition (Figure 4.1.). The classification depends on the increase or decrease of the α/β stabilizing. Alpha stabilizers are Al, O, N, C, B, Ga and Ge. Aluminum is the most widely used α stabilizer. Beta stabilizers are divided into two; β isomorphous elements; V, Mo, Nb, Ta and Re are β eutectoid forming elements; Cr, Fe, Si, Ni, Cu, Mn, W, Pd and Bi.

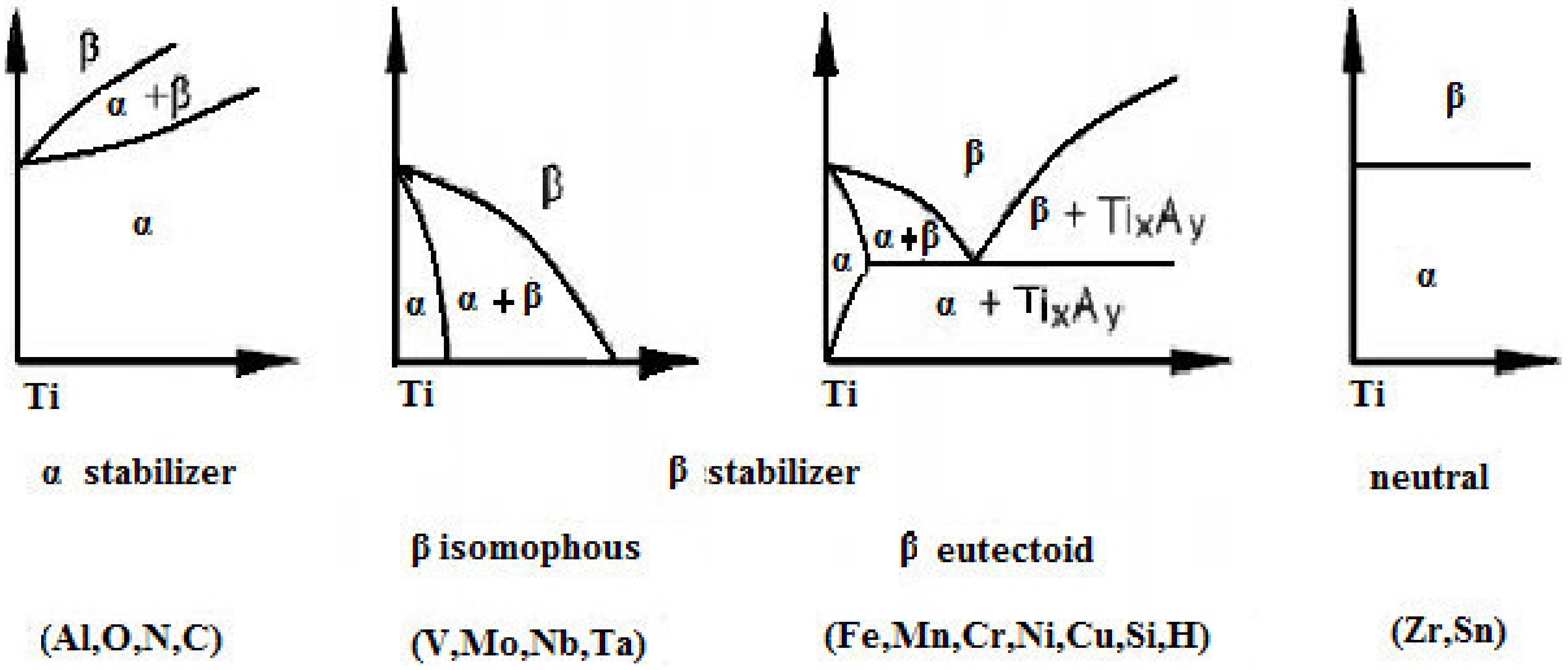

Figure 4.1. Effect of alloying elements on the phase diagrams of titanium alloy (Source: Engineering Materials and Processes)

Alpha titanium alloys are based on the low temperature, hexagonal allotropic form of titanium. The important application of the alpha alloy is the process equipment in chemical and petrochemical industries. The most important properties that make alpha alloy titanium suitable for this usage is high corrosion resistance, formability and weldability. Alpha-beta titanium alloys contain both two phases. This two phase system can be obtained as result of adding controlled amount of beta-stabilizing element, which causes the beta phase to persist below the beta transformation temperature. Cooling down to room temperature results in a two-phase system. The most important and commonly used alpha-beta titanium alloy is Ti6Al4V. Figure 4.2 shows a part of Ti-Al-V phase diagram. At 4 wt % of vanadium the evaluation of the alpha and beta phases can be predicted on the dotted line in Figure 4.2. As the temperature decreases from 1066 ^{o}C, type and percentage of the phases change.

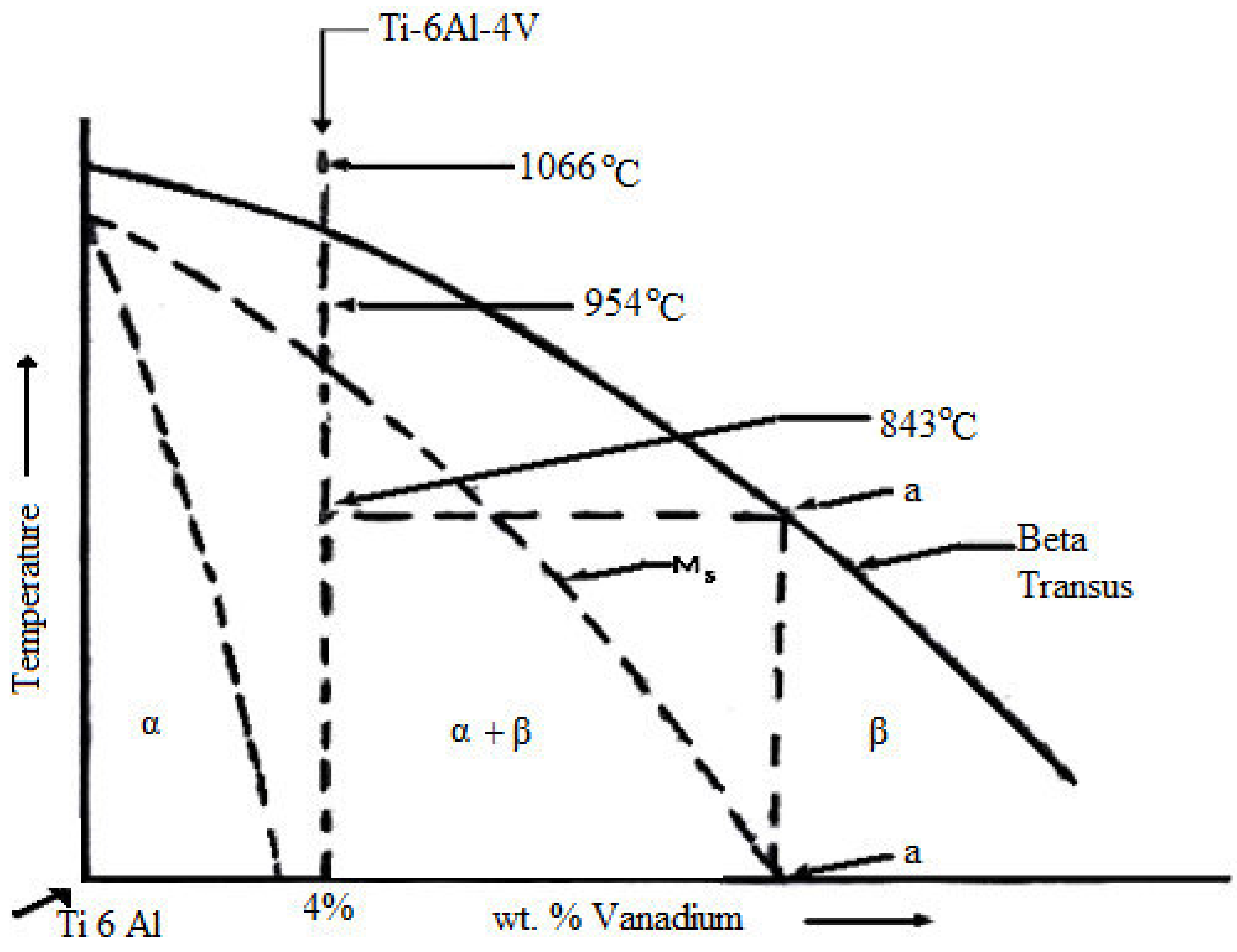

Figure 4.2. Phase diagram of Ti6Al alloy with vanadium addition
(Source: Proc. National Seminar on NonDestructive Evaluation 2006)

The most important application areas of alpha-beta titanium alloy are; aircraft structural parts, rotating and non rotating parts in aero-engines, armor component, biomedical field, sporting equipments and automobiles. Beta titanium alloys can be produce by recrystallization in the beta phase and aging in the alpha and beta phase to precipitate the alpha phase. Beta phase titanium has the highest strength of any titanium alloy. Because of the high strength the usage of beta phase titanium alloys replace with alpha beta alloys in aero space industry.

In the present study, the material and damage model of a biomedical grade Ti6Al4V alloy was determined in order to model its deformation and failure in CWR process. The material contains a low level of interstitial element and therefore, it is anticipated that the mechanical behavior would be different from conventional Ti6Al4V alloy. The lack of damage model for Ti6Al4V in the literature also is also another motivation for the present thesis. Dynamic and quasi-static tests were performed for these purposes. In addition, the microstructure and failure mechanism of Ti6Al4V alloy under quasi-static and high strain rates were examined.

CHAPTER 5

MATERIAL AND TESTING

5.1. Sample Preparation

Tension and compression Ti6Al4V test samples were machined from the biomedical grade Ti6Al4V bars. The bars were supplied from Era Medikal ve Kaynak Ürünleri San. Tic. Ltd. Şti. The bar in 10 mm diameter was used to prepare compression and tension tests specimens, while 19 mm diameter bar was cut into pieces and used for the trial deformations in a CWR machine to determine its formability.

The technical drawing and the picture of a 6 mm diameter compression test sample is shown in Figure 5.1(a) and (b), respectively. The compression test samples, length/diameter ratio of 1, were machined in two different diameters, 6 and 9 mm. These samples were tested in quasi-static and dynamic strain rates. The static and dynamic tension test samples technical drawings and pictures are sequentially shown in Figure 5.2(a-d). The same sample geometries and sizes were used both in quasi-static and dynamic tests, except dynamic test samples had treats at the ends which were used to fix the samples to the tensional SHPB. The gage length of the samples was 10 mm and the diameter 4 mm. Both, compression and tension test specimen sizes are non-standard, which is dictated by the specimen size limitation in SHPB testing. The stress equilibrium is lost when long and small diameter samples are used in SHPB.

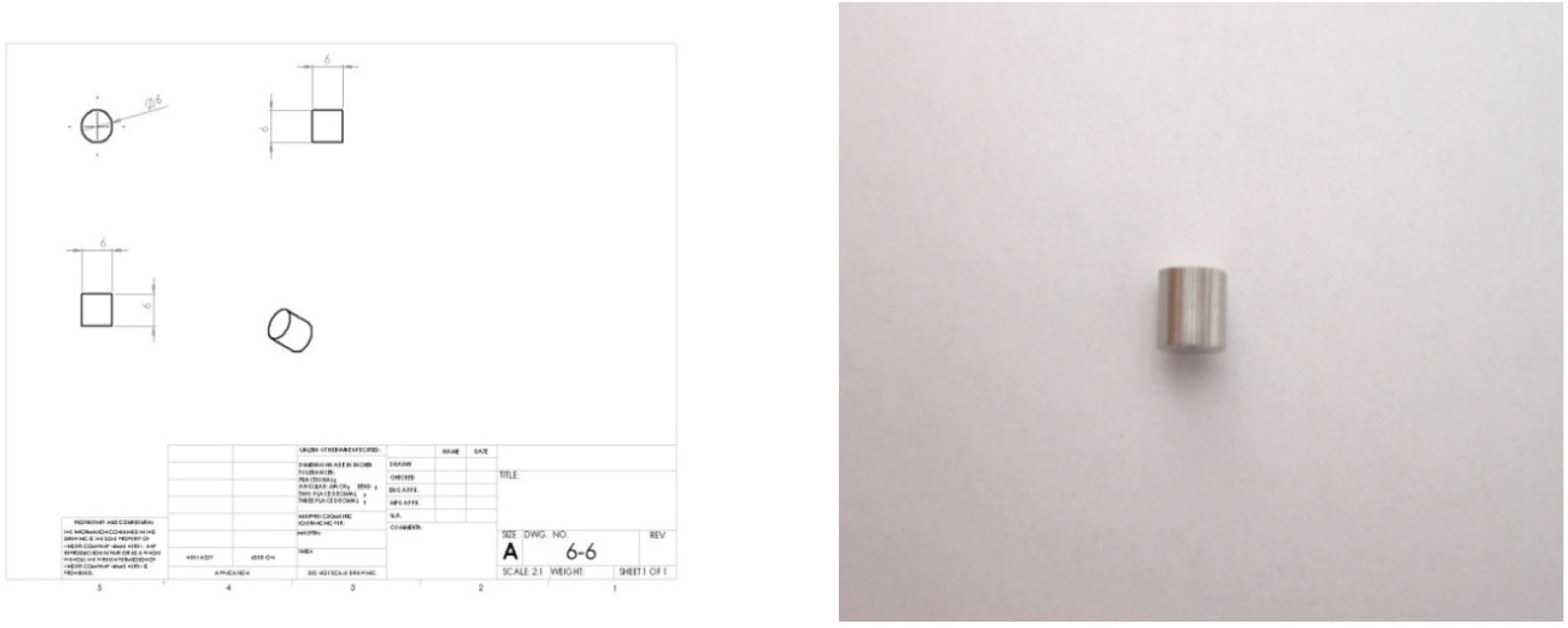

(a)

(b)

Figure 5.1. Compression test specimen (a) technical drawing and (b) picture

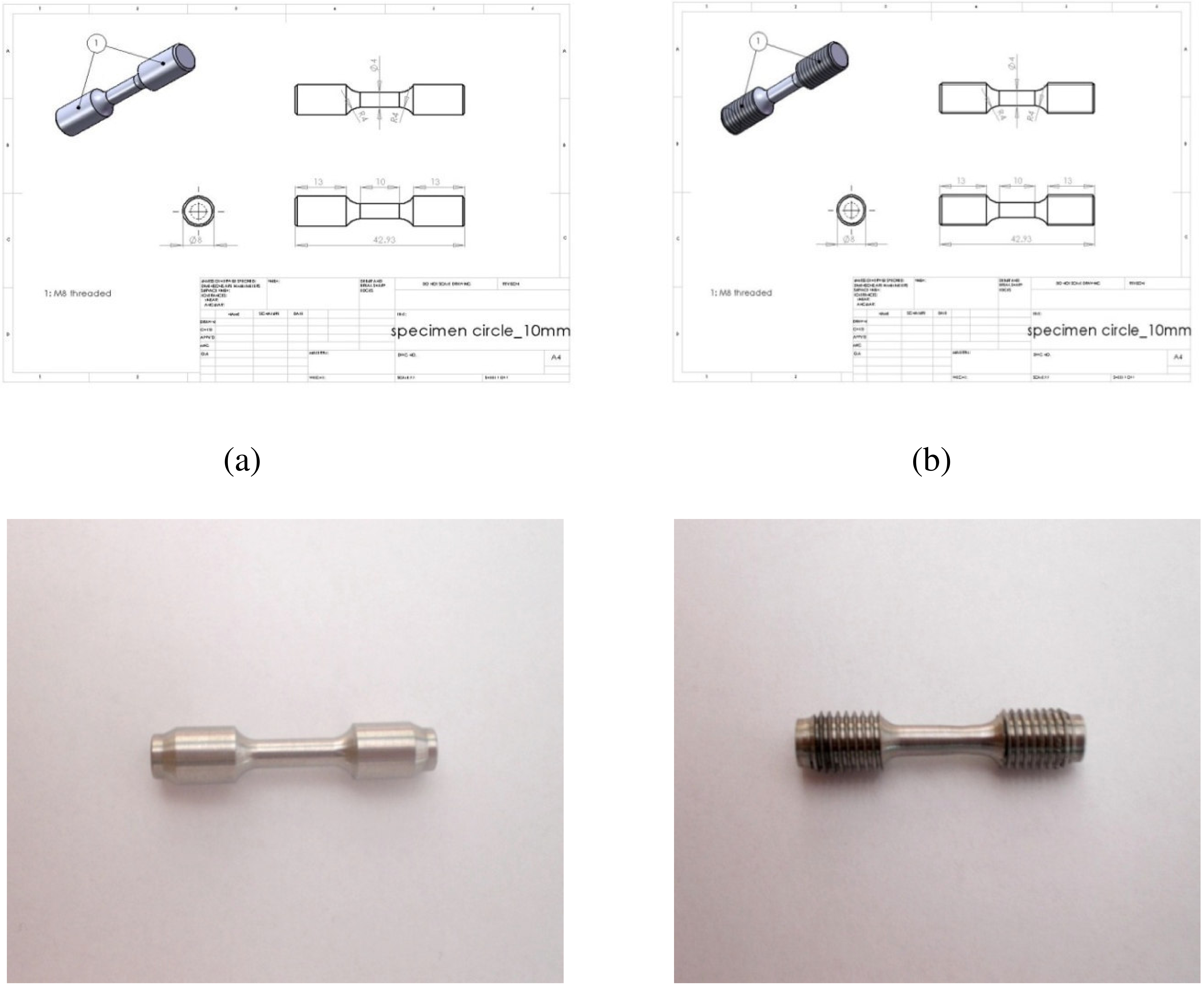

(a)

(b)

(c)

(d)

Figure 5.2. Tension test specimens (a)-(b) technical drawings and (c)-(b) pictures

5.2. Testing

Quasi-static compression and tension tests were performed using a Shimadzu Autograph AG-X 300 test machine within a strain rate regime ranging between 10^{-3} and 10^{-1} s^{-1}. In compression tests, the samples end surfaces were lubricated with grease before each test. The compression test specimen size and the strain rates are further tabulated in Table 5.1. In order reduce the extent of specimen heating effect at increasing strain rates larger specimens (9 mm in diameter) were tested. At the lowest strain rate, 6 mm and 9 mm samples were initially tested in order to check if the specimen size had an effect on the measured stress values. These test showed that the difference between the stress values of 6 mm and 9 mm diameter sample was insignificant.

Table 5.1. Quasi-static compression test samples and the compression strain rates

No	Specimen Dimensions	Strain Rate(s^{-1})
1	Diameter:6mm Height:6mm	0.001
2	Diameter:6mm Height:6mm	0.01
3	Diameter:6mm Height:6mm	0.1
4	Diameter:9mm Height:9mm	0.001
5	Diameter:9mm Height:9mm	0.01
6	Diameter:9mm Height:9mm	0.1

For each strain rate, the tests were repeated five times. Engineering stress-strain curves were then converted into true stress-strain curves as depicted in Figure 5.4. Finally the plastic strain and plastic strain rate were calculated using following relations;

$$\varepsilon_p = \varepsilon_t - \frac{\sigma}{E} \tag{5.1}$$

and

$$\dot{\varepsilon}_p = \frac{d\varepsilon_p}{dt} \tag{5.2}$$

where, ε_t is the total strain. As in the compression tests, tension tests were repeated five times for each strain rate. Similar to compression tests, engineering stress-strain curves were converted into true stress-strain curves using the same relations (Figure 5.4.).

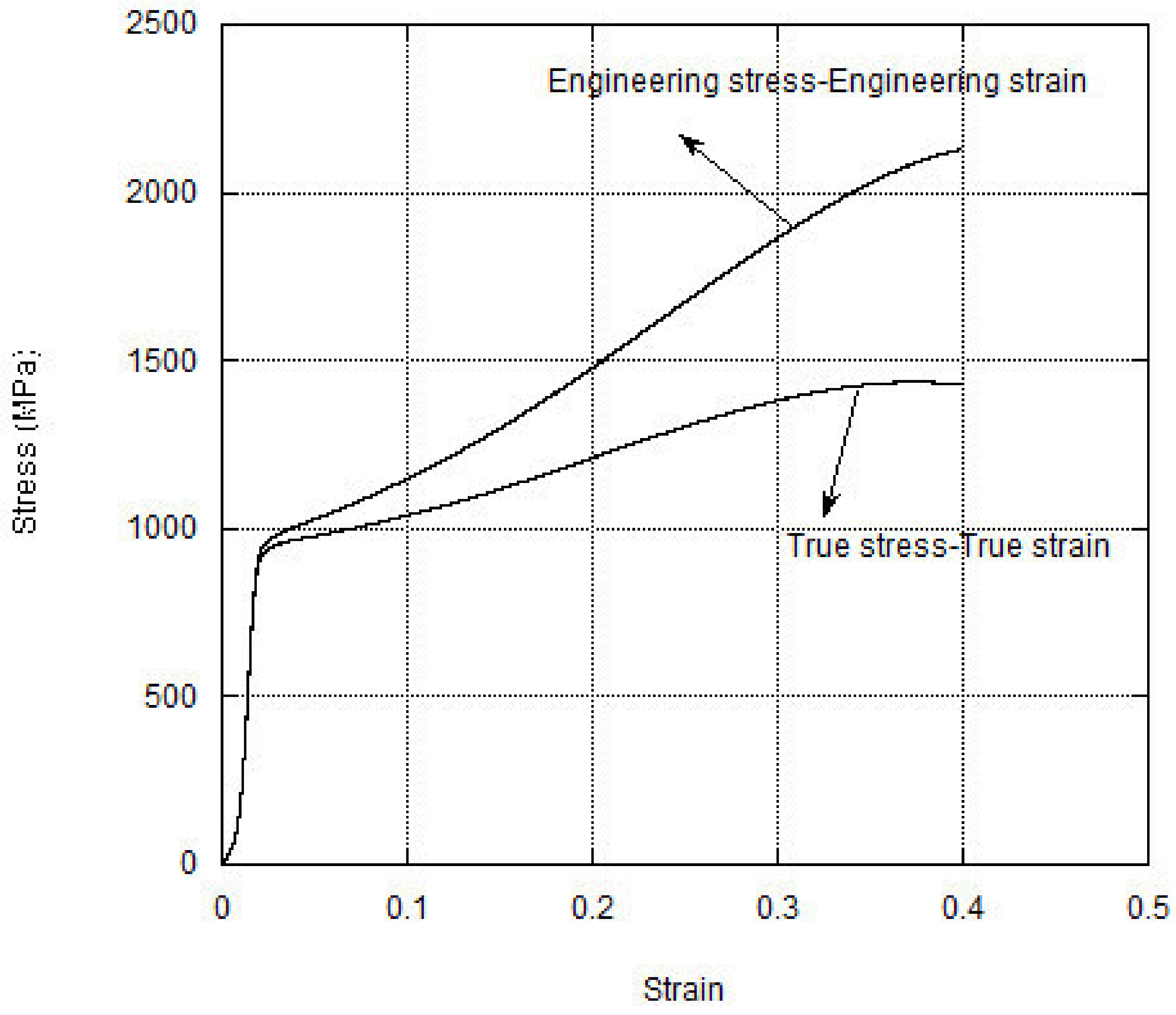

Figure 5.3. Engineering and true stress-strain curve of a compression test

As in the compression tests, tension tests were repeated five times for each strain rate to provide accurate results. Similar to compression tests, engineering stress-strain curves were converted into true stress-strain curves using the same relations (Figure 5.4.).

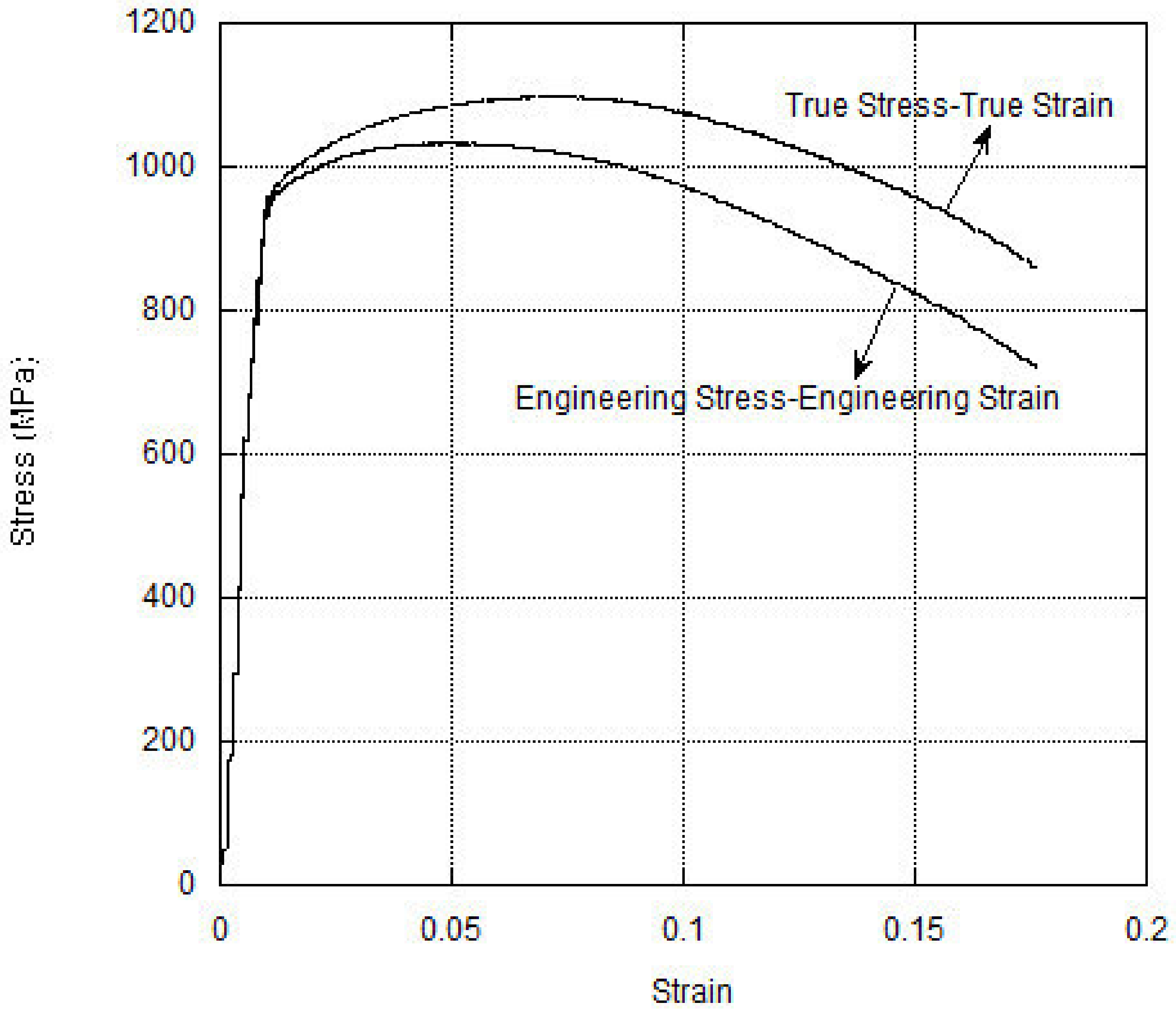

Figure 5.4. Example of a true and engineering stress-strain graph obtained from tension test

Dynamic compression and tension tests were performed using compression and tensional SHPB testing apparatus, respectively. The used SHPB test apparatus consists of three major parts; gas gun assembly (Figure 5.5(a)), bars (Figure 5.5(b)) and electronic measurement devices (Figure 5.5(c)). The gas gun assembly consists of pressure chambers which facilitate the impact of striker bar on to the incident bar. For that purpose, the inner and outer pressure chambers of the gas gun assembly are pressurized with nitrogen from a high pressure gas cylinder before each test. When the inner gas chamber pressure is released with a valve, the outer chamber pressure is emptied into the barrel. This moves the striker bar horizontally until it impacts the incident bar end. This impact initiates a constant amplitude compressive elastic wave in the incident bar. In each test, $v_{o,}$ can be measured just before impact of the striker bar on to the incident bar by the help of two infrared beams (speed measurement sensors) as seen in (Figure 5.5(a)). The used compression type SHPB bars are made from CPM Rex76 alloy. The mechanical properties of the bar alloy are tabulated in Table 5.2. The lengths of the available striker bars are 362 and 724 mm and the lengths of the incident and transmitter bars are 3658 and 1440 mm. All bars diameters are the same, 20 mm. The electronic measuring system consists of strain gage conditioner and oscilloscope. The strain gage conditioner is used to form a full bridge strain gage circuit on the bars in order to measure the longitudinal strain involved in each test. An oscilloscope connected to the strain gage conditioner is used to monitor and record the strain gage bridge circuit voltages during each experiment. Besides these devices, a micro-computer is used to conduct data reduction (calculation of stress and strain). In SHPB testing, specimen surfaces in intimate contact with the bar ends are lubricated in order to reduce frictional effects because the presence of any constraining effect on the specimen surfaces forms a multiaxial stress-state which invalidates one of the most important assumption of the SHPB analysis, namely, that of a uniaxial stress state. The samples surfaces were lubricated using grease.

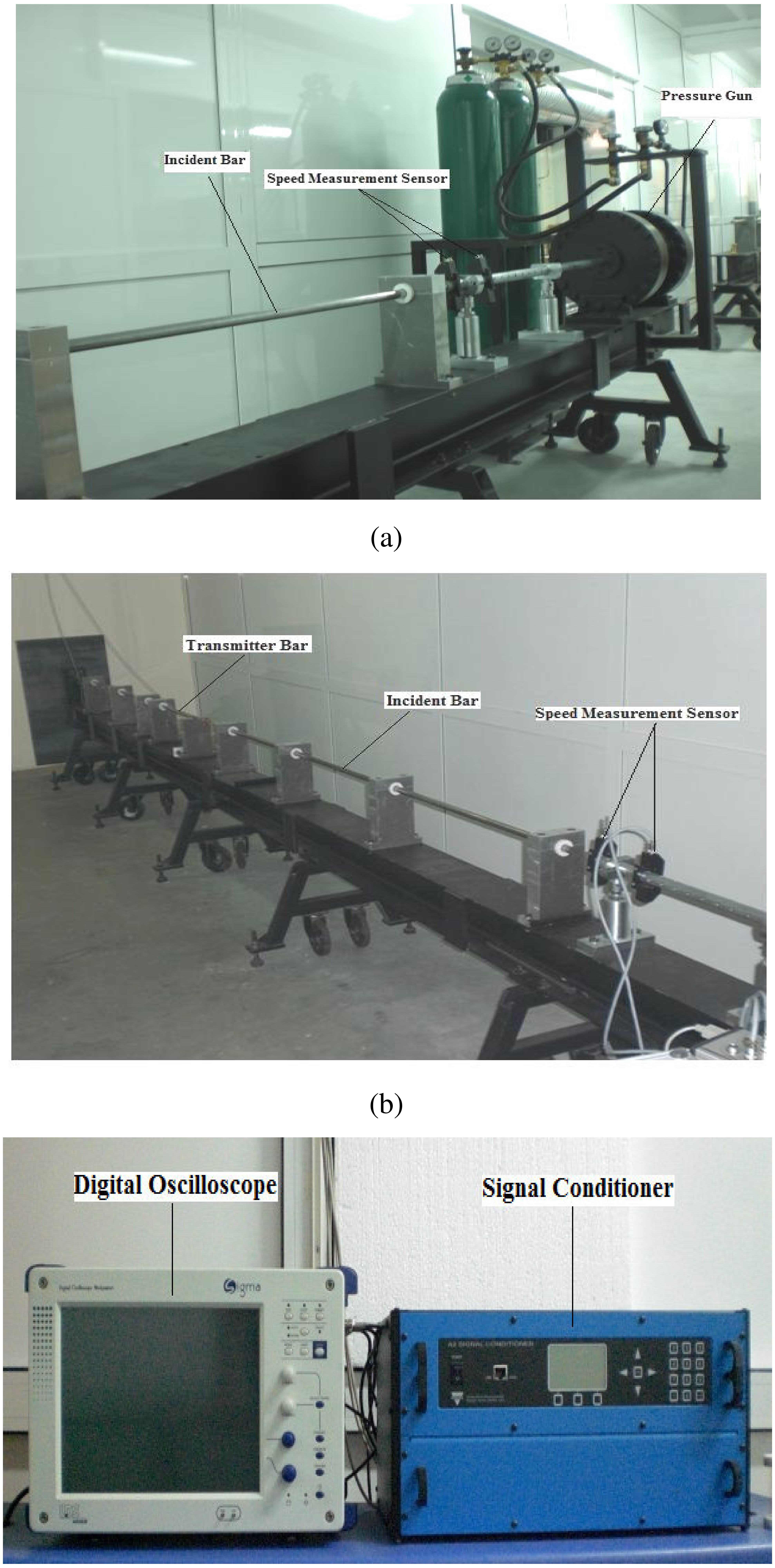

(a)

(b)

(c)

Figure 5.5. Compression SHPB (a) gas gun, (b) bars and (c) strain measurement devices

Table 5.2. Compression bars properties

Material	Elastic Module	Density	Hardness
CPM Rex76	214 GPa	8255 kg/m^3	40 HRC

The strain in the specimen was calculated using the following relation developed for full bridge,

$$\varepsilon_s = -\frac{2C_b}{L_s}\left(\frac{2\int \varepsilon_r(V)dt}{G_g K_g V_e(1+\varphi)}\right) \tag{5.3}$$

where, G_g, K_g, V_e and φ are the strain gage conditioner gain, strain gage factor, excitation voltage of the strain gage bridge and Poisson's ratio of the bar material, respectively. The stress in the specimen was calculated using

$$\sigma_s = \frac{A_b}{A_s}E_b\left(\frac{2\varepsilon_t(V)}{G_g K_g V_e(1+\varphi)}\right) \tag{5.4}$$

The values of G_g, K_g, and V_e were 20, 2.08 and 10 V, respectively.

Typical SHPB compression strain readings of a tested Ti6Al4V sample are shown in Figure 5.6. Typical engineering stress-strain and strain rate-strain curves of the same sample are shown in Figure 5.7.

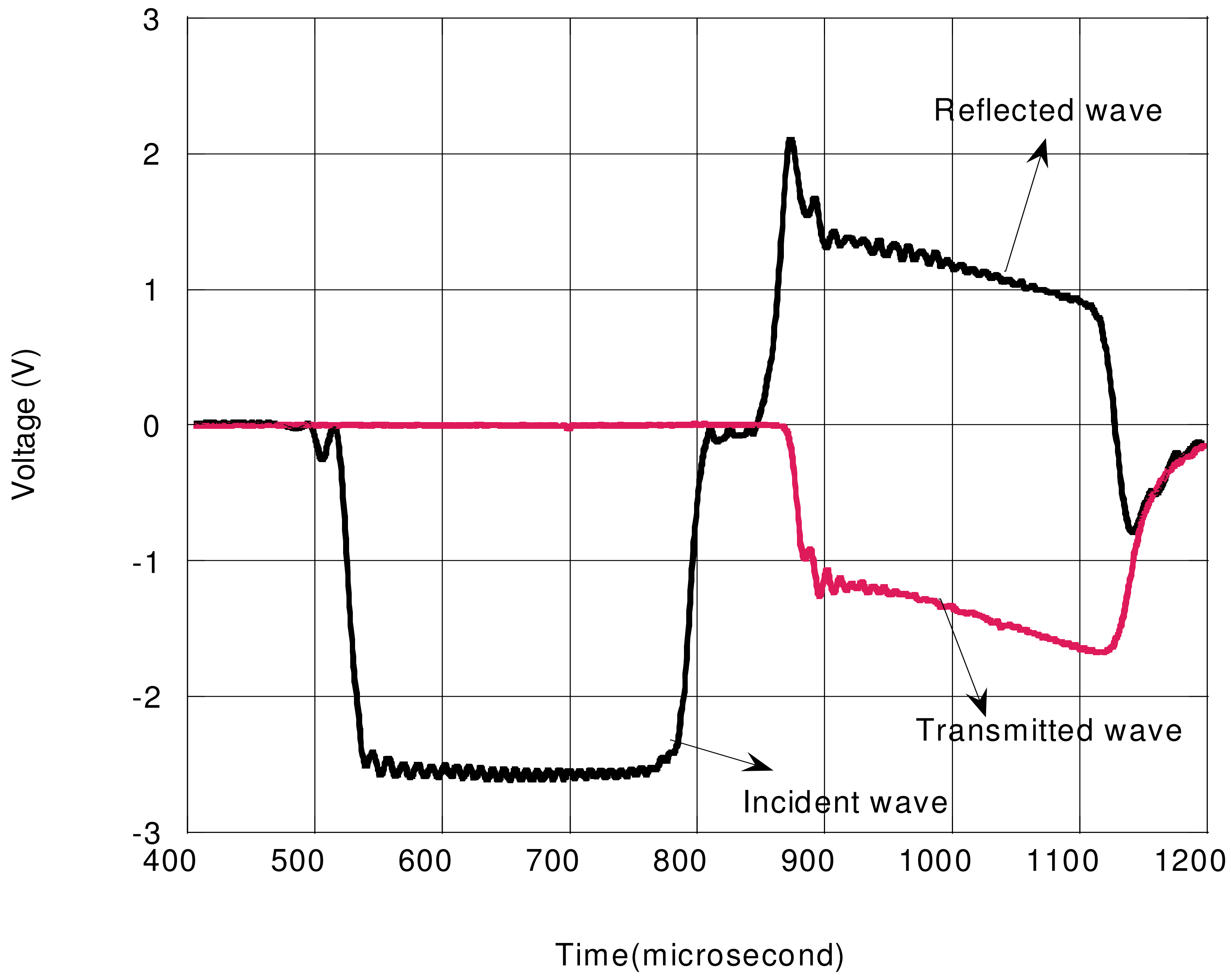

Figure 5.6. Typical compression test voltage vs. time graph

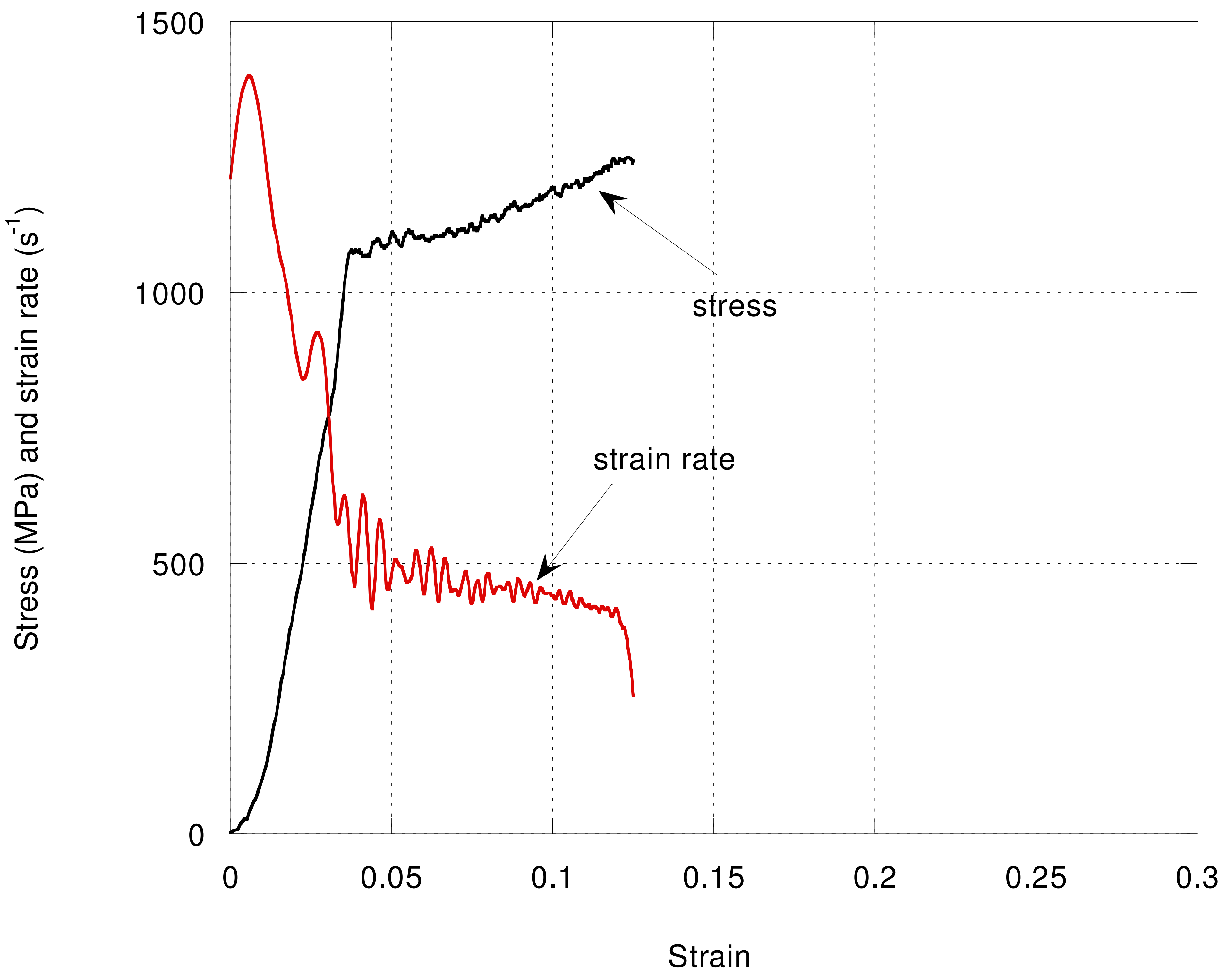

Figure 5.7. Typical compression, engineering stress-strain and strain rate-strain curves of Ti6Al4V

The used tension SHPB apparatus pictures are shown in Figure 5.8.(a) and (b). Similar to compression SHPB, tensional SHPB consists of three parts: gas gun assembly, bars and electronic measurement devices. The bars of tension SHPB are made of 316 L stainless steel. The properties of the bar material is tabulated in Table 5.3. Typical tensional SHPB strain readings of a tested Ti6Al4V sample are shown in Figure 5.9. Engineering and true stress-strain curves were calculated using the same relations used in compression test.

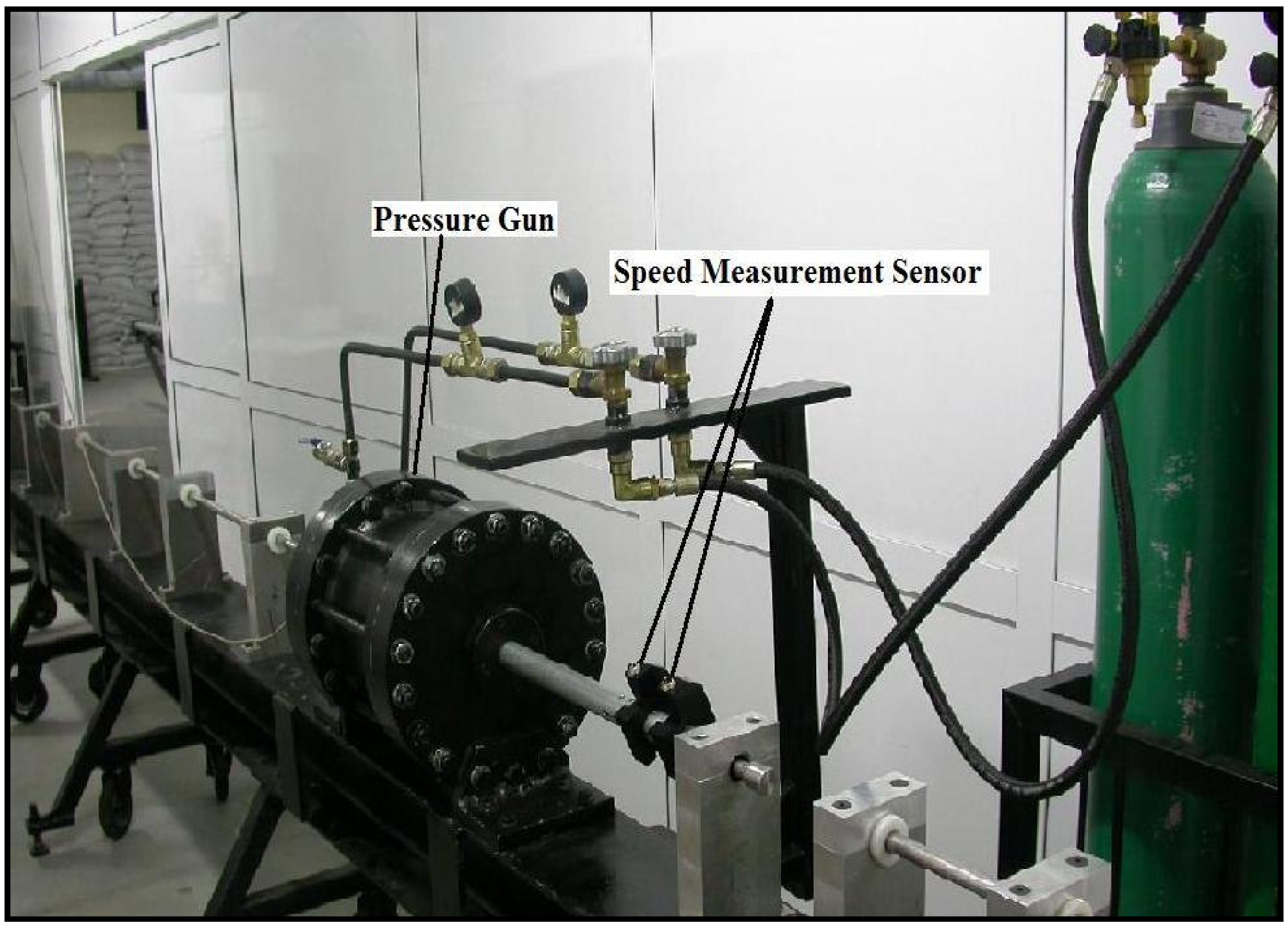

(a)

(b)

Figure 5.8. Tension SHPB apparatus; (a) gas gun assembly and (b) bars

Table 5.3. Properties of the tension bars

Material	Elastic Modulus	Density
316 L	193GPa	8gg/cc

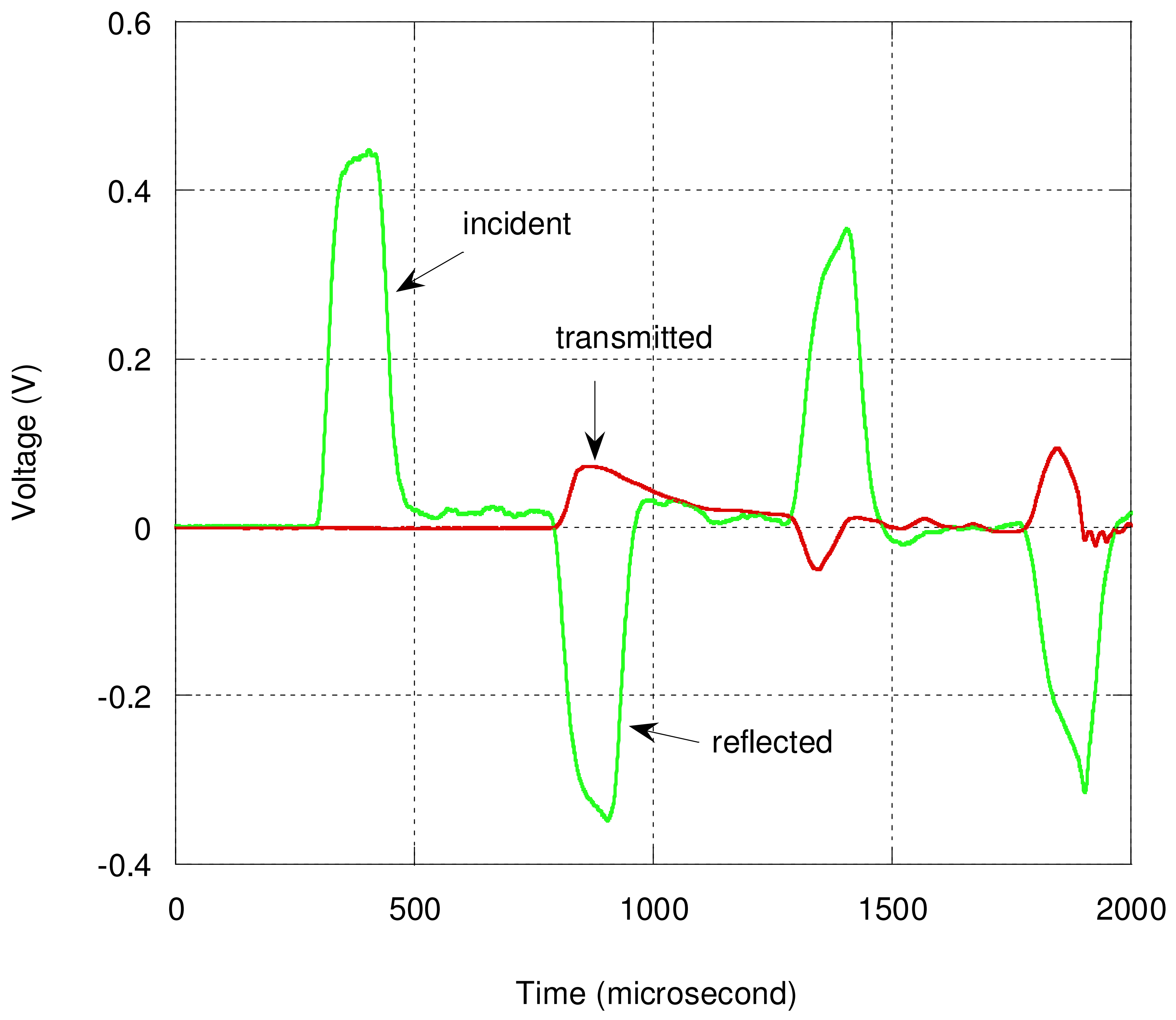

Figure 5.9. Typical voltage vs. time graph of SHPB tension test

Elevated temperature tests (300 ^{o}C) in compression SHPB were conducted using a small split-tube furnace covering the specimen and only a small portion of the bars. The length of the bars remaining in the furnace was 20 cm. The furnace was insulated in order to heat only the specimen and the bars sections remaining in the furnace. The furnace, together with the bars and sample, was heated to the desired temperature. Temperature measurement was conducted using a thermocouple. The thermocouple was suspended from the top of the split furnace until it just touched the specimen. The heating was achieved in 10 minutes and then the test was conducted.

Notch specimens were further tested to determine JC damage parameters. Specimen with notch radius 2, 3 and 6 mm were prepared and tested (Figure 5.10.). The geometrical parameters and stress triaxiallity of the tested specimens are listed in Table 5.4. Unnotched specimens had stress triaxiality of 0.33 and as the radius of curvature decreases the stress triaxility increases.

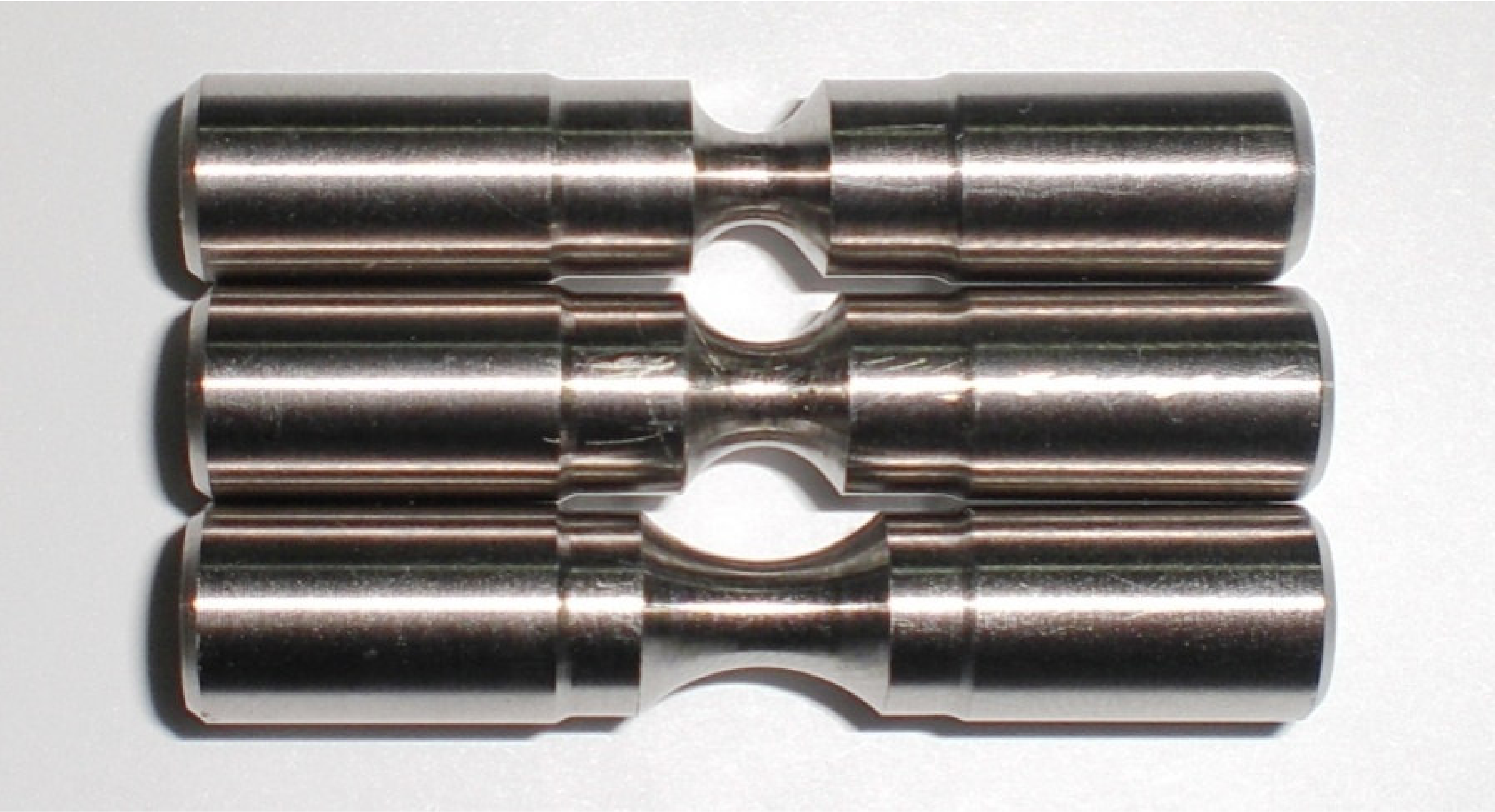

Figure 5.10. Picture of the notched specimen with different radius

Table 5.4. The geometrical parameters of unotched and notched tension specimens

Material	Unotched			
Radius of curvature (R) (mm)	-	6	3	2
Minimum radius (mm)	6	4	4	4
Stress triaxility	0.33	0.486	0.621	0.738

Notched specimens were tested quasi-statically within the strain rate regime of $1x10^{-3}$- $1x10^{-1}$ s^{-1} using static test machine. While the load-displacement data were recorded, the sample deformation was recorded using a high speed camera. The camera zoomed to the specimen gage length and the test was recorded with 50 fps (frame per second) and 320x832 pixel format. The variation of the specimen minimum diameter and radius of curvature were measured using the video camera records. For each sample tested the effective fracture strain was measured. Figure 5.11(a) shows a typical stress-strain curve of a notched specimen and Figure 5.11(b) the corresponding video record pictures at various strain levels. Although the starting values of stress triaxility, R and a changed during a test near the fracture, this change was not taken into account. For example stress triaxility in a typical experiment changed only 15% near the fracture.

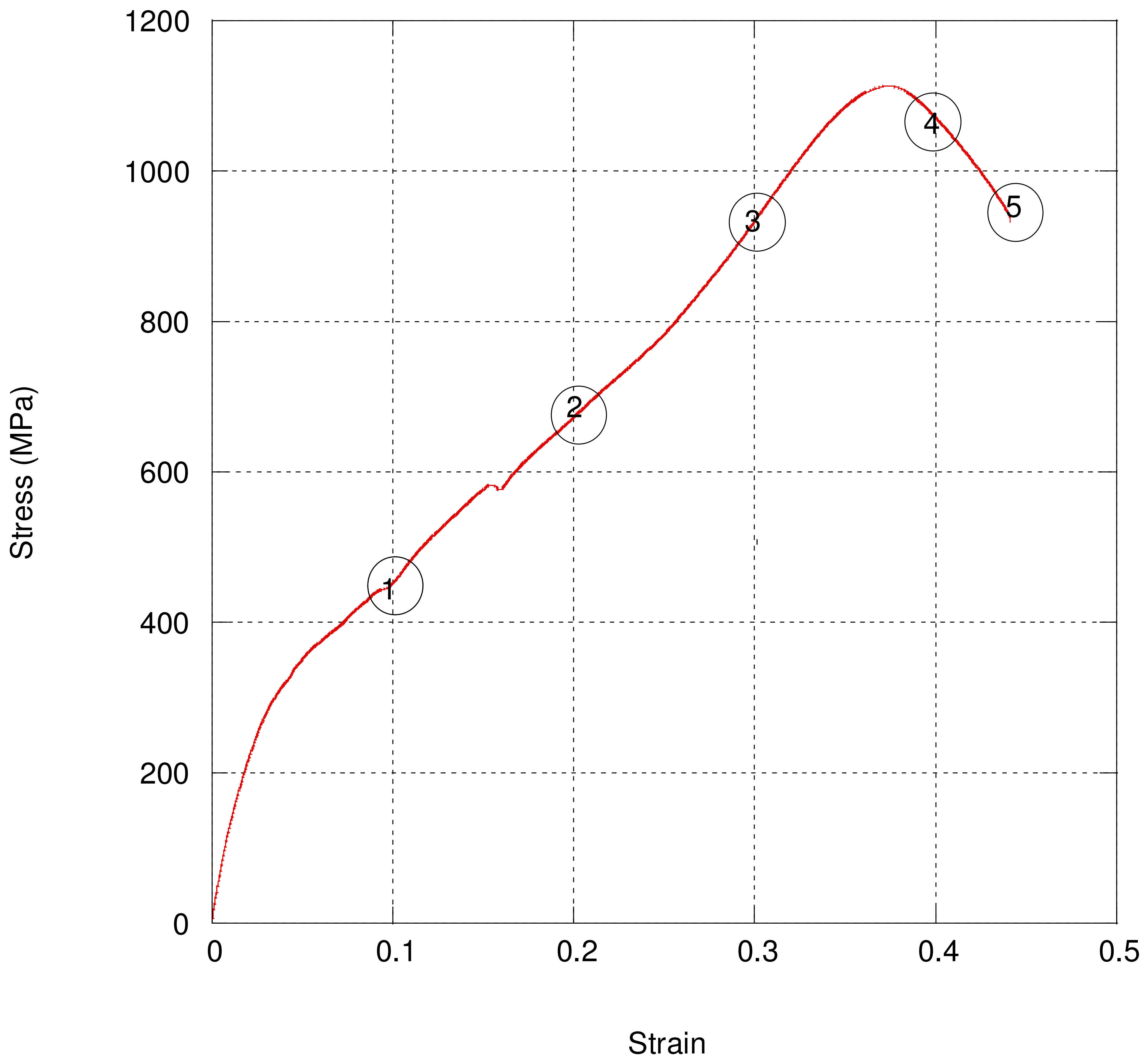

(a)

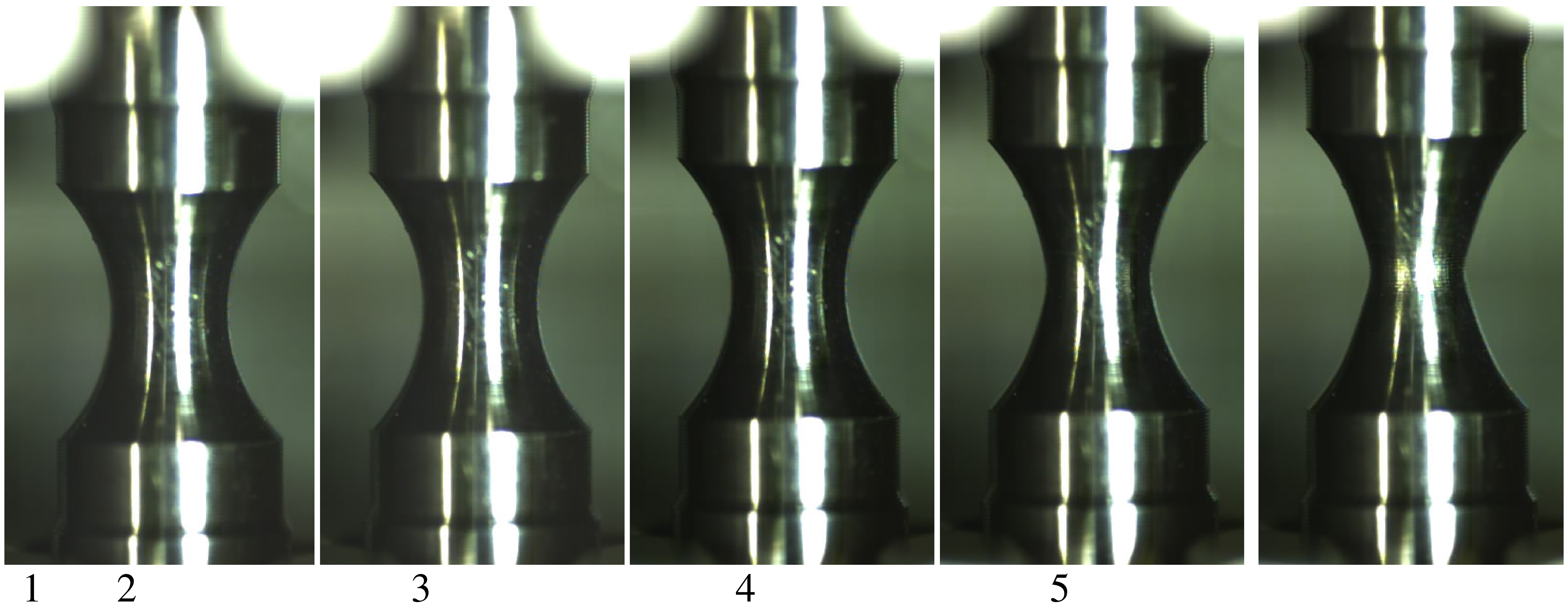

(b)

Figure 5.11. (a) Typical stress-strain curve of notched specimen (R=6 mm) and (b) the pictures of the notched section at various strains.

5.3. Microscopy

Microscopic analysis of untested and tested specimens was performed using an optical microscope and a Philips XL30-SFEG scanning electron microscope (SEM) with an Energy Dispersive X-ray (EDX) analyzer. Deformed samples were cut using a slow speed diamond saw and then epoxy mounted. The mounted samples were then grinded and polished down to 1 micron. The polished cross-sections of samples were etched with Kroll's reagent (3 cm^3 of HF and 6 cm^3 of HNO_3 in 100 ml of H_2O).

CHAPTER 6

RESULTS AND DISCUSSION

6.1. Quasi-Static Tests and Dynamic Tests

Representative compression true stress-true strain curves of 6 mm diameter specimen at quasi-static strain rates of 1x10^{-3}, 1x10^{-2} and 1x10^{-1} s^{-1} are shown in Figures 6.1(a-c), respectively. In each graph shown in this figure, includes at least three true stress-true strain curves. As noted in Figure 6.1(a-c), there is an insignificant variation between each test at a specific strain rate. It is further noted that as the strain rate increases from 1x10^{-3} to 1x10^{-1} s^{-1} the yield strength increases, showing the strain rate sensitive flow stress behavior of the tested Ti alloy. The yield stress of the 6 mm diameter specimen at 1x10^{-3} s^{-1} is about 927 MPa and it increases to 1000 MPa when the strain rate increases to 1x10^{-1} s^{-1}. In Figure 6.2, the true stress-true strain curves of 6 and 9 mm diameter samples tested at 1x10^{-3} s^{-1} are shown together for comparison. Both specimens show essentially similar stress values until about 0.1 strain, while 9 mm diameter samples show higher stress after this true strain. This signifies the dominance of the frictional forces at increasing strain levels in larger diameter samples. Although 6 mm specimens fail at about 0.4 strain, 9 mm diameter samples fail about 0.3 strain was about %30.

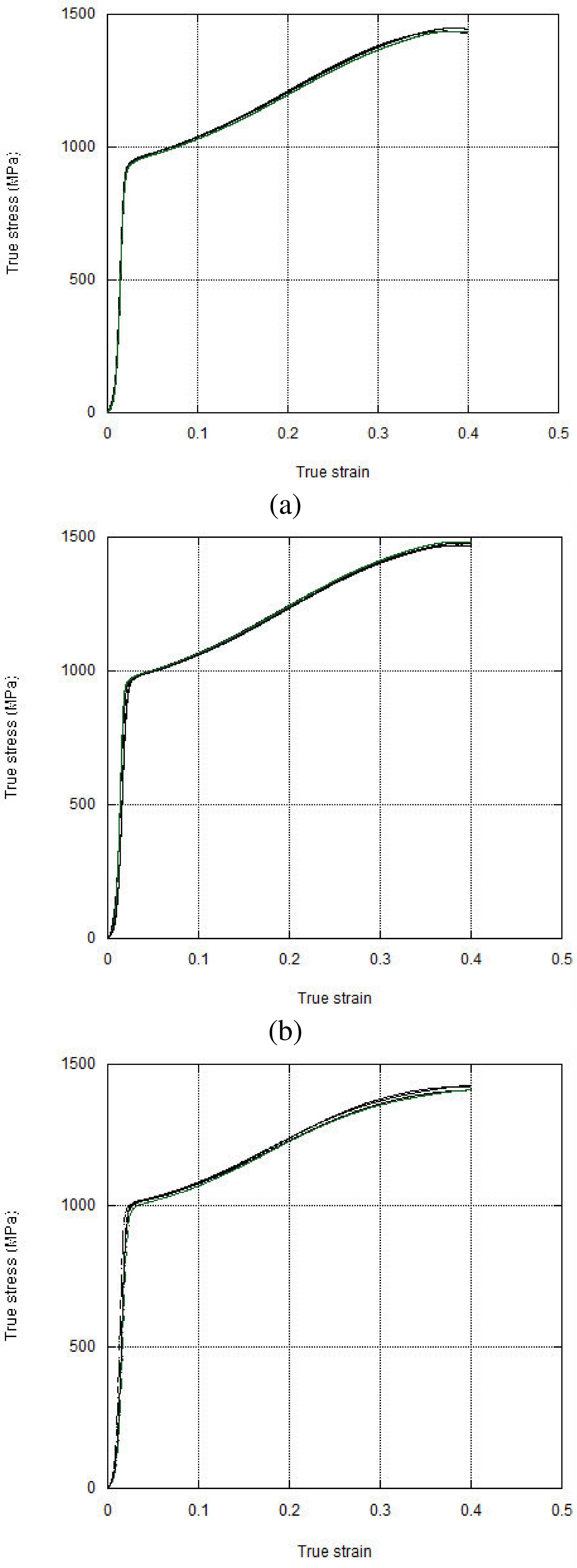

(a)

(b)

(c)

Figure 6.1. Compression true stress-true strain graph of 6 mm diameter Ti6Al4V alloy at (a) 1x10^{-3} s^{-1}, (b) 1x10^{-2} s^{-1} and (c) 1x10^{-1} s^{-1}

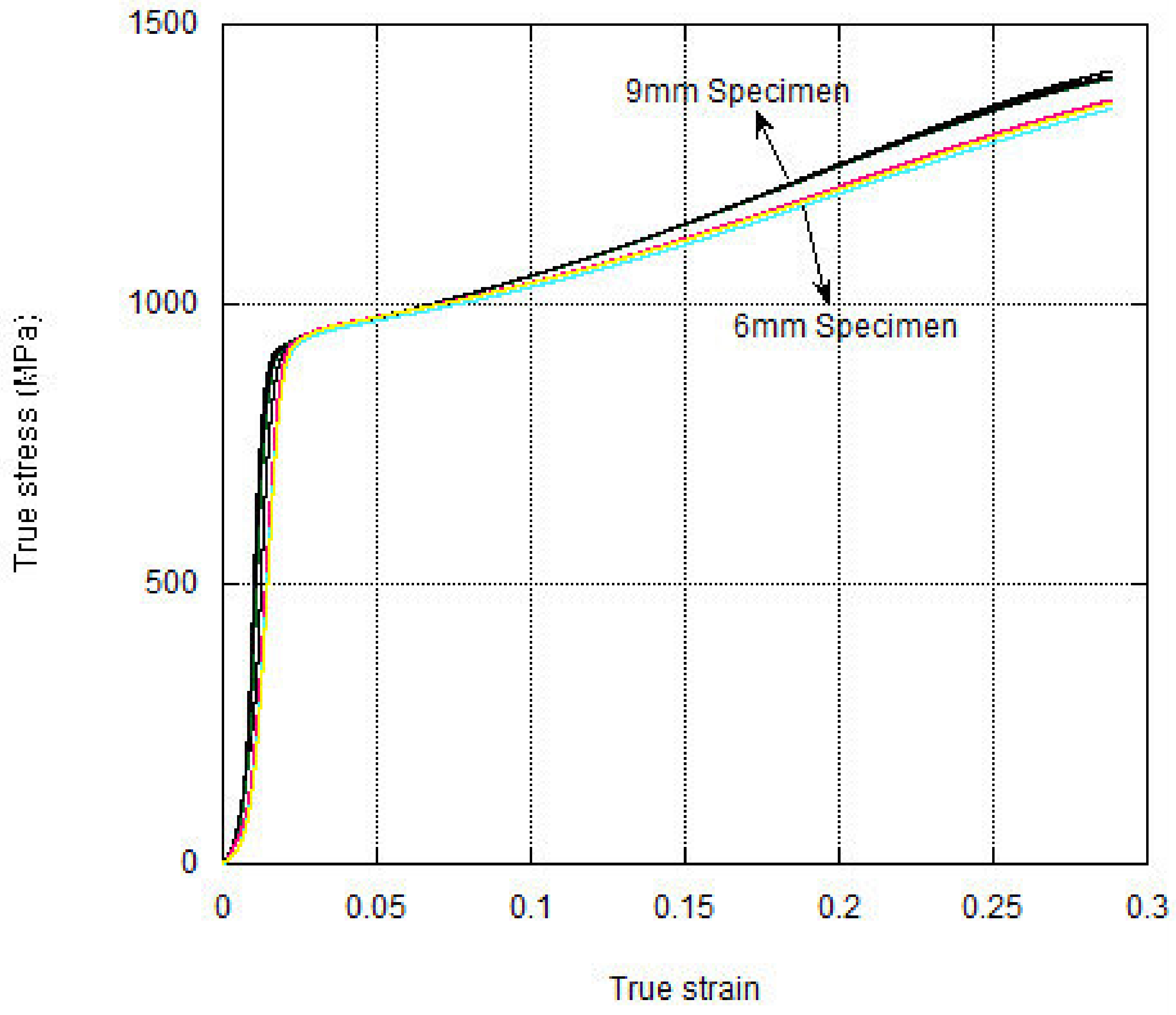

Figure 6.2. True Stress- true strain curves of 6 and 9 mm Ti6Al4V samples at $1x10^{-3}$ s^{-1}

The tension true stress- true strain curves of 4mm diameter Ti6Al4V alloy specimens at quasi-static strain rates of $1x10^{-3}$, $1x10^{-2}$ and $1x10^{-1}$ s^{-1} are shown in Figure 6.3(a-c). Again each graph shows at least three tension test curves. The stress values increases above the yield stress until the necking starts and with the necking the stress values decreases and the sample fails with a ductile fracture mode. Yield strength at $1x10^{-3}$ s^{-1} is about 930 MPa which is consistent with compression yield strength (927 MPa). Similar to compression tests, yield stress increases with increasing strain rate in tension. The measured percentage of elongations are about 18%, which is consistent with the elongation (%15) provided by the manufacture. The effect of quasi-static strain rate on the stress-strain curves is shown in Figure 6.4. As the strain rate increases the yield and flow stress increases (Figure 6.4.) while the failure strain decreases.

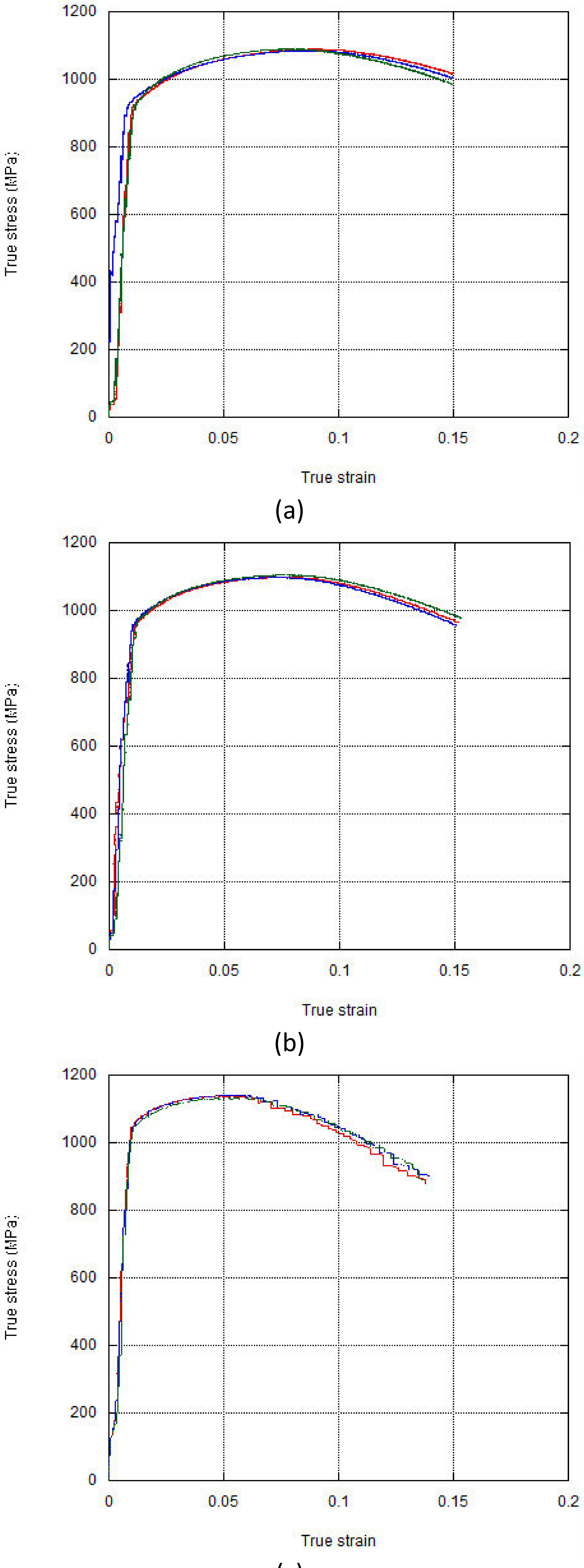

(a)

(b)

(c)

Figure 6.3. Tension true stress-true strain graph of 4mm diameter Ti6Al4V alloy at (a) $1x10^{-3}$ s^{-1}, (b) $1x10^{-2}$ s^{-1} and (c) $1x10^{-1}$ s^{-1}

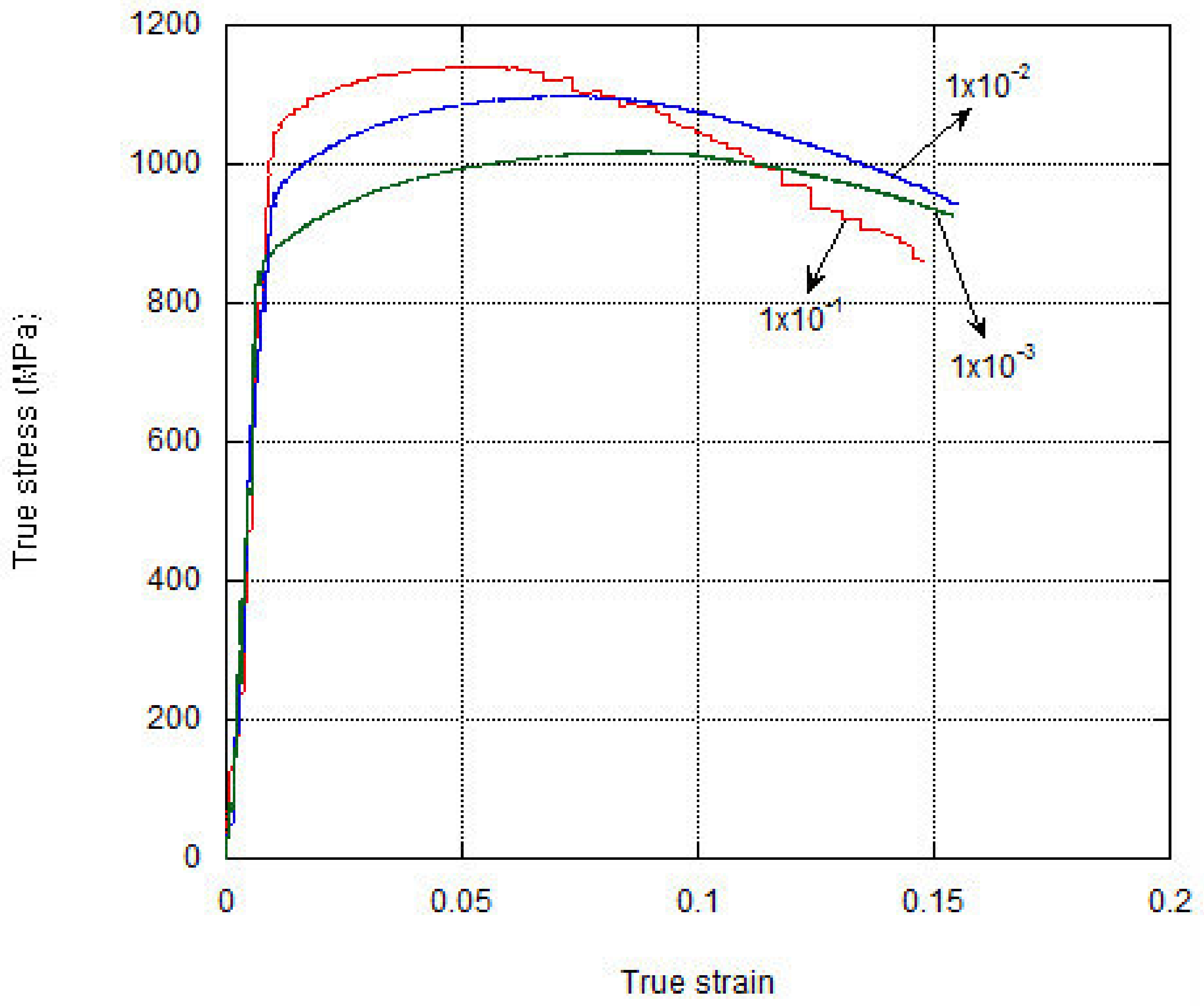

Figure 6.4. Tension true stress-true strain curve at quasi-static strain rates

The high strain rate compression tests were conducted in the strain rate range between 495 and 950 s^{-1}. Typical high strain rate compression tests performed at 495 s^{-1} and 550 s^{-1} are shown in Figure 6.5 and Figure 6.6, respectively. The similar stress-strain behavior obtained for each group of tests proves the consistency of the high strain rate tests. Figures 6.7 and 6.8 show the compression and tension plastic stress-strain curves of samples tested at quasi-static and high strain rates, respectively. These graphs clearly show that Ti6Al4V alloy has strain rate sensitive flow stress behavior. The decrease in stress values of the compression tests at increasing strain rates (Figure 6.7.) is due to the thermal softening effect of the adiabatic heating. At increasing strain rates the heat generated in the specimen is accumulated in the sample due short duration time of the deformation. The effect of adiabatic heating is neglected in this study since the flow stresses used to construct the constitutive equations are determined at relatively low strain levels at which the effect of adiabatic heating is not significant. In tension tests similar to compression tests, as the strain rate increases the yield and flow stress increases (Figure 6.8.), while the failure strain decreases.

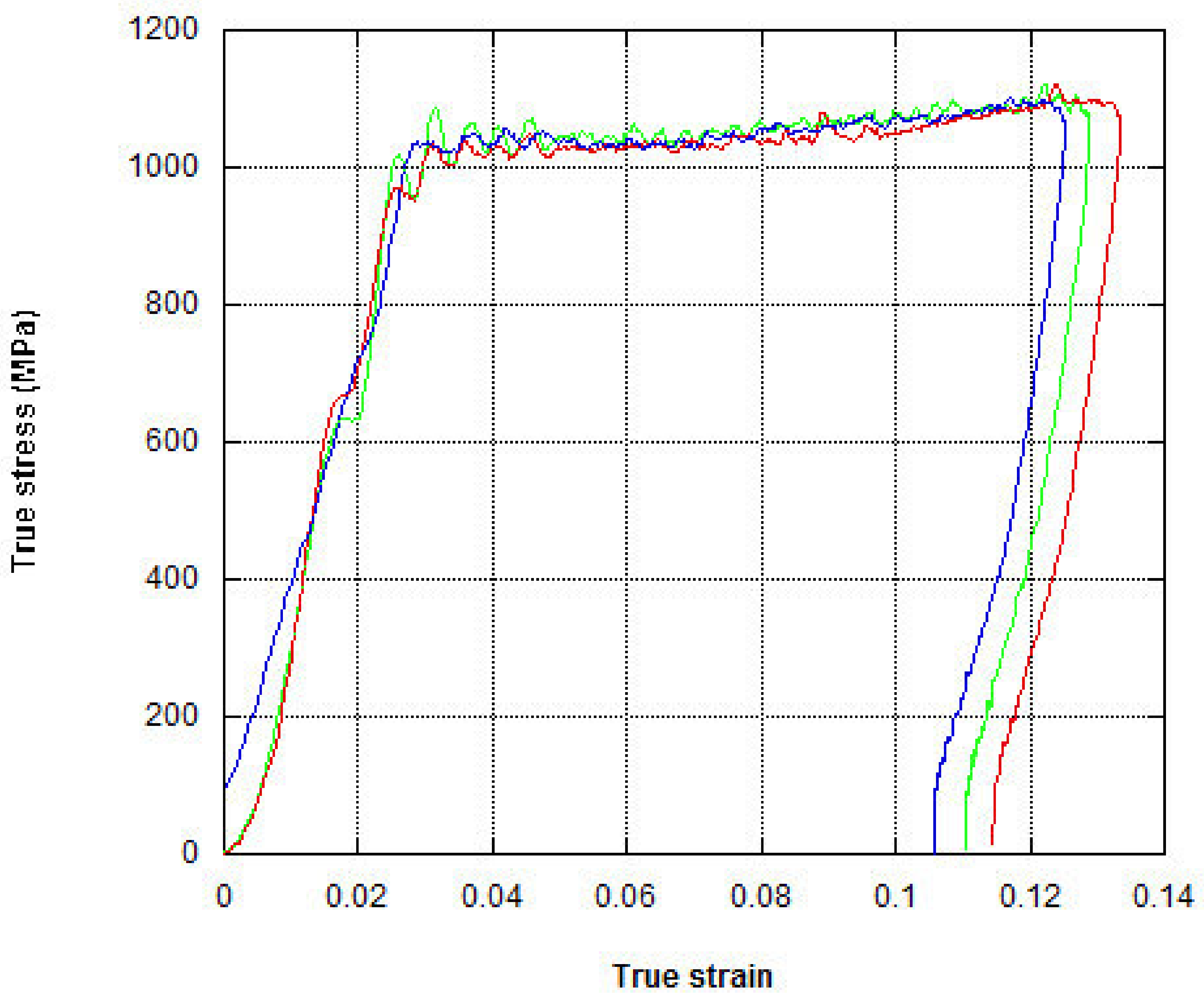

Figure 6.5. Typical high strain rate tests performed under compression at 495 s^{-1}

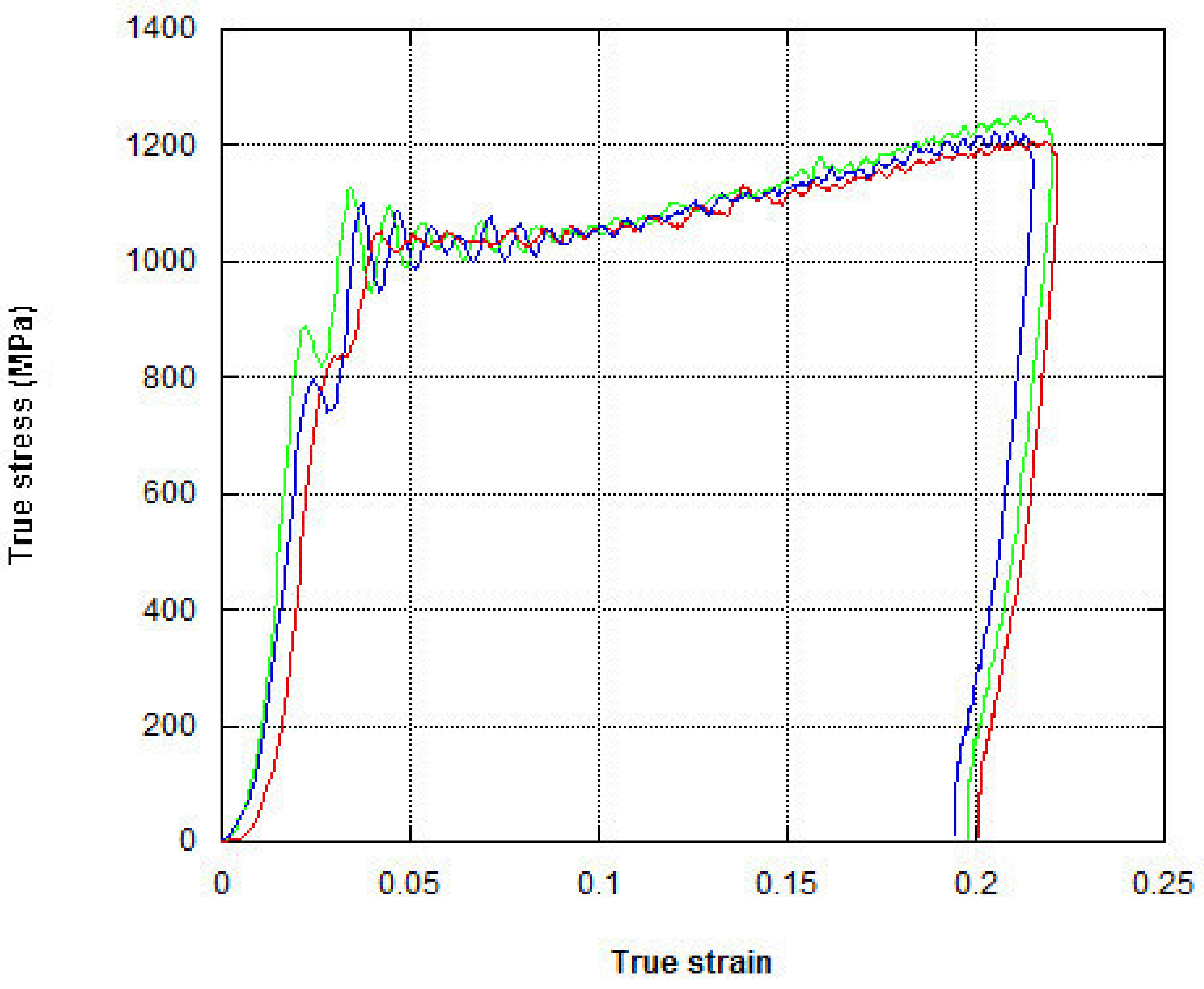

Figure 6.6. Typical high strain rate tests performed under compression at 550 s^{-1}

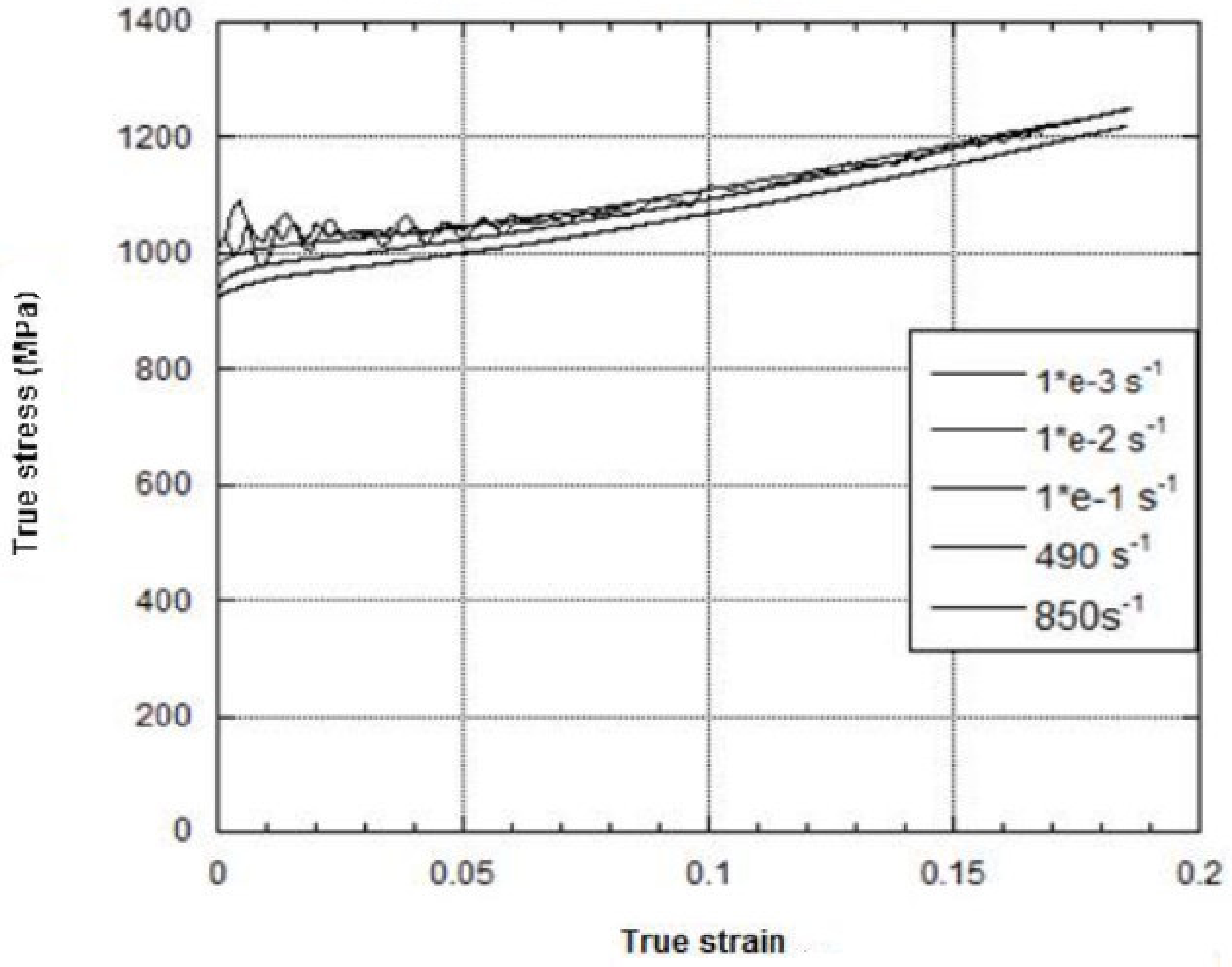

Figure 6.7. Compression plastic true stress-strain curves at different strain rates

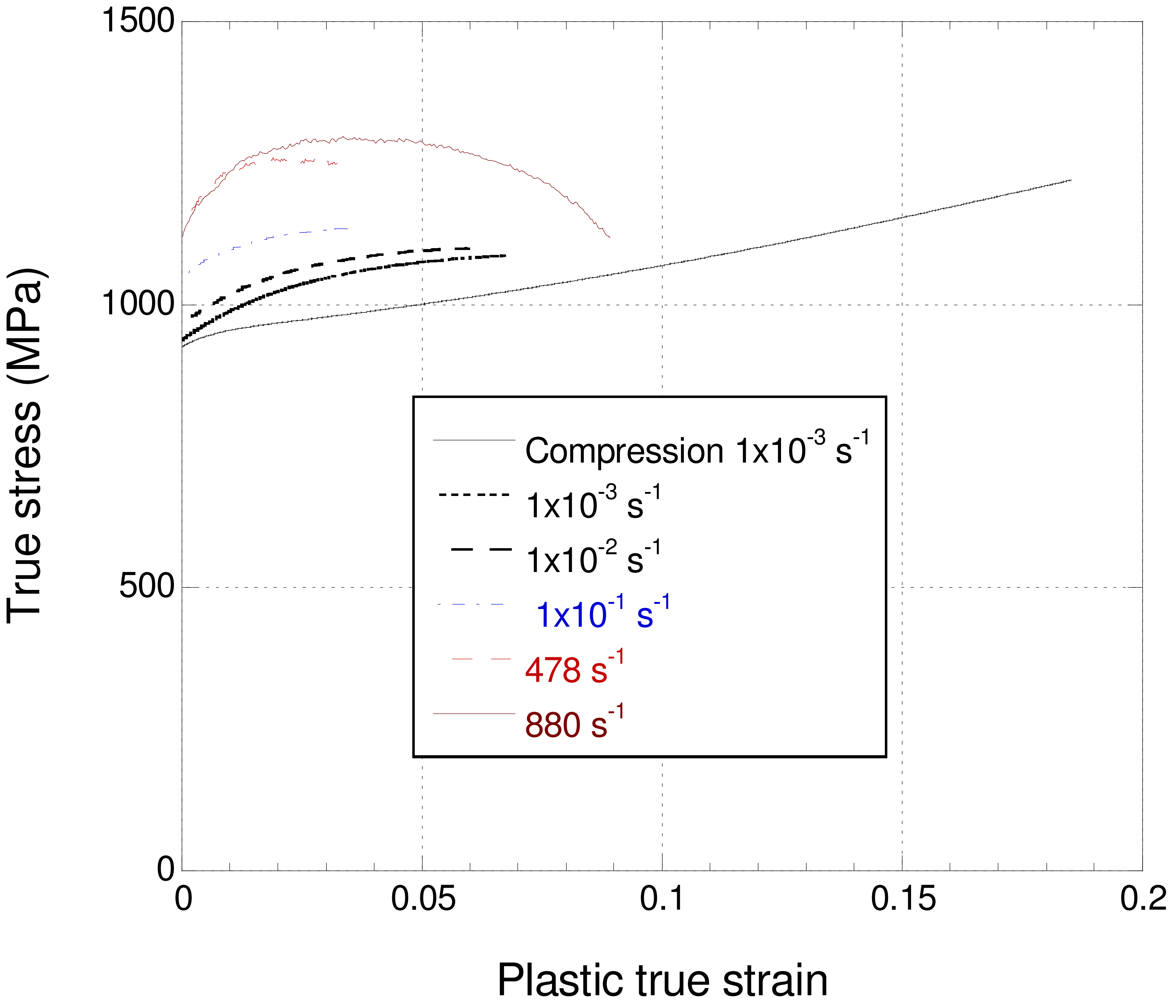

Figure 6.8. Tension plastic true stress-strain curves at different strain rates

6.2. Johnson-Cook Material and Damage Model

6.2.1. JC Material Model Parameter Determination For Compression Tests

As stated earlier, JC equation consists of three brackets which defines the effect of the strain, strain rate and temperature on the flow curve of the tested material. The first bracket includes the parameters related with the flow curve at the reference strain rate. The first bracket ($A+B\varepsilon^n$) is determined from the quasi-static compression test at the reference strain rate of $1\text{x}10^{-3}$ s^{-1}. For this purpose, true plastic stress-strain curves are calculated for each test performed. The plastic strain is calculated by subtracting the elastic strain from the total strain as depicted in Figure 6.9. For the reference strain rate, average stress-strain curves are calculated and this average stress values are fitted with $(A+B\varepsilon^n)$ as shown in Figure 6.10. The fitting parameters for the compression, A, B and n are shown in the same graph: A=927 MPa, B=1150 MPa and n=0.8744.

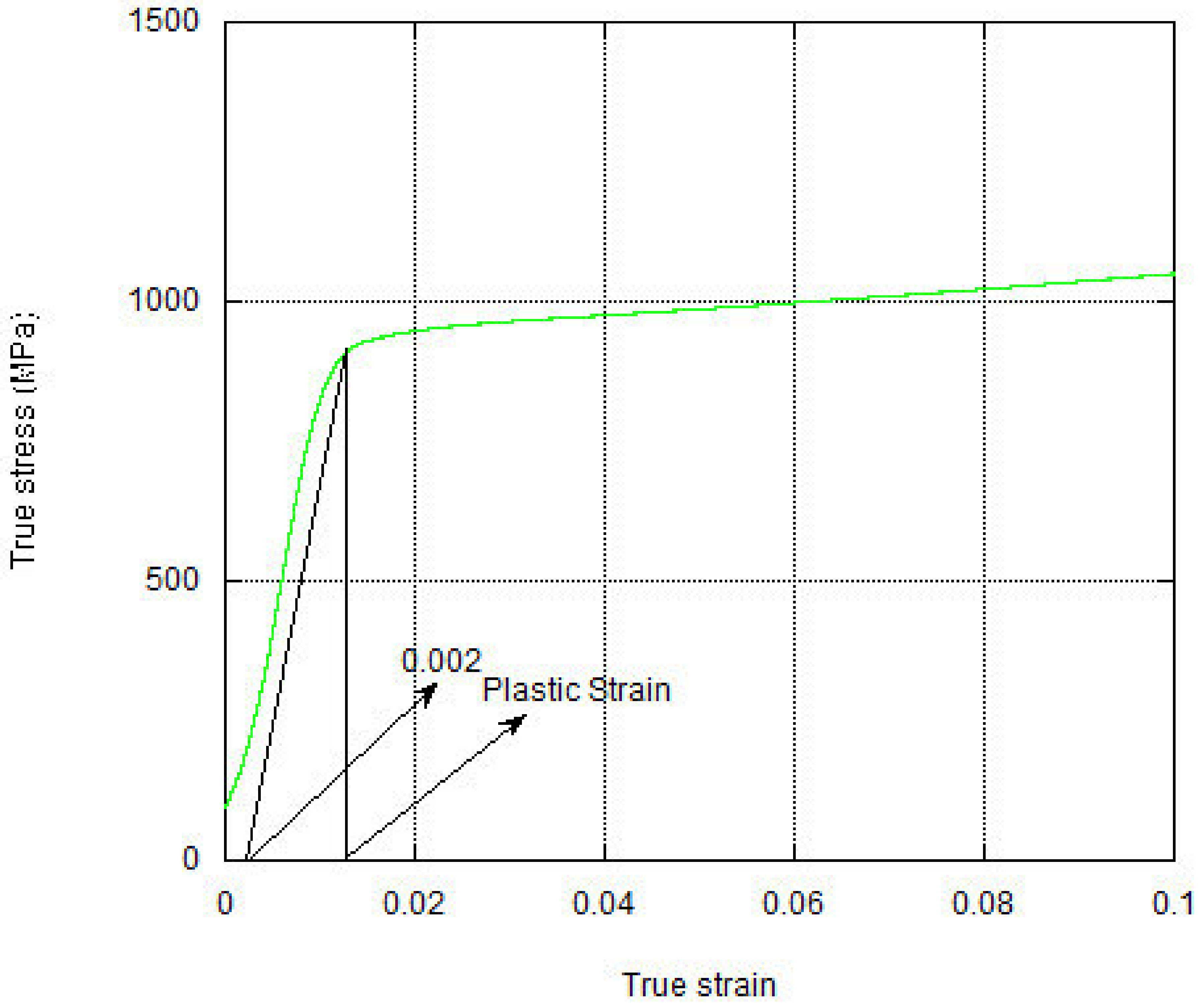

Figure 6.9. True stress-strain curve of compression test at reference strain rate

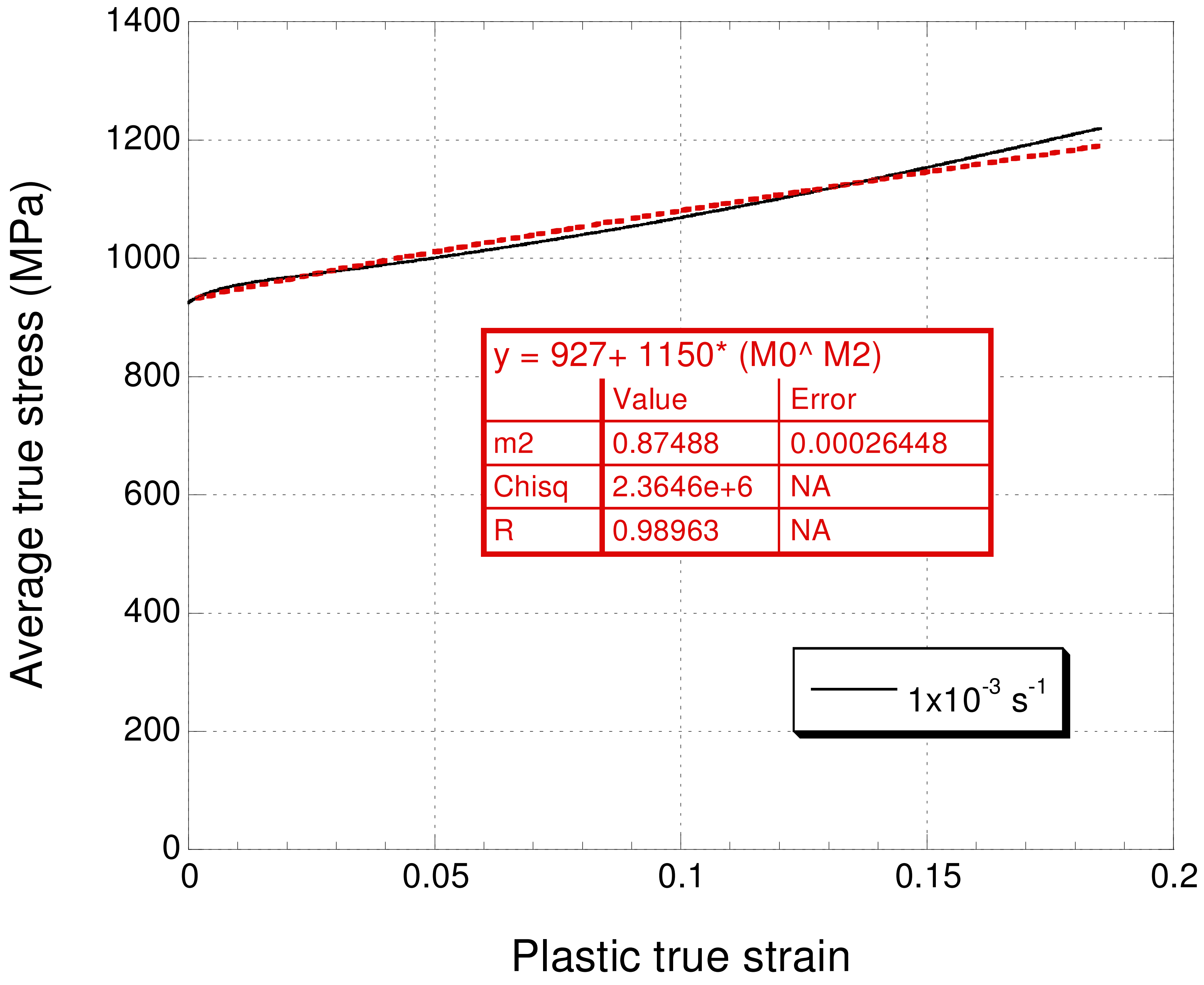

y = 927+ 1150* (M0^ M2)

	Value	Error
m2	0.87488	0.00026448
Chisq	2.3646e+6	NA
R	0.98963	NA

Figure 6.10. True plastic stress versus true plastic strain

Figure 6.11. shows typical compression high strain rate stress-strain rate-strain curve of the studied alloy. As noted in Figure 6.11., the strain rate in a dynamic test is not constant and varies with strain. The variance is about ±100 s^{-1} for each test and therefore an average strain rate is calculated for the each dynamic test performed. For the second parentheses which show the strain rate effect on the deformation, the yield stress values are drawn as function strain rate as shown in Figure 6.12. The data in Figure 6.12 is then witted with the following relation

$$(A+B\varepsilon^{n})=(927+1150\varepsilon^{0.87448}) \tag{6.1}$$

JC compression model parameters of Ti6Al4V are further tabulated in Table 6.1. Figure 6.13. shows the model and experimental stress-strain curves at different strain rates. If one ignores the softening due to adiabatic heating at large strains, the experimental and model stress-strain curves are essentially very much similar. Figure 6.13 compares experimental and model stress-strain curves at different strain rates. At last to check the reliability of the model parameters we compared with the real tests result with the model results as in Figure 6.13 model and experimental stress values are very much similar particularly at relatively low strains. At increasing strain levels, the model stress values deviates from the experimental stress values, resulted from the material softening due to adiabatic heating.

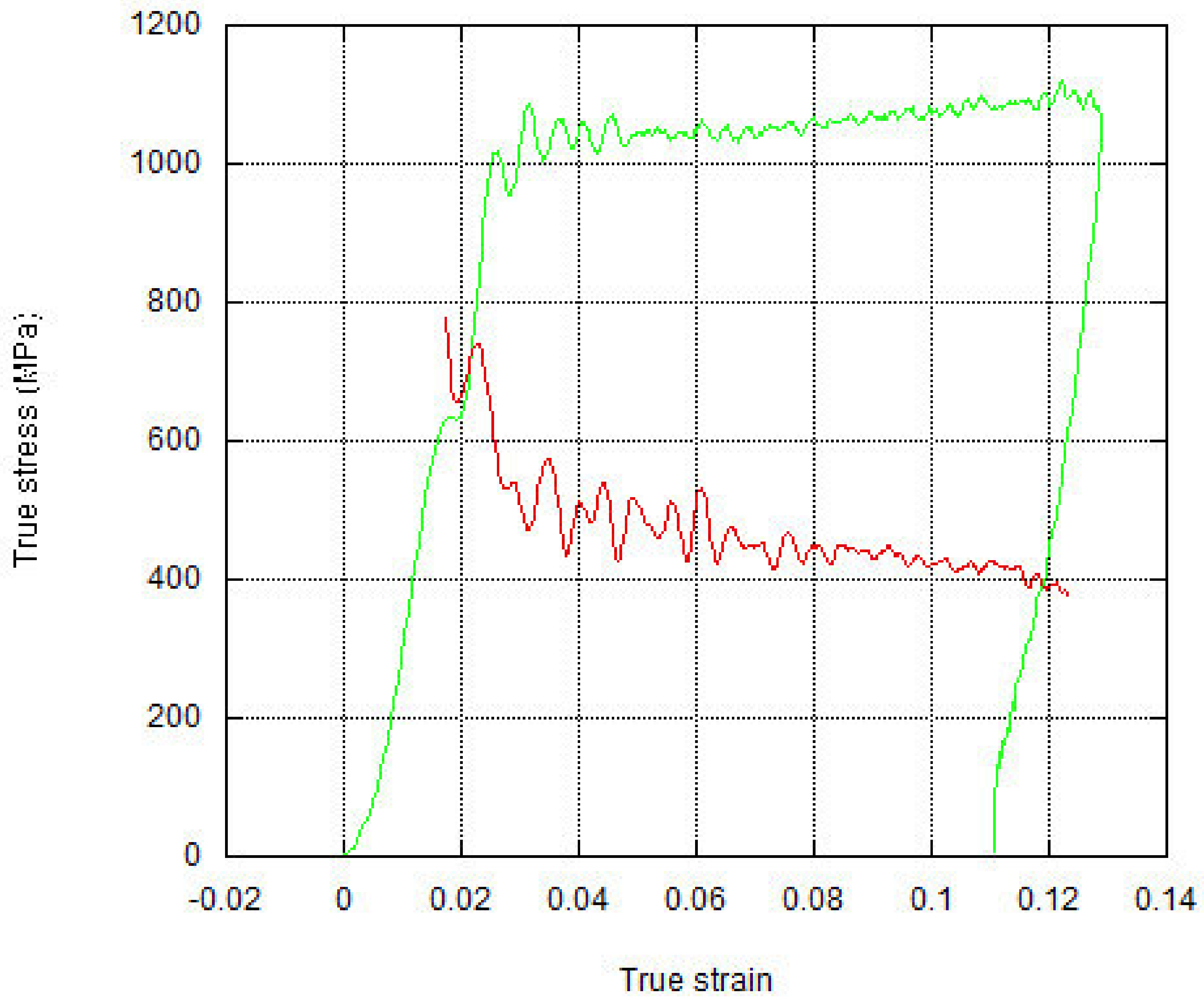

Figure 6.11. True stress-strain rate versus true strain graphics for dynamic test at strain rate 495 s^{-1}

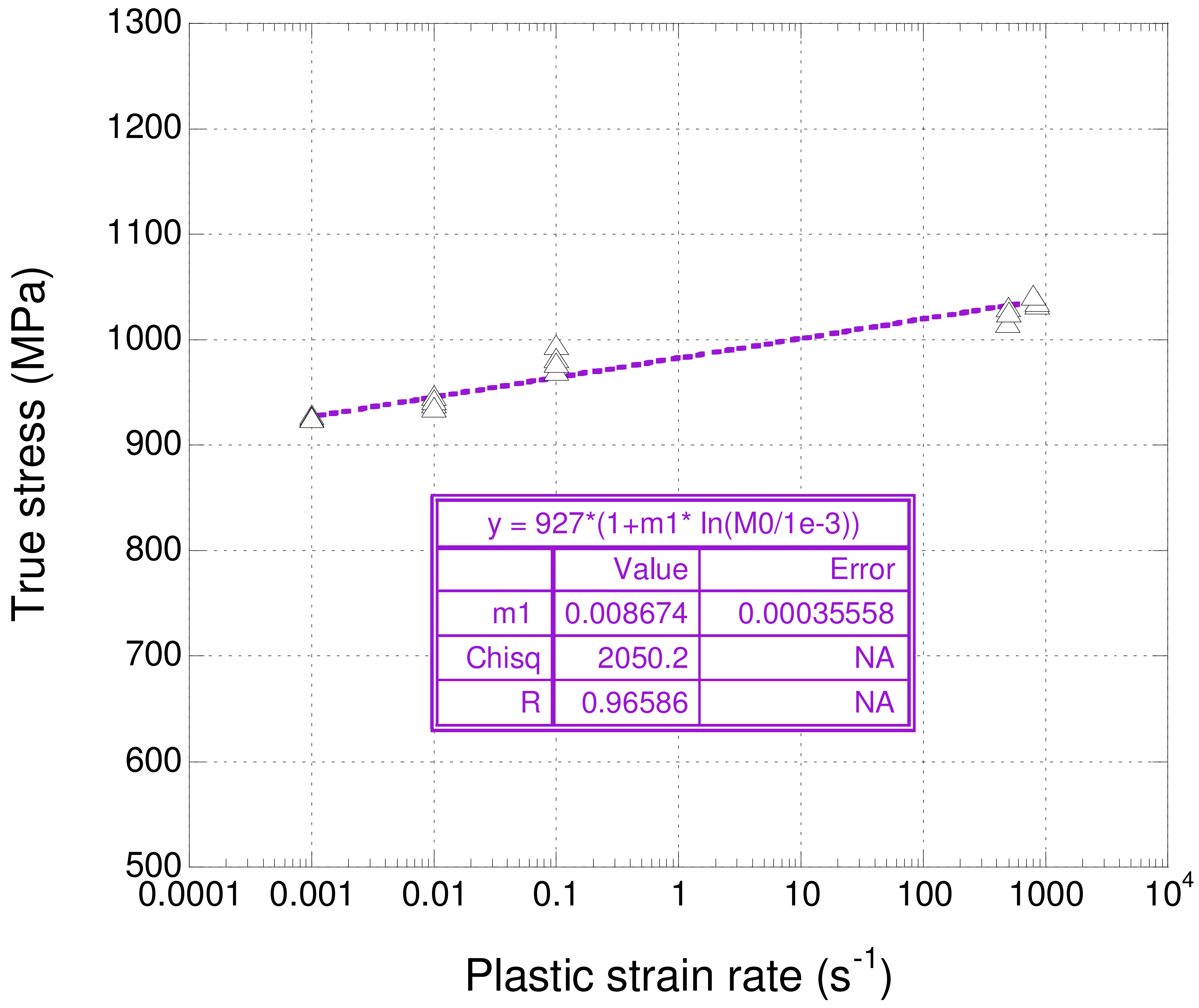

Figure 6.12. True plastic stress versus true plastic strain rate curve for compression

Table 6.1. JC Model parameter defined for compression tests of Ti6Al4V

A (MPa)	**B(MPa)**	**c**	**n**	**ε_0 (s^{-1})**
927	1150	0.008674	0.8674	$1x10^{-3}$

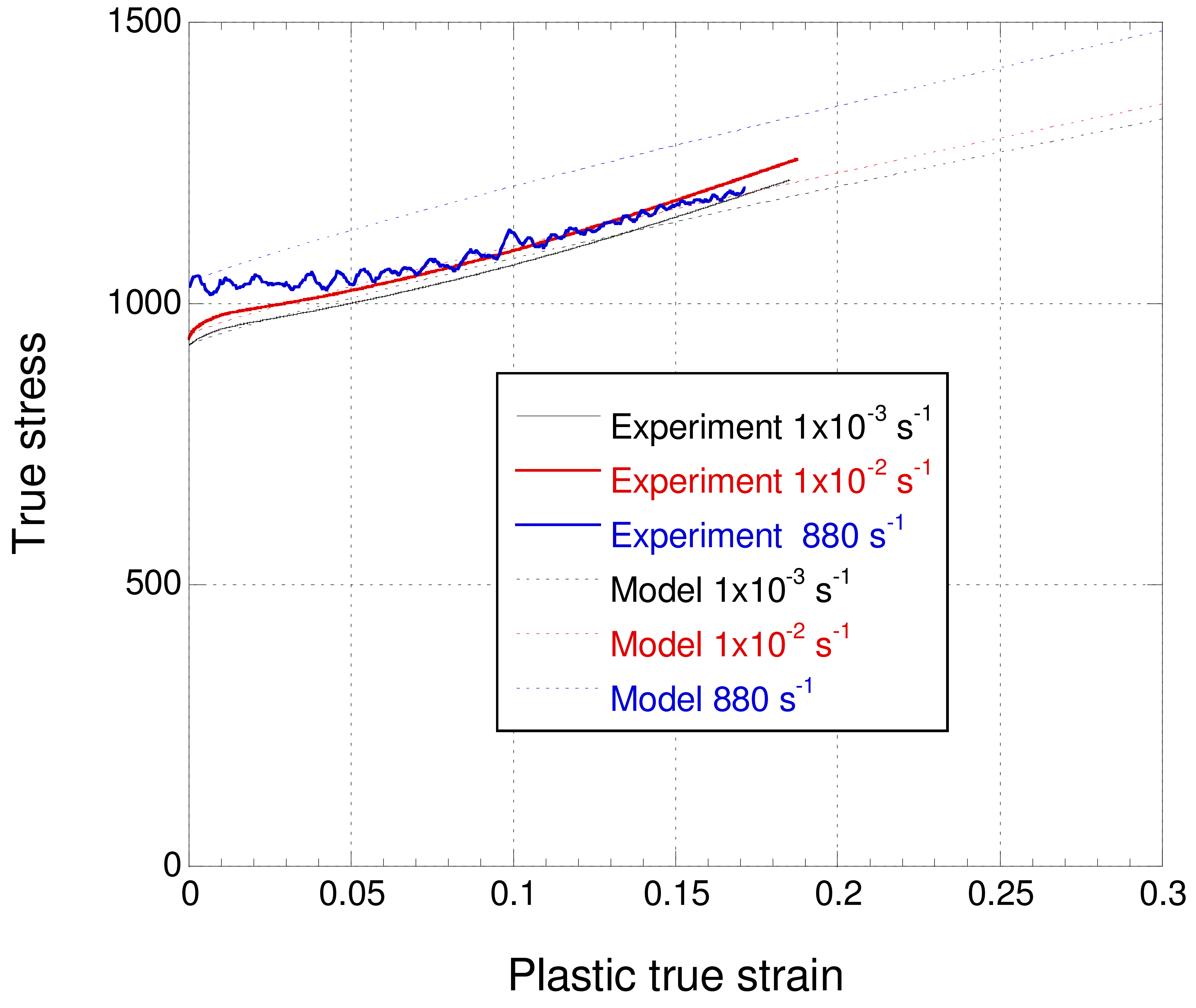

Figure 6.13. Comparison of true stress versus true plastic strain results of model and experiments

6.2.2. JC Material Model Parameter Determination For Tension Tests

The same strategy as with compression tests is applied to tension test stress-strain curves to obtain JC material model parameters. The first bracket, $(A + B\varepsilon^{n})$, of JC model is determined using the average true stress-strain curve at the reference strain rate (Figure 6.13.). The fitting is performed until about 0.035 strain since above this strain level necking starts and the stress values gradually decreases. The first bracket of the JC equation for tension is found as,

$$(A + B\varepsilon^{n}) = (927.8 + 1150\varepsilon^{0.8674}) \tag{6.2}$$

Similar to dynamic compression strain rates, the tension dynamic strain rates vary with strain (±50 s^{-1}). Therefore, an average strain rate is calculated for the each dynamic test performed. In addition, the adiabatic heating effect is considered negligible for the tension tests as the material necks down at relatively low strains before any significant adiabatic heating. For the determination the parameters of the second bracket of JC equation true plastic stress versus fitted with

$$- \qquad (6.3)$$

The witted curve is shown in Figure 6.14. JC tension model parameters of Ti6Al4V are further tabulated in Table 6.2. Figure 6.15 shows the model and experimental stress-strain curves at different strain rates. As seen in Figure 6.15, the model and experimental stress-strain curves are very much similar and show the capability of the model to predict the stress-strain behavior at varying strain rates.

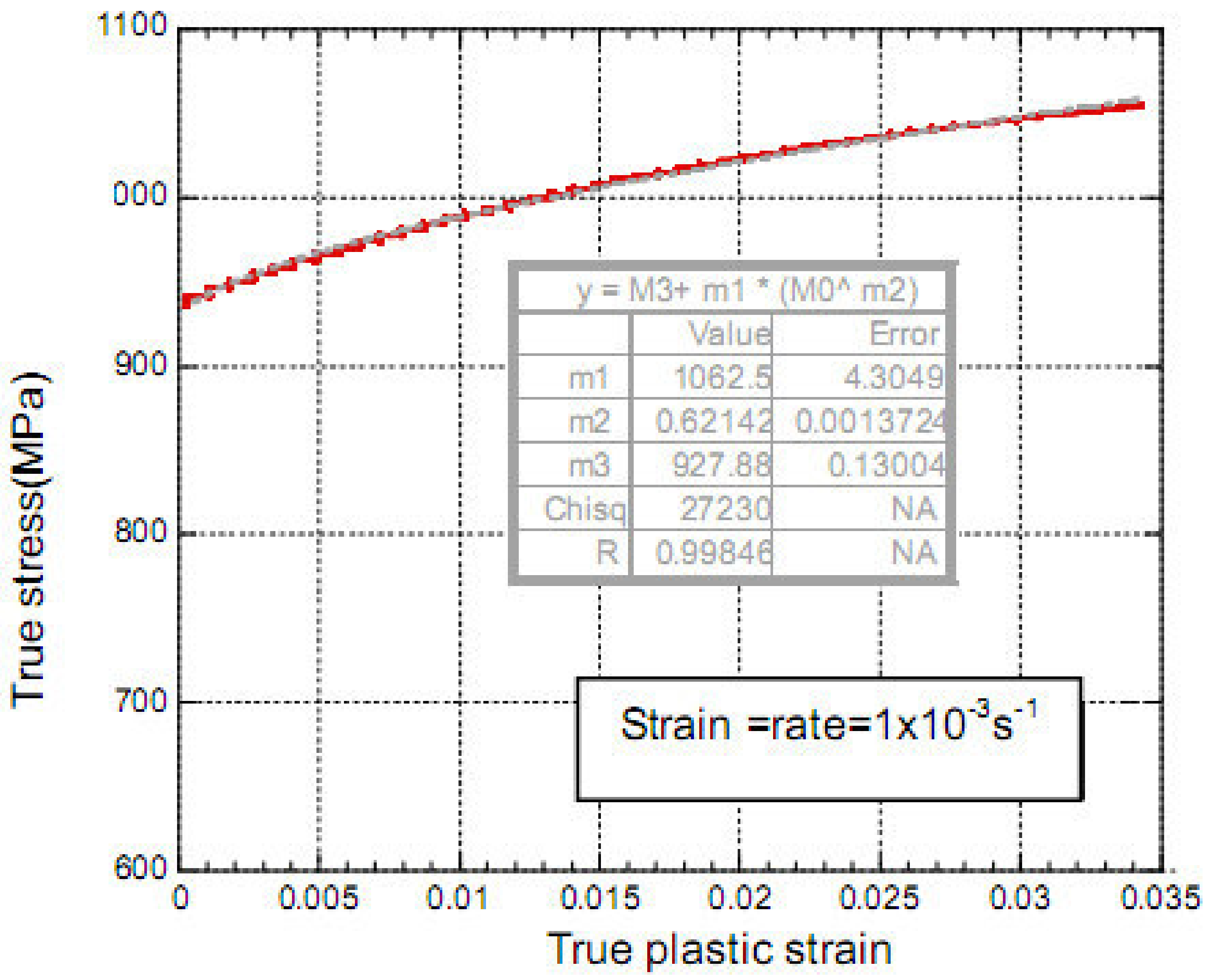

Figure 6.14. True plastic stress versus true plastic strain curve at reference strain rate

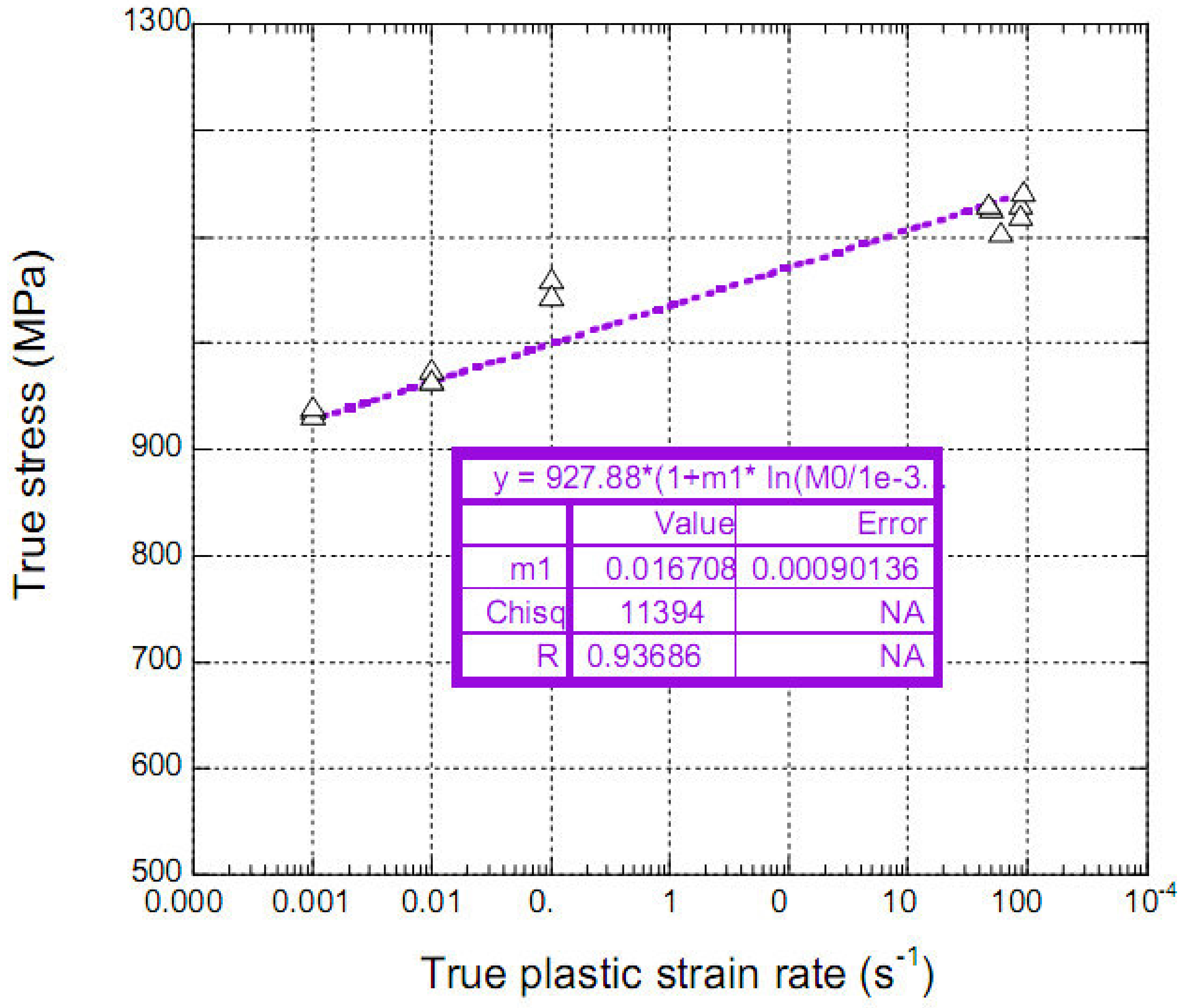

Figure 6.15. True plastic stress versus true plastic strain rate curve for tension

Then the parameters determined for the tension test listed in Table 6.2.

Table 6.2. JC parameters determined for tension tests

A (MPa)	**B(MPa)**	**c**	**n**	**ε_o (s^{-1})**
927.88	1062.5	0.0167	0.6214	1x10^{-3}

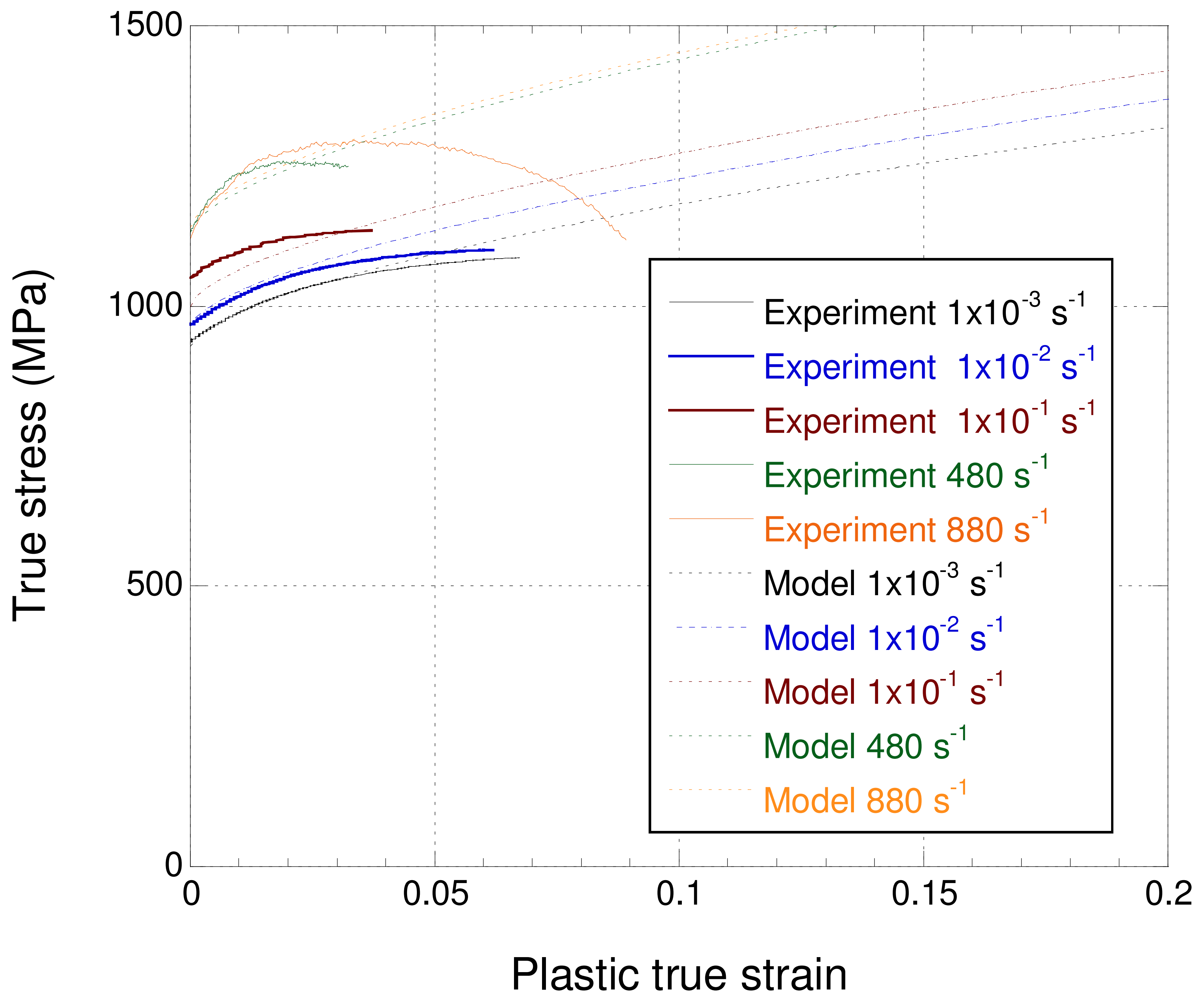

Figure 6.16. Comparison of true stress versus true plastic strain results of model and experiments

6.2.3. High Temperature Tests

The third bracket of the JC material model relates the temperature effect with the flow curve of the material. Quasi-static (1x10^{-3} s^{-1}) high temperature tests were performed at temperatures of 500 °C, 950 °C, 1050 °C and 1100 °C. The stress-strain curves of the alloy at the tested temperatures are shown in Figure 6.16. and 6.17.

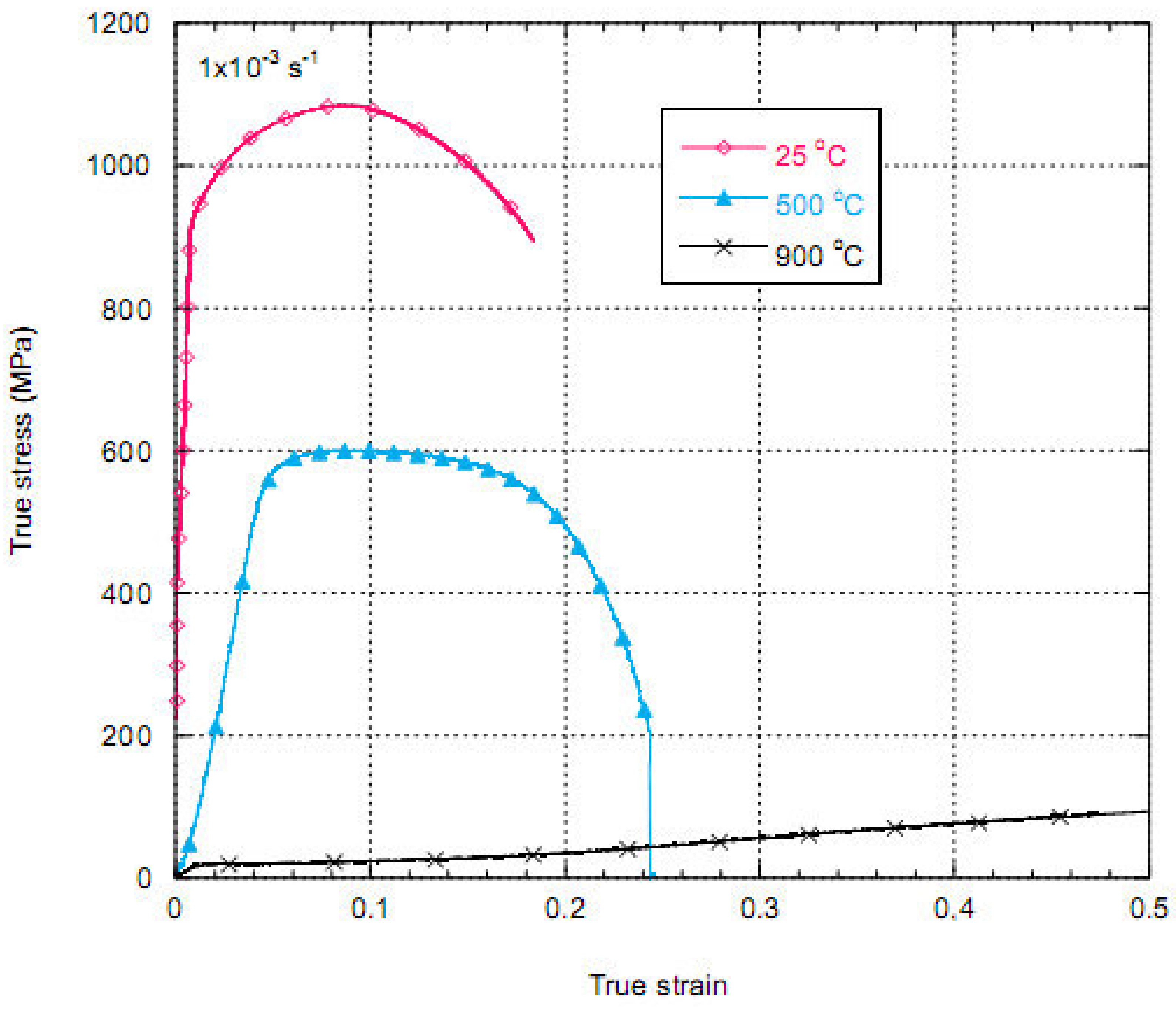

Figure 6.17. True stress-true strain graph of high temperature tension test at reference strain rate (10^{-3} s^{-1})

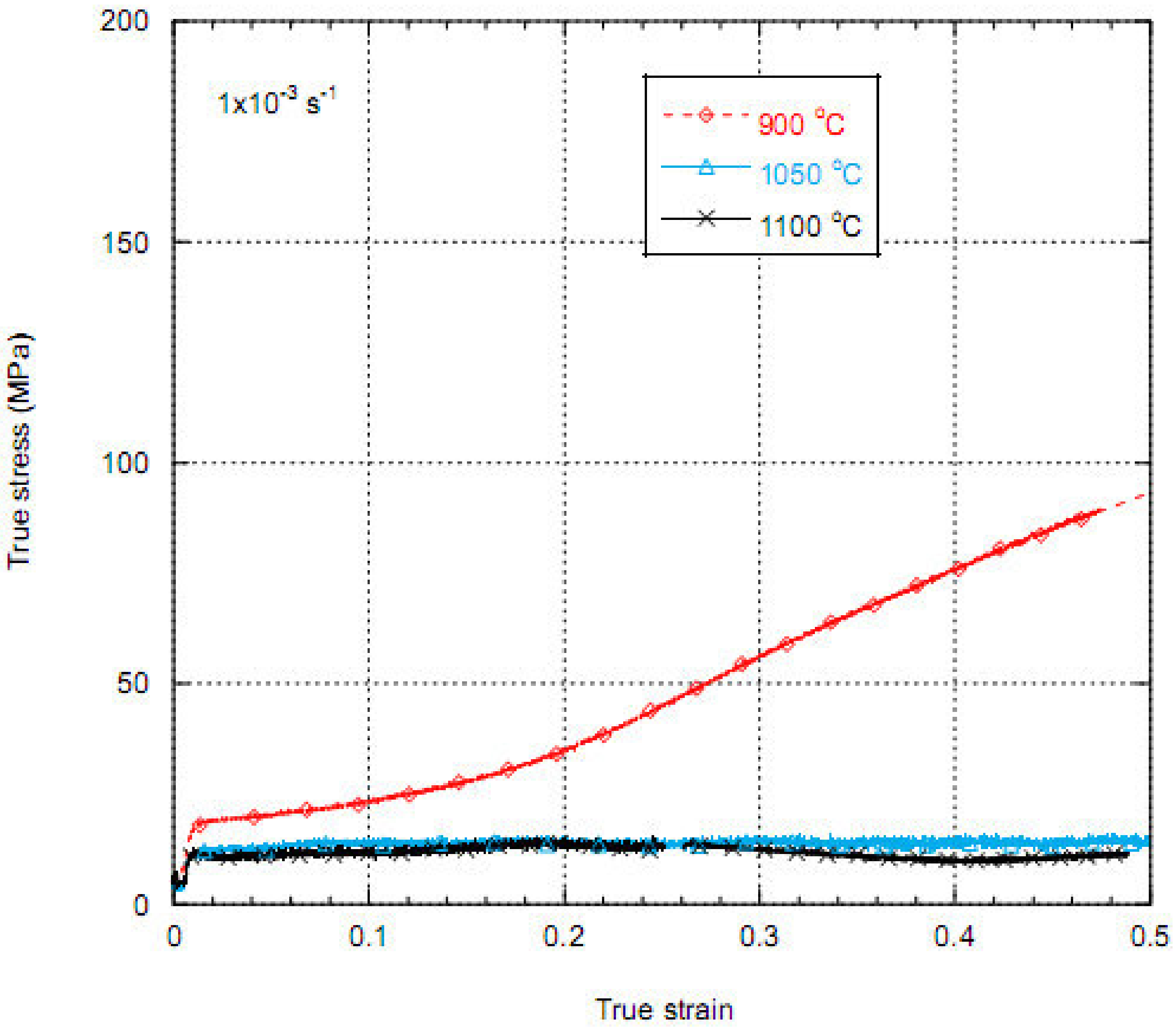

Figure 6.18. True stress-true strain graph of high temperature tension test at reference strain rate (10^{-3} s^{-1})

In high temperature tests, SHPB incident and transmitter bar heated up with the specimen. The temperature increase affects the strain and stress values at high strain rates. Since the strain measurements are taken some distance from the specimen, the strain values should be corrected for the correct values. The following formulations are used to correct stress and strain values;

$$\sigma = \sigma_o (1 - C)^{1/4} \tag{6.4}$$

$$\varepsilon = \varepsilon_o (1 - C)^{-3/4} \tag{6.5}$$

$$C = \alpha (T - T_o) \tag{6.6}$$

where, α is the thermal diffusivity, T is sample temperature and To is the room temperature. The correction factors for the used SHPB are shown in Figure 6.18 as function of temperature.

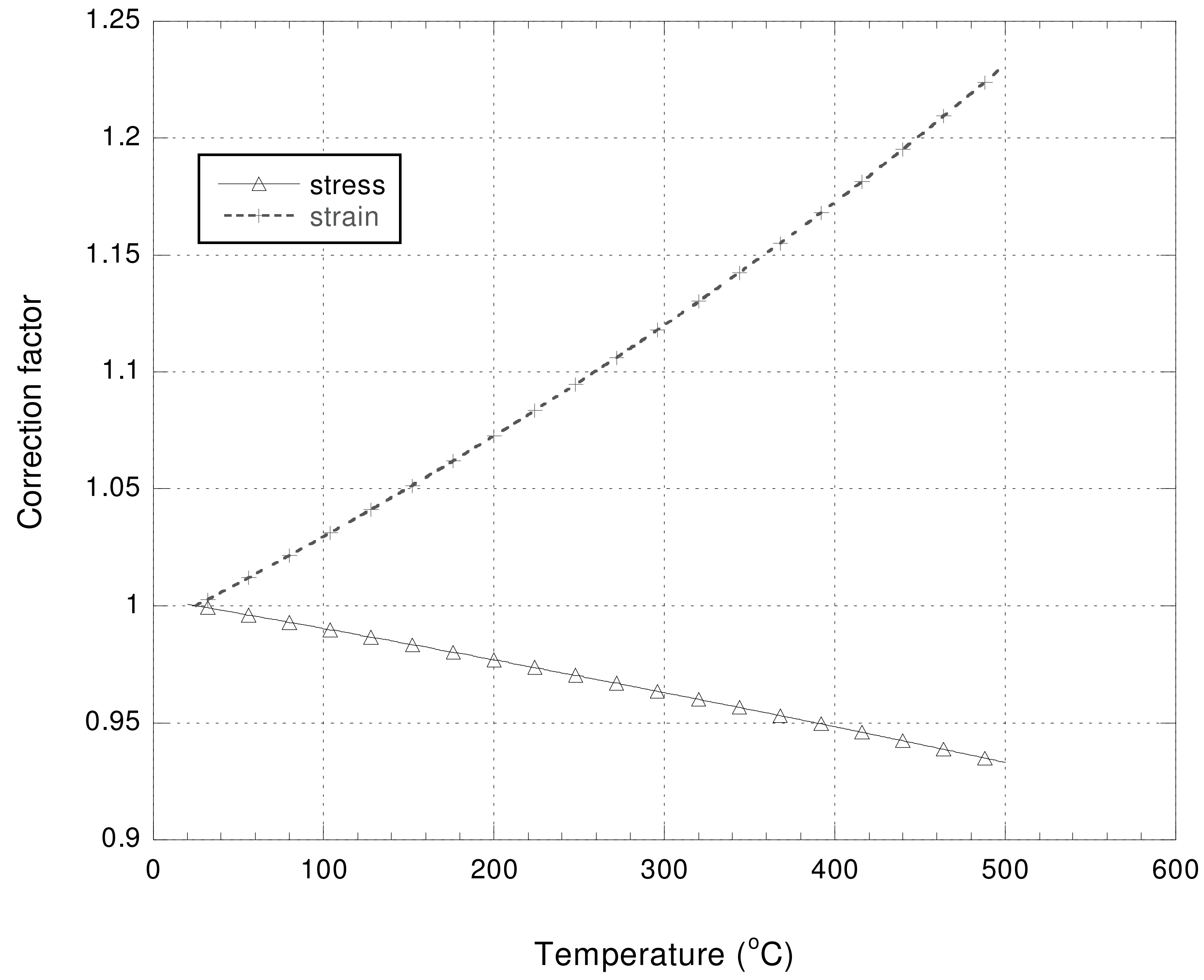

Figure 6.19. Correction factors-temperature curve for inconel bars

Figure 6.19 shows the variation of the yield strength with T^*. In Figure 6.19, also the yield strength data of the similar alloy taken from Vanderhasten study are also shown (M. Vanderhasten, et al. 2005). Important stress decreased with increasing temperature determined from quasi-static tests results is especially seen after 600 ^{o}C. The reason of this decrease after 600 ^{o}C is related with the change of the microstructure as a result of recrystalization process. In addition, after 800 ^{o}C phase transformation and dislocation climb take place. Due to these facts, the third bracket of the JC model equation is fitted to yield strength data between 25-600 ^{o}C and 800-1100 ^{o}C separately. For the later the reference temperature is taken 800 ^{o}C as seen in Figure 6.20. The JC model parameters between 25-600 ^{o}C and 800-1100 ^{o}C are tabulated in Table 6.3 and 6.4, respectively.

The model stress-strain curve at high strain rate and high temperature is verified by the high temperature stress-strain curve obtained from SHPB as shown in Figure 6.21. Model and experiment give similar stress values as depicted in this figure, showing the consistency between model and experiments.

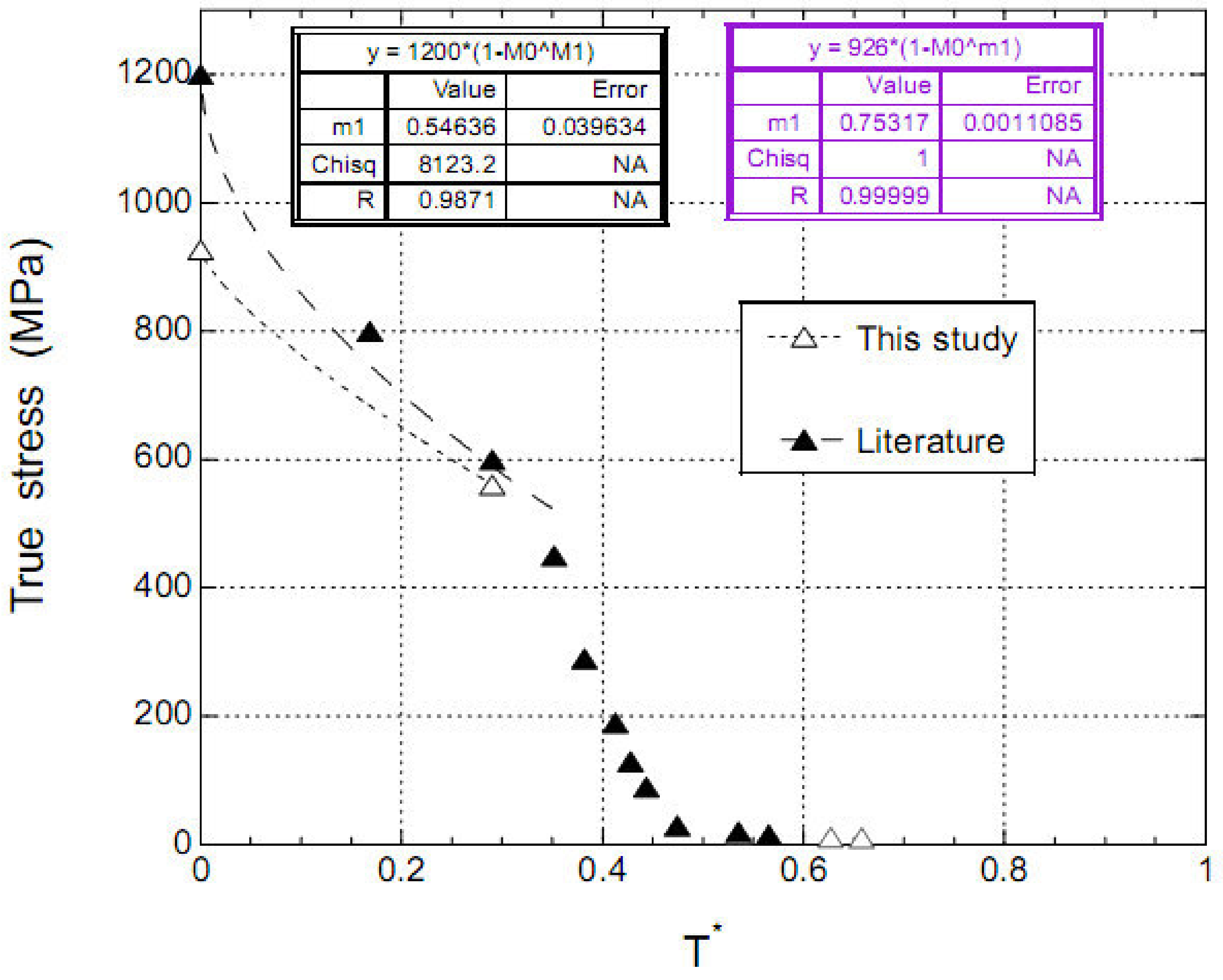

Figure 6.20. True stress-temperature graphs of this study and literature

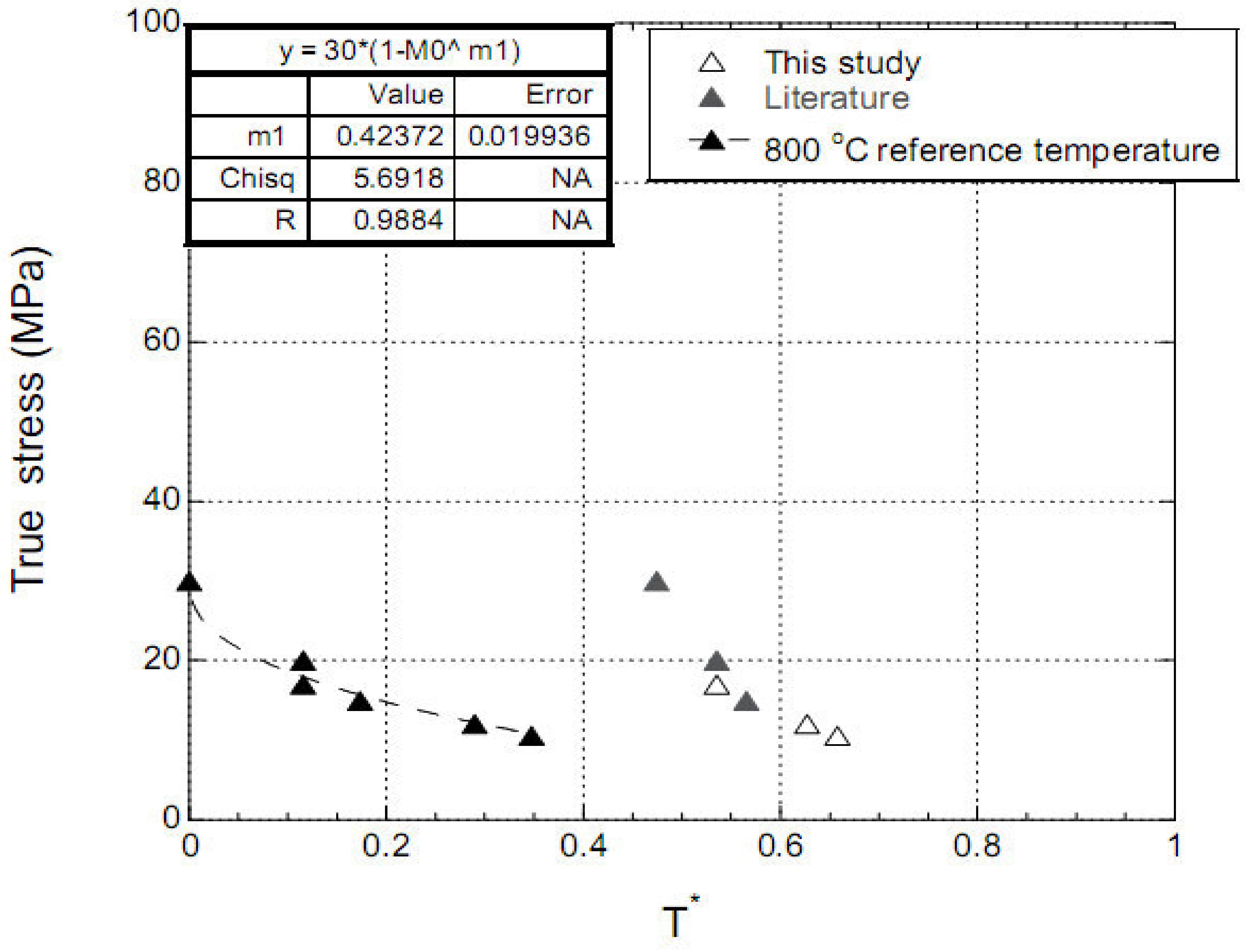

Figure 6.21. True stress-temperature graphs of this study and literature

Table 6.3. JC model parameters between 25 °C to 600 °C

A (Mpa)	**B (Mpa)**	**c**	**n**	**m**	**ε_o (s^{-1})**	T_r (°C)
927	1062.5	0.0167	0.6214	0.753	$1x10^{-3}$	25
927	1150	0.008674	0.8674	0.753	$1x10^{-3}$	25

Table 6.4. JC model parameters between 800 °C to 1100 °C

A (Mpa)	**B (Mpa)**	**c**	**n**	**m**	**ε_o (s^{-1})**	T_r (°C)
30	50	0.0167	0.6214	0.423	$1x10^{-3}$	800

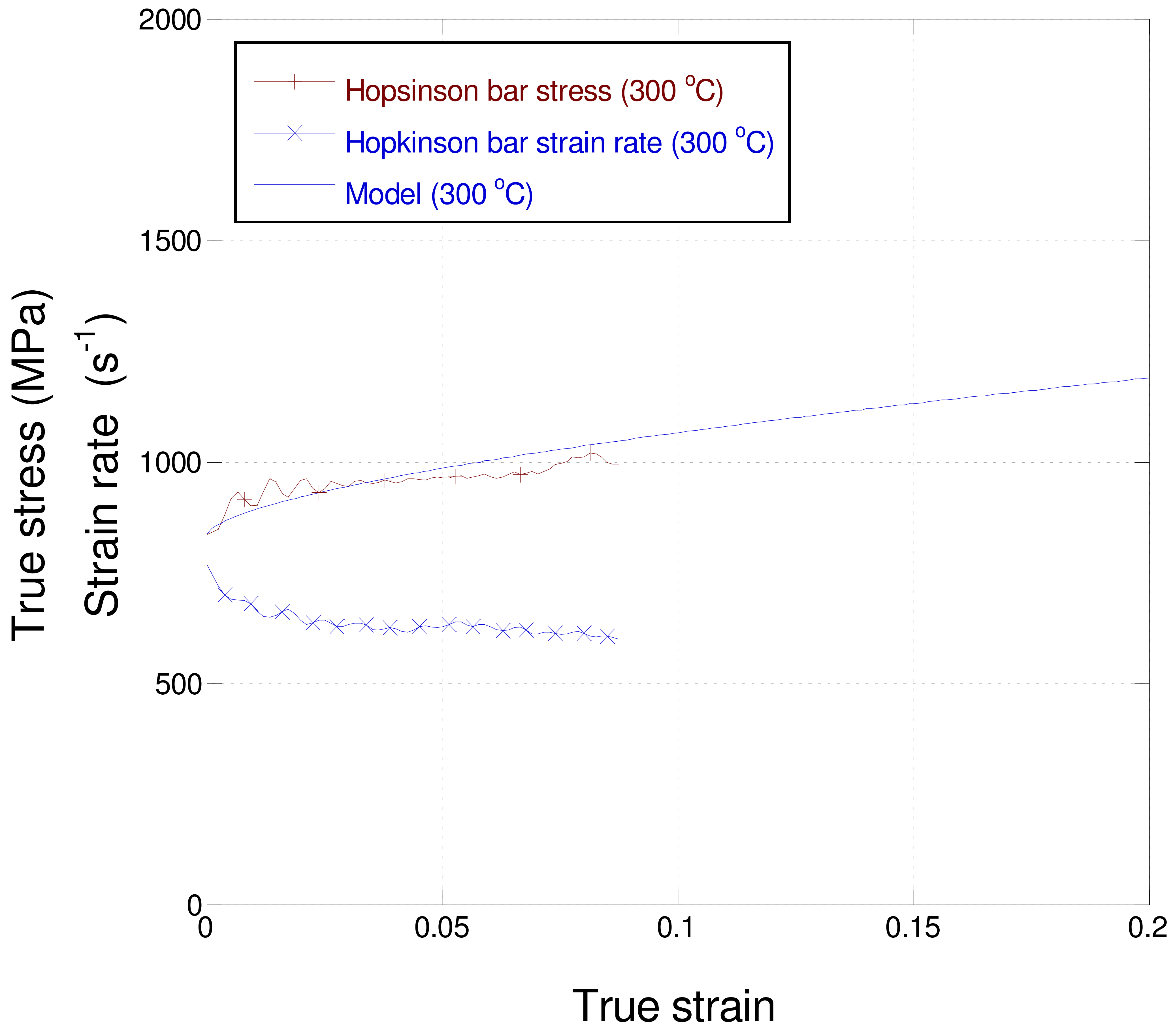

Figure 6.22. True stress-strain rate-true strain graph of high strain rate test

6.2.4. JC Damage Model Parameter Determination

The first bracket in the JC fracture model defines the relation between strain to fracture and hydrostatic tension. As the hydrostatic tension increases, strain to fracture decreases. The second bracket represent the strain rate effect on the failure strain of the material. The third bracket defines the effect of thermal softening on the failure strain. The stress triaxilities, fracture strain, and strain rates of the tested notched samples with different notch radius listed in Table 5.3. Parameters $D_{1,}$ D_2 and D_3 in the first bracket of the JC damage model are determined from the tension tests of the specimens with notch radius of 6 mm, 3 mm and 2 mm at reference strain rate (10^{-3} s^{-1}). The Stress triaxility versus fracture strain graph shown in Figure 6.22 is fitted with $[D_1 + D_2 \exp{(D_3 \dot{\sigma})}]$ (Figure 6.22.). The value of D4 in the second bracket is determined by fitting the fracture strain-strain curve (Figure 6.22.). The determined value of D4 is the average of the three notched samples. Thermal softening parameter D_5 is further determined by fitting tests at various temperatures. The determined JC model parameters are listed in Table 6.23.

Table 6.5. Fracture strains, strain rates and dimensions of the test samples

Strain Rate	**Fracture Strain (Notch Radius 6 mm)**	**Fracture Strain (Notch Radius 3 mm)**	**Fracture Strain (Notch Radius 2 mm)**
$10^{-3}s^{-1}$	0.43779	0.34510	0.30994
$10^{-2}s^{-1}$	0.36341	0.32075	0.29746
$10^{-1}s^{-1}$	0.33143	0.31145	0.27793

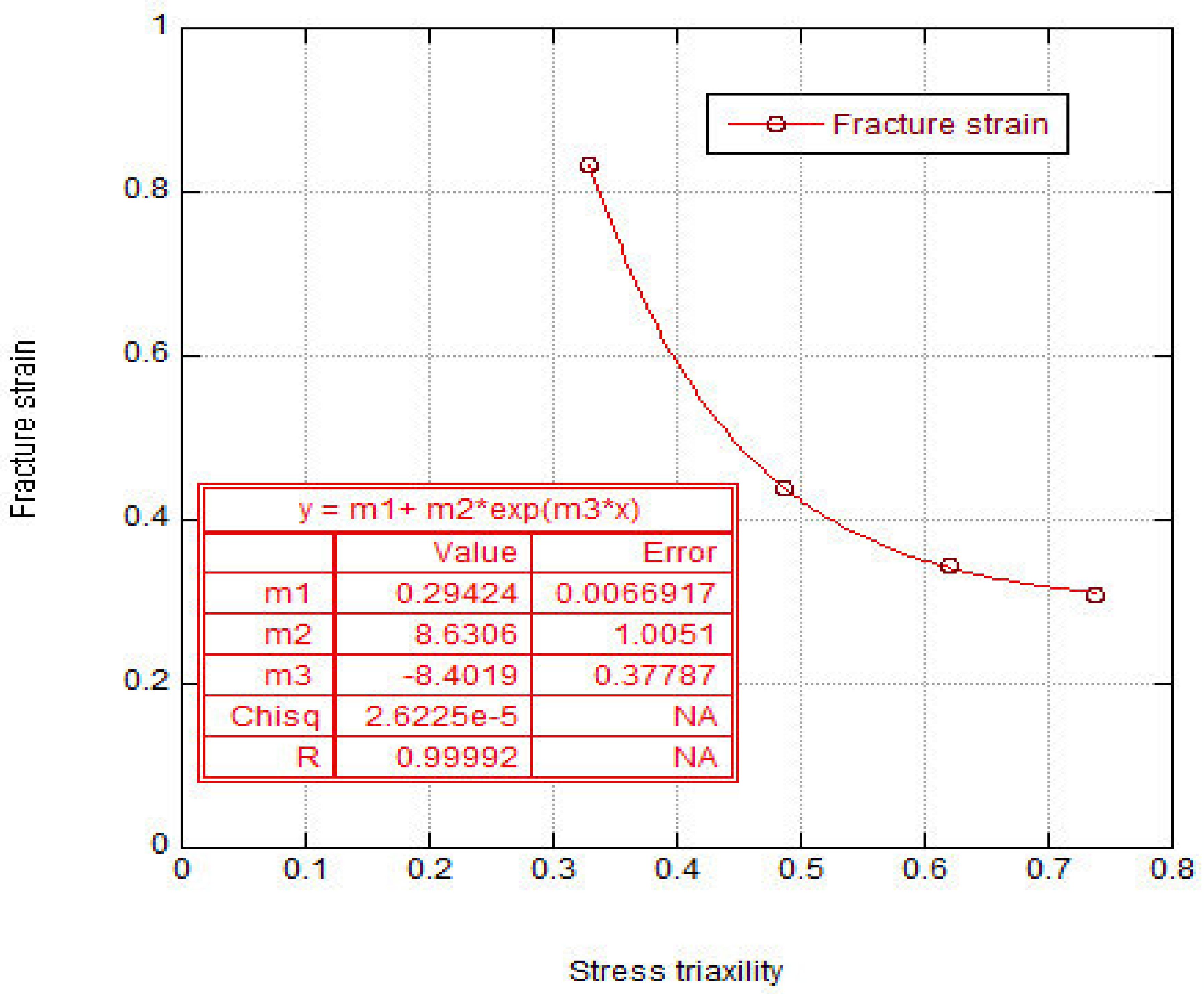

y = m1+ m2*exp(m3*x)

	Value	Error
m1	0.29424	0.0066917
m2	8.6306	1.0051
m3	-8.4019	0.37787
Chisq	2.6225e-5	NA
R	0.99992	NA

Figure 6.23. Fracture stress versus stress triaxility

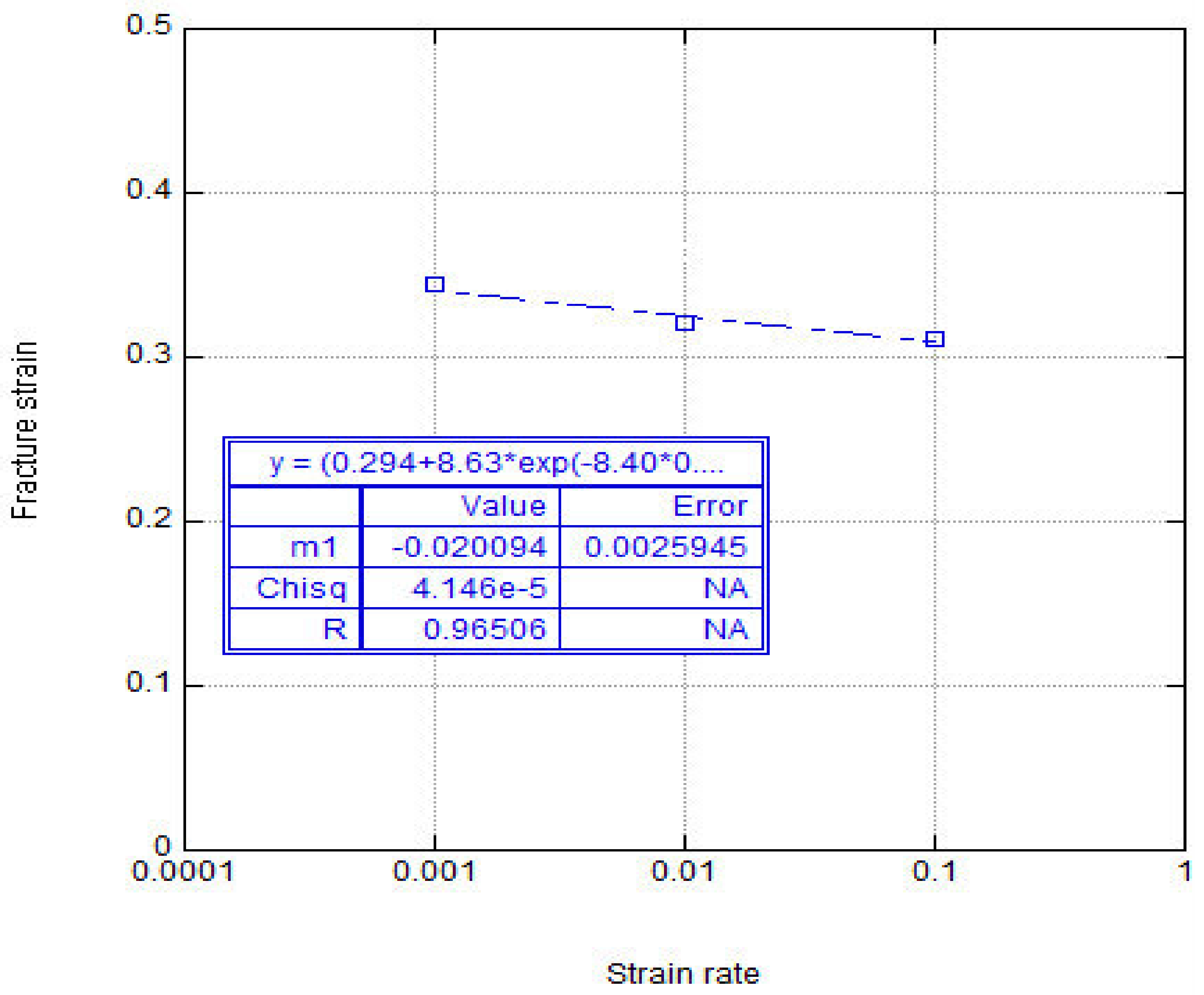

y = (0.294+8.63*exp(-8.40*0....

	Value	Error
m1	-0.020094	0.0025945
Chisq	4.146e-5	NA
R	0.96506	NA

Figure 6.24. Fracture versus strain rate graph for specimen with 3mm notch radius

Table 6.6. JC damage parameters

D1	**D2**	**D3**	**D4**	**D5**	**ε_o (s^{-1})**
0.294	8.63	-8.4	-0.0213	4.22	1x10^{-3}

6.3. Metallographic Examination

Figure 6.22 shows SEM micrograph of tested Ti6Al4V alloy. The structure consists of α and β phases. The EDX result shown in Figure 6.22 confirms that the white phase is β phase as it contains higher V content. Titanium alloy used in this study was reported to be annealed at below β transus temperature. As a result β phase precipitated in α phase.

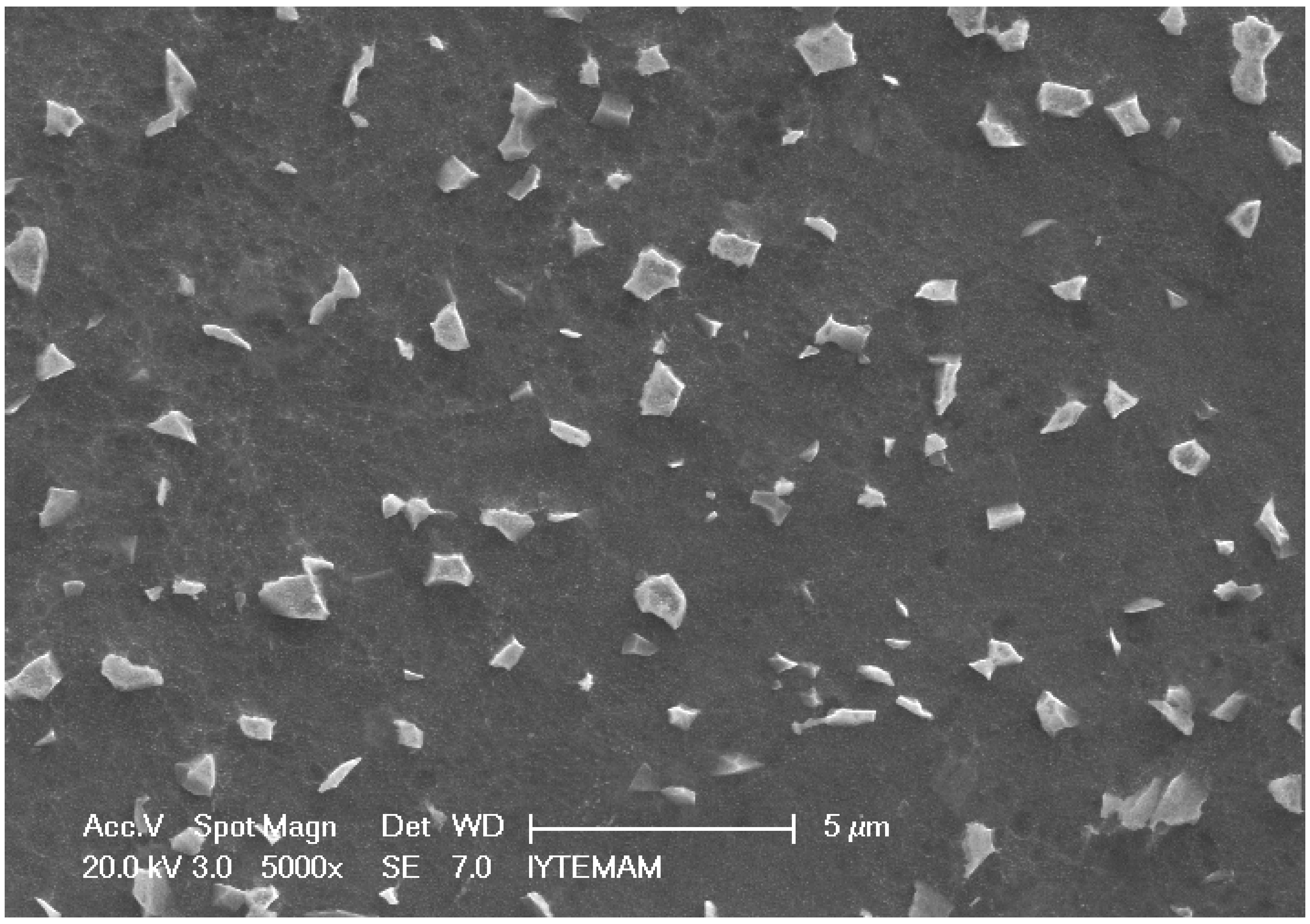

Figure 6.25. Micro-structure of Ti6Al4V alloy with 5000X magnification

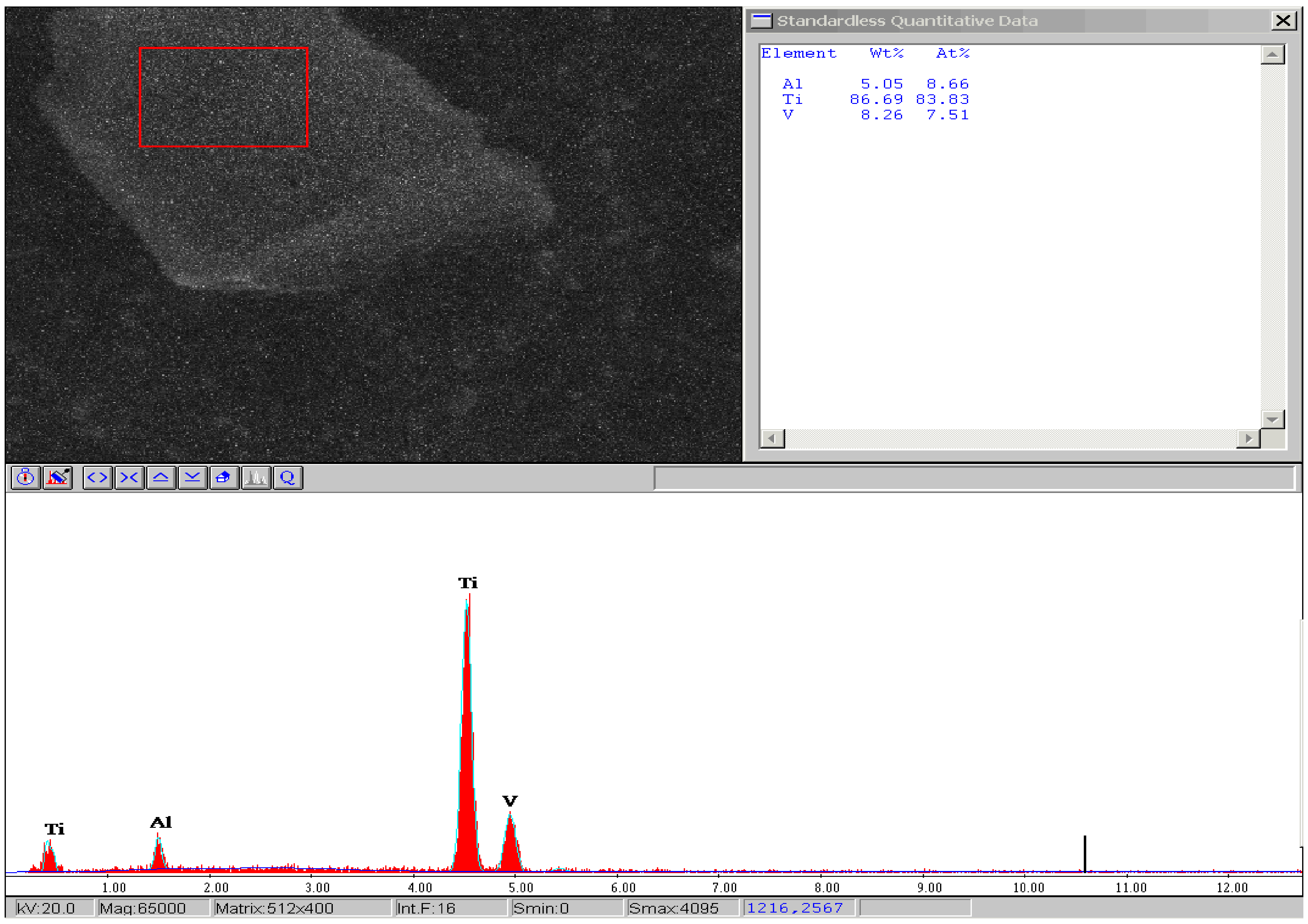

```
Element   Wt%   At%

  Al      5.05  8.66
  Ti     86.69 83.83
  V       8.26  7.51
```

```
kV:20.0  Mag:65000  Matrix:512x400  Int.F:16  Smin:0  Smax:4095  1216,2567
```

Figure 6.26. EDX of the precipitate in Ti6Al4V alloy

The fracture surfaces of the quasi-statically and dynamically tested tensile test specimens are shown in Figure 6.23 and 6.24, respectively. The failure is a cup and cone type of fracture, which is a characteristic fracture type of ductile metals. The dimpled central area of the pictures shows the region of the ductile failure. The voids initiate in the center and progress through ductile failure to the end of the specimen. The flat region around the ductile fracture region is the region of the brittle fracture. The ductile fracture area in quasi-statically tested sample is seen to be larger, proving a more ductile failure at quasi-static strain rates. This also agreed with the measured decline in fracture strain at increasing strain rates. Both crack surfaces contain dimples in the ductile region but the size of the dimples on dynamic test specimen fracture surface are large and distinctive than the static test specimen (Figure 6.25 and 6.26). This also prove a excessive plastic deformation of the static test specimen than dynamic one. When the photos in above figures examined. It can be seen that number of the dimples on the fracture surface of the static tested specimen were more than dynamic one. But the size of the dimles in dynamic specimen greater than static tested specimen. Also dimples in static specimen surface are shallow and smaller than dynamically tested specimen. Deeper dimples would have a direct relationship with the higher values obtained for the reduction area in the sample. SEM micrographs of the quasi-statically and dynamically tested samples are shown sequentially in Figure 6.27 and 6.28, respectively. The side view photographs of dynamic and quasi-static tension test specimens prove that fracture occurs in α phase. β phase is soft and deforms along the applied stress direction. All the side view photographs include bubble like structures and numbers of these structures are more in dynamic tested specimen structure then static. These structures are the point where the dislocations reunite. Also small black points called voids are observable in the photographs.

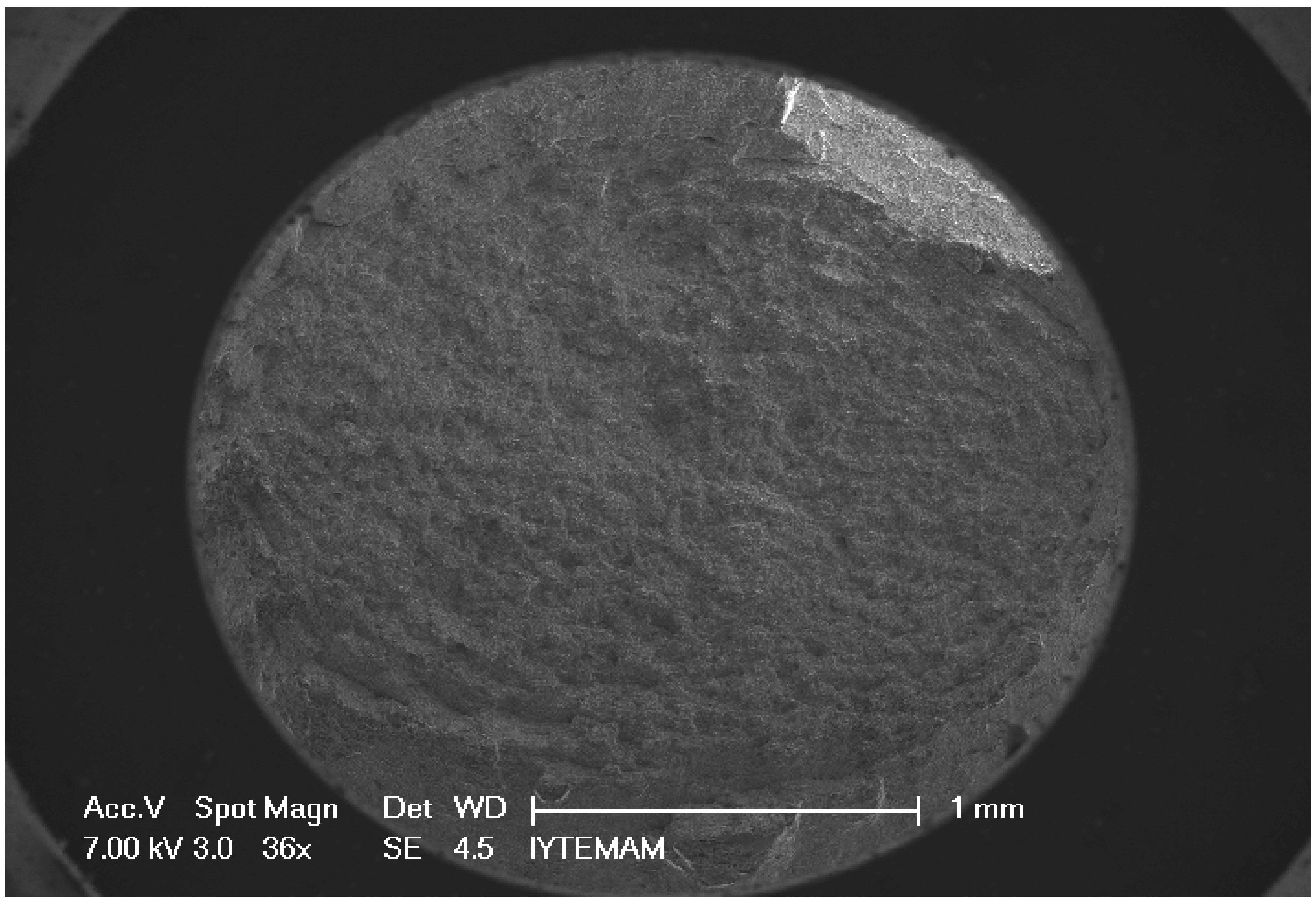

Figure 6.27. Crack surface of quasi-static tension test specimen

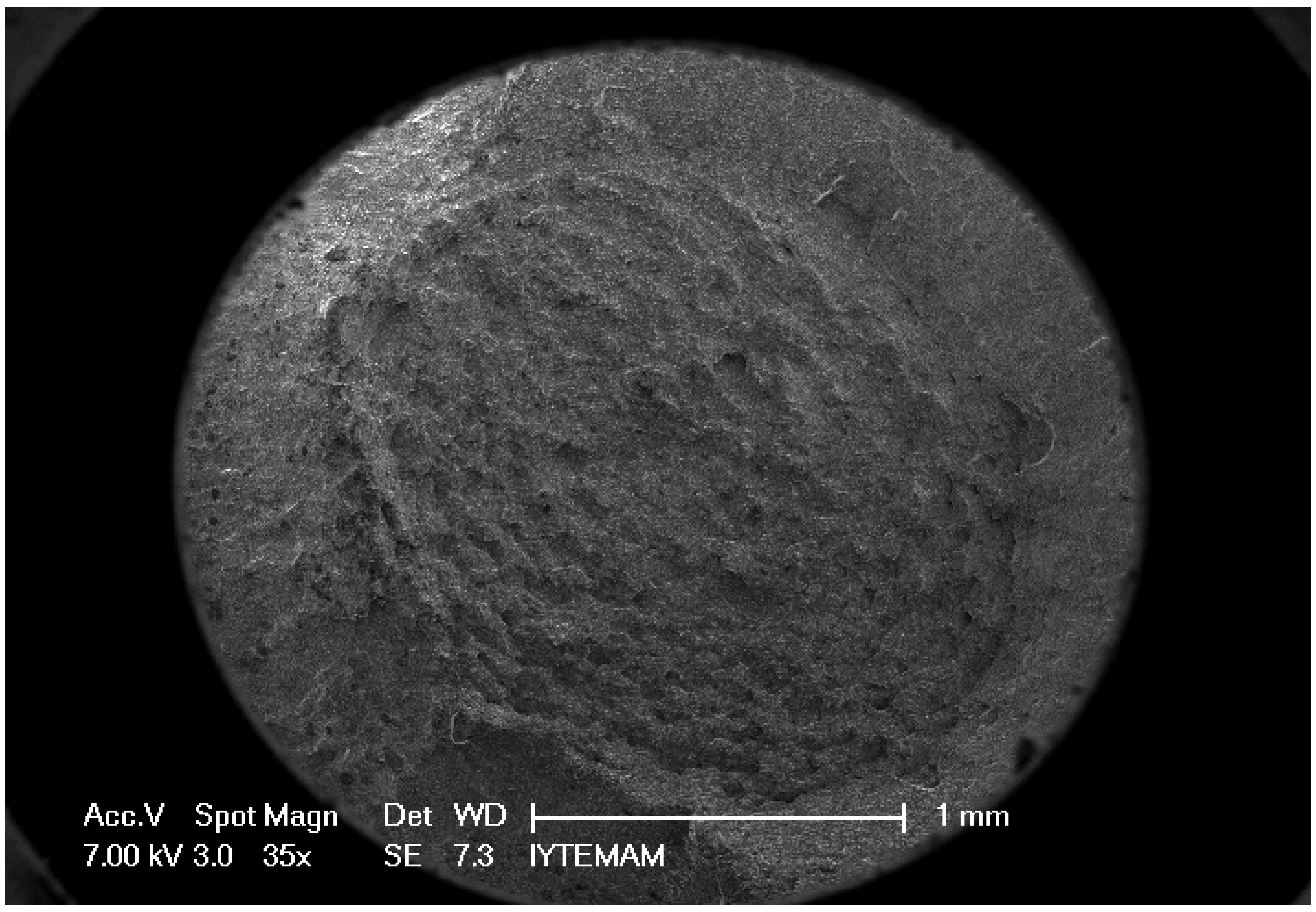

Figure 6.28. Crack surface of dynamic tension test specimen

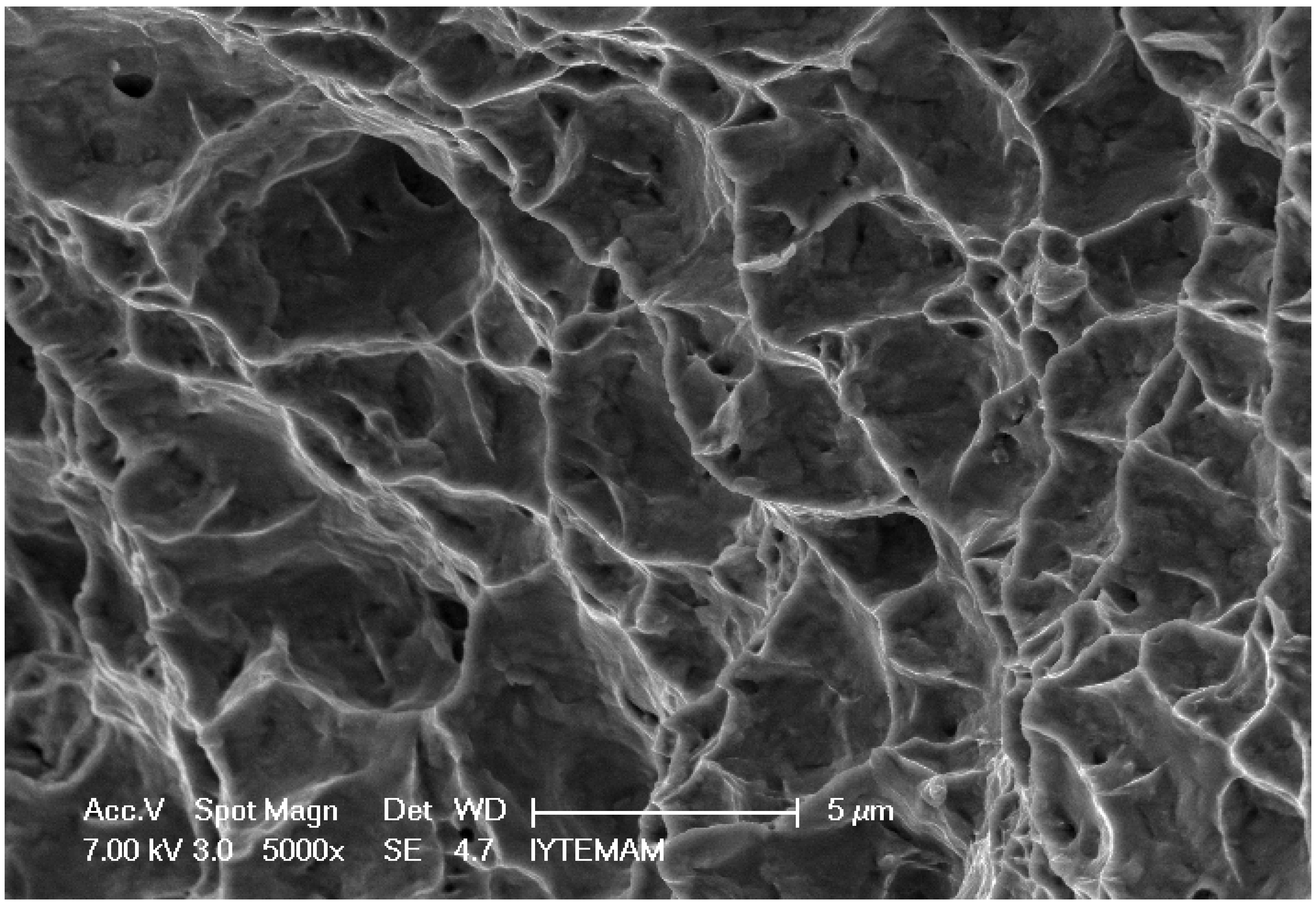

Figure 6.29. Quasi-static tension test specimen fracture surface at 5000X magnification

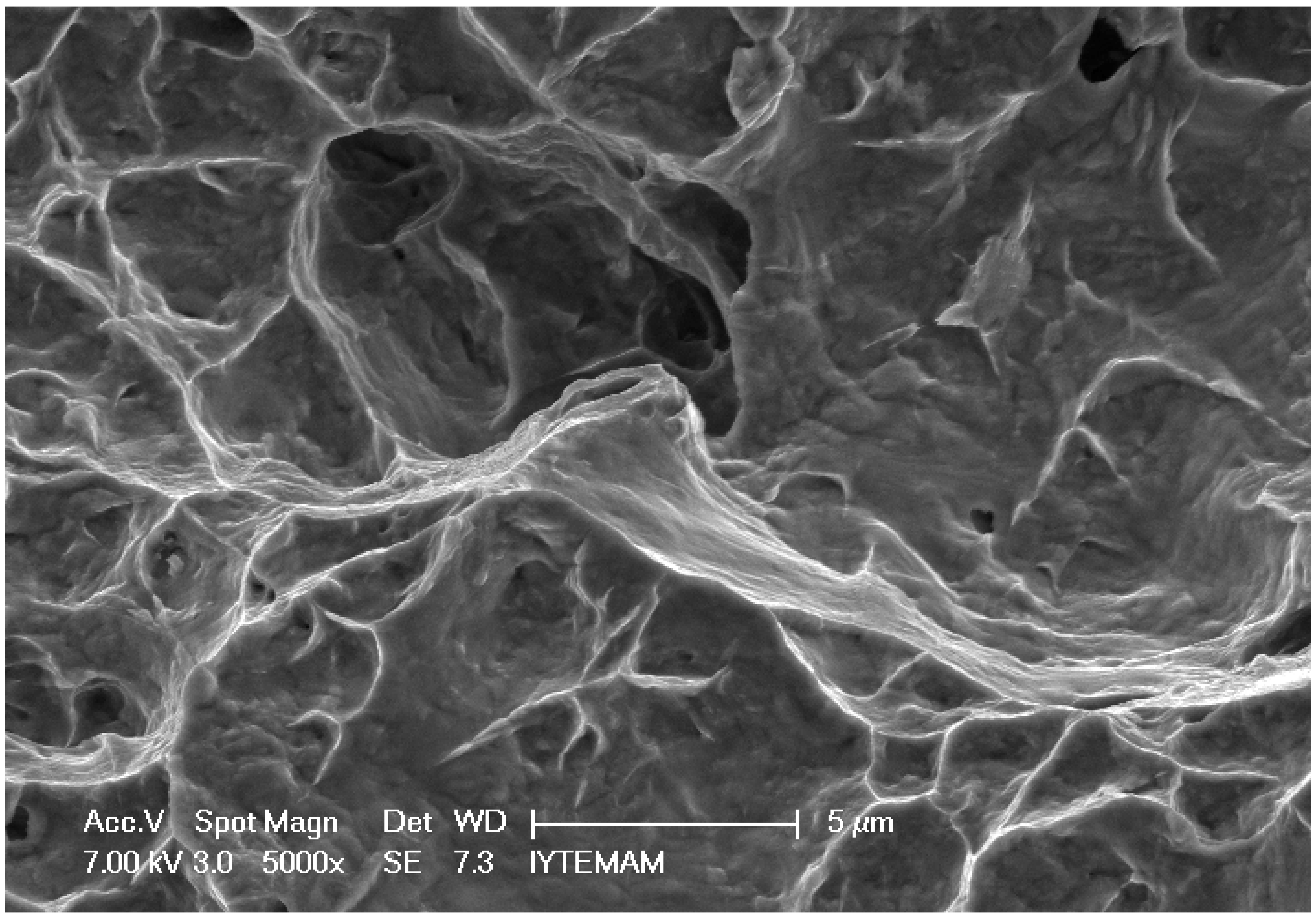

Figure 6.30. Dynamic tension test specimen fracture surface at 5000X magnification

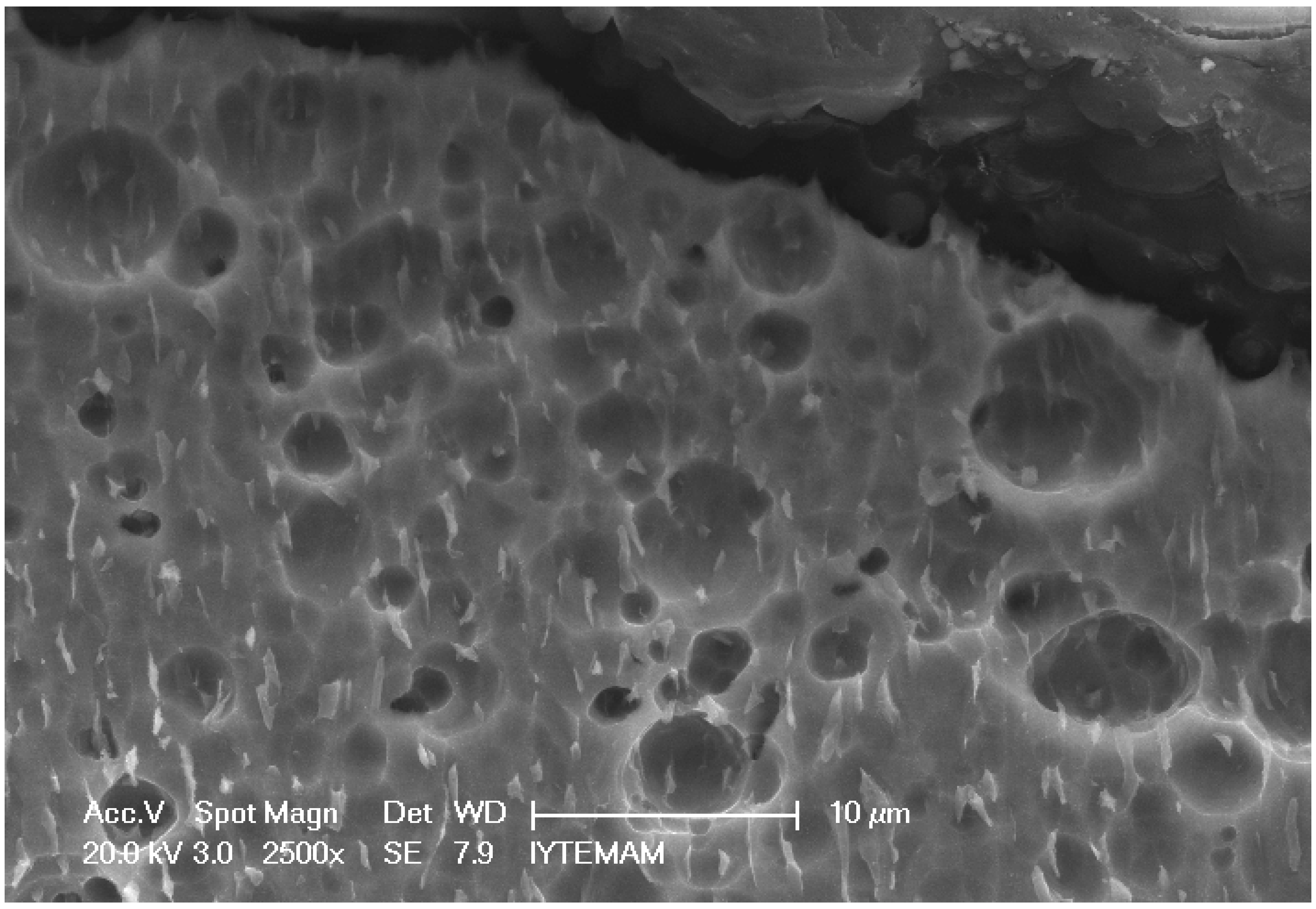

Figure 6.31. Quasi Static test specimen side view at 2500X magnification

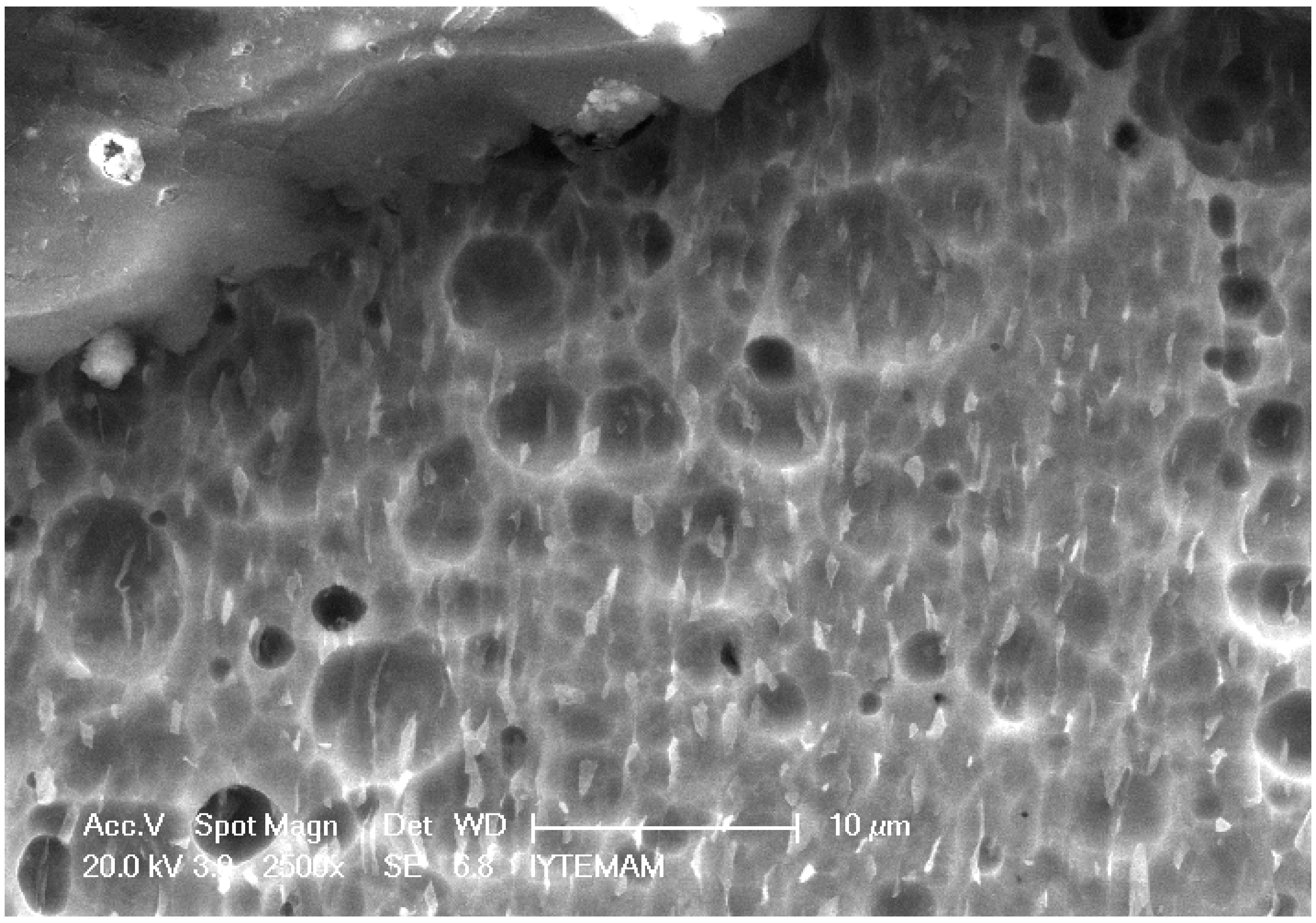

Figure 6.32. Dynamic tension test specimen side view at 2500X magnification

Figures 6.29 and Figure 6.30 show the cracks in the tested static and dynamic compression test specimens, respectively. In general the failure mechanisms of metals prove that shear banding is one the major fracture mode. The large strains cause the formation of bands where the shear is localized intensively. These bands are important for the fracture mechanism because in the zone cracks and voids initiate and propagate. The thickness of the shear band in dynamically tested samples is about 15µm (Figure 6.31). After metallographic examination Vickers hardness tests are applied to determine the change in hardness around the shear band. The hardness tests are applied to the three different regions in compression test specimen; shear band (SB), near shear band (near) and far to the shear band (far). The hardness values are tabulated in Table 6.9 includes the hardness test results of three regions. The reduced hardness values in the band signals the softening of the material in the band.

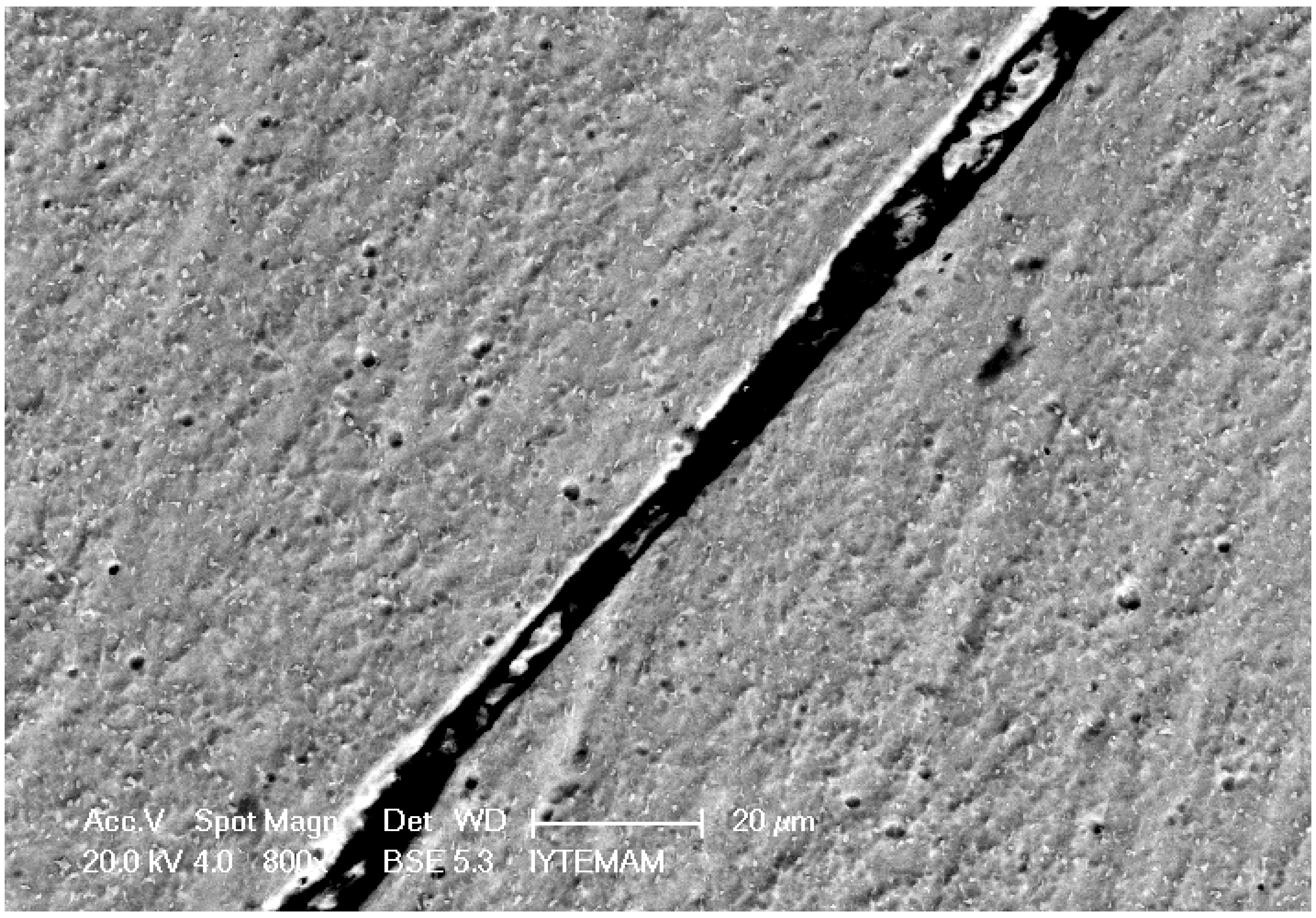

Figure 6.33. Crack inside the quasi-static compression test specimen

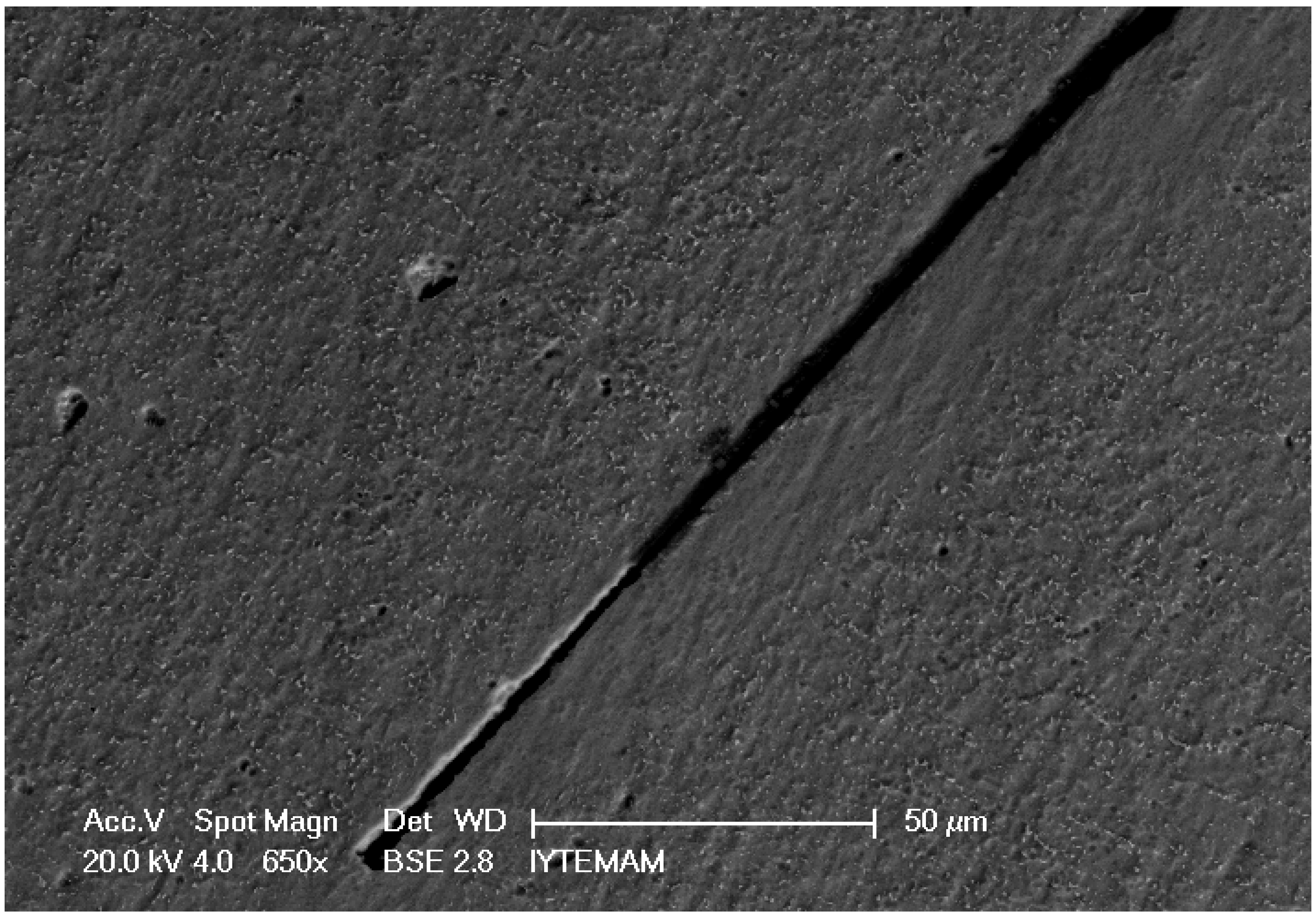

Figure 6.34. Crack inside the dynamic compression test specimen

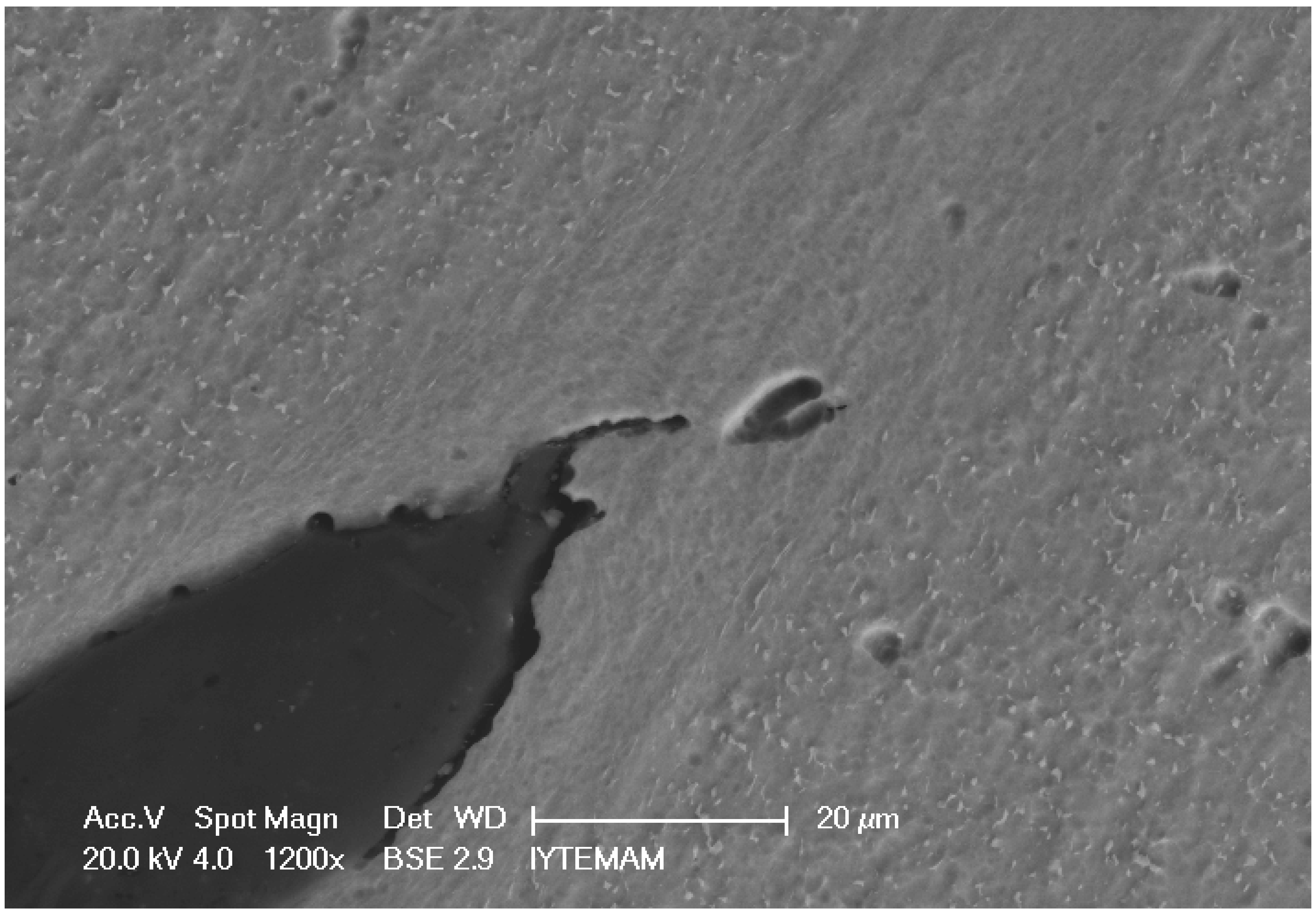

Figure 6.35. Crack inside the dynamic compression test specimen

Table 6.7. The hardness test results of three regions

	STATIC SPECIMEN			DYNAMIC SPECIMEN		
	A.S.B.	NEAR	FAR	A.S.B.	NEAR	FAR
1	244	324	351	287	349	361
2	230	316	341	281	353	362
3	263	335	344	276	349	356
MEAN	246	325	345	281	351	360
STD. DEV. (%)	12.52	9.54	5.13	5.51	4.04	3.21
COEFF. OF VAR.	3.65	2.94	1.49	1.96	1.15	0.89

6.4. JC Model Analysis and Comparison with the Literature

Such important properties including high strength to weight ratio, low density and corrosion resistance tend to increases the use of Ti6Al4V alloy gradually, especially in the biomedical and aerospace industry. For the design purposes of this alloy in the structural applications, to define the mechanical behavior in terms of constitutive relations is needed. Studies were previously performed on Ti6Al4V alloy to understand its behavior under quasi-static and dynamic loading conditions at different strain rates and temperatures. Nasser (Nemat-Nasser, et al. 2001) investigated the effect of strain rate, temperature and microstructure on the mechanical properties Ti6Al4V alloy produced by three different processes. These alloys were commercial Ti6Al4V (MIL-T-9047G), RS-MIL-HIP (hot isostatic pressed) and RS-HIP. Commercial alloy specimens annealed at 748 ^{o}C for one hour in a vacuum approximately at 10^{-5} Torr, and air-cooled to room temperature. The other two alloys were produced with powder metallurgy. Experimental results showed that RS-MIL-HIP Ti6Al4V alloy had higher flow strength. The flow stresses of the alloys tested were found to be, however, more sensitive to the temperature than the strain rate. The microscopical examinations also showed that the microstructure differences affected the initial yield stress and the athermal part of the flow stress. Adiabatic shear bands and associated fractures were found as the main failure characteristics of the Ti6Al4V alloy at low temperatures and high strain rates, which was fully agreed with the present work. Khan (Khan, et al. 2004) also developed the J-C parameters of the commercial Ti6Al4V alloy using the test results of Nasser. Lee (Lee and Lin 1998) investigated the flow properties of Ti6Al4V alloy at high temperature and high strain rate. The titanium alloy used in this study was extruded below the transition temperature and annealed for 1 hour at 760 ^{o}C. The results of experiments proved that the flow behavior of Ti6Al4V alloy was sensitive to the temperature and temperature sensitivity increased with increasing true strain. The results of the failure analysis also proved that shear bands were the sites where the fracture occurred. The microstructural examination of the deformed specimens indicated that the dislocation density linearly decreased with temperature. The dislocation cell size increased with temperature and decreased with dislocation density. As a result of microscopic examinations, an inverse relation between flow stress and dislocation cell size was obtained. Lastly, the JC material model parameters were determined. Seo (Seo, et al. 2005) investigated high temperature and strain rate deformation behavior of a Ti6Al4V alloy (AMS 4928N HEAT 579L) used as airplane turbine blade. Specimen with dimensions of 8mm in length and 8mm in diameter were used for tests. Dynamic tests were performed with high temperature Split Hopkinson pressure bar. The true stress-strain relations at a strain rate of 1400 s^{-1} were determined from room temperature to 1000 ^{o}C at intervals of 200 ^{o}C. As the temperature increased the flow stress and strain hardening parameter decreased. JC material model was determined. Similar study performed by Khan et al. with Ti6Al4V alloy. The chemical composition of the alloy used in this study shown in the table. The alloy used in this study has hexagonal close packed crystalline structure. Macdougall and Harding (Khan, et al. 2004) determined JC parameters of a Ti6Al4V alloy using . torsion stress data extracted and converted to von Mises effective stress and plastic strain. Lawrence Livermore National Laboratory reported the deformation and failure behavior of a Ti6Al4V alloy. The Ti6Al4V alloy investigated was annealed at 790 ^{o}C for one hour and cooled in a furnace. Both compression and tension tests were applied at high strain rate tests. The data from the existent literature were used for the determination and verification of the JC model. The relation between shear band, shear localization and failure of the sample was explained. The parameters of the JC material and damage model were defined.

Based on the above literature survey, JC flow stress and damage model parameters of the previous studied are listed sequentially in Tables 7.1 and 7.2 together with present study results. For comparison, the reference strain rate of the studies listed in Table 7.1 converted into 1 s^{-1} and JC parameters recalculated. The JC parameters listed in these tables differ from each other. The difference is attributed to the differences in the microstructure of the same alloy tested. However, the strain rate sensitivity parameter of the JC model, c, is found to be very similar. The values of c range between 0.013-0.028. The values c in the present study is lower in compression and this is basically a result of large strain involved in compression which hides the effect of strain rate. While the c parameter obtained in tension show good agreement with values obtained in previous studies. It should also be noted that the tested Ti6Al4V alloy is a biomedical grade alloy as it contains very low level of interstitial elements. This result in an increased ductility when compared with commercial alloys tested in the literature.

Table 6.8. JC material model parameters defined as a result of different studies

	A(MPa)	B(MPa)	n	c	m
Khan, et al. (with optimization)	1104	1036	0.6349	0.01390	0.7794
Khan, et al. (without optimization)	1080	1007	0.5975	0.01304	0.7701
Nasser, et al.	1119	838.6	0.4734	0.01921	0.6437
Macdougall and Harding	984.0	520.3	0.5102	0.015	0.8242
Lee, et al.	782.7	498.4	0.28	0.028	1.0
Seo, et al.	997.9	653.1	0.45	0.0198	0.7
Lawrence Livermore National Laboratory	1098	1092	0.93	0.014	1.1
Present study, tension	1062	1317.3	0.7392	0.015	0.965
Present study, compression	982.5	1218.9	0.8674	0.00824	0.965

Table 6.9. JC damage parameters defined as a result of different studies

Study	D_1	D_2	D_3	D_4	D_5
Lawrence Livermore National Laboratory	-0.09	0.25	-0.50	0.014	3.87
Our study	0.294	8.63	-8.4	-0.0213	4.22

CHAPTER 7

CONCLUSION

In the present work, the JC flow stress and damage parameters of a biomedical grade Ti6Al4V alloy that contained very low levels of interstitial elements were determined for the modeling its deformation in the CWR process. Despite the existence of the material parameters of the alloy in the literature, this study provided the material property data for the first time for a biomedical grade alloy. The JC models were determined through quasi-static (10^{-3}- 0.1 s^{-1}) and high strain rates (300-1000 s^{-1}) within the temperature range of 25-1150 ^{o}C. High strain rate tests were performed using both compression and tension SHPB testing devices. The damage model was determined using notched specimens of different stress triaxiality. Based on the results the followings may be concluded.

1. The tested alloy flow stresses were found to increase with increasing strain rate for both compression and tension tests. This was proved that the alloy has a strain rate sensitive flow stress behavior.
2. At increasing strain rates the failure strains in tension decreased. The reduced fracture strain was also confirmed by the microscopic observations. In statically tested samples the ductile fracture mode was composed of smaller but deeper dimples, while the dimples were observed to be shallow and larger in dynamically tested samples. The cup region of the cup-cone type fracture was also wider in statically tested samples.
3. The tensile fracture presumably started in α region and the β phase microscopically shown to deform plastically through the tensile axis.
4. The compression failure mode of the alloy was found to be resulting from the shear band formation followed by the fracture of the shear band. This failure mode was also found to be valid both statically and dynamically tested samples. The size of the shear band was measured to be 15 μm in the samples tested dynamically. The material in the shear band was also shown to be softer.

5. High temperature test conducted at quasi-static strain rate showed that the stress values decreased greatly after about 800 ^{o}C due to α ->β transformation. Due to this two differ tent JC material models valid between 25-600 ^{o}C and 800-1150 ^{o}C were developed.
6. The determined JC parameters were found to be well agreed with the literature except the model obtained from the compression tests. The reduced strain rate sensitivity parameter of the model in compression was attribute to adiabatic heating of the samples which hided the strain rate sensitivity.

REFERENCES

Akhtar S. Khan, Yeong Sung Suh, Rehan Kazmi. 2004. Quasi-static and dynamic modeling responses and constitutive modelling of titanium alloys. *International Journal of Plasticity* 20:2233-2248.

Bancroft, D. 1941. The velocity of Longitudinal Waves in Cylindrical Bars. *Physical Review* 59:588-593.

Bertholf, L.D.a.K.C.H. 1975. Two Dimensional Analysis of the Split Hopkinson Pressure Bar System. *J. Mech. Phys. Solids* 23:1-19.

G. Lütjering, J.C.W. 1993. *Engineering Materials and Processes. 2nd edition ed. Titanium*, P.B. Derby: Springer.

Gorham, D.A.a.W., X.J. 1996. An Emprical Method For Correction Dispersion in Pressure Bar Measurement of Impact Stresses. *Measurement Science and Technology* 7:1227-1232.

Johnson, T.J.H.a.G.R. 1991. Determination of constants and comparison of results for various constitutive models. *Journal de Physique* 111, Vol. 1.

Jutras, M. 2008. Improvement of the characterisation method of the Johnson-Cook Model, in M´ emoire pr´ esent´ e` alaFacult´ edes´ etudes sup´ erieures de l'Universit´ eLaval dans le cadre du programme de maˆ ıtrise Maˆ ıtrise en g´ enie m´ ecanique pour l'obtention du grade de Maˆ ıtre ` es Sciences (M.Sc.)., Facult´ e Des Sciences Et De G´ Enie Unıversit´ E Laval Qu´ Ebec.

K. H. Jürgen Buschow, R.W.C., Merton C. Flemings, Bernard Ilschner (print), Edward J. Kramer, Subhash Mahajan, and Patrick Veyssière (updates). 2008. *Encyclopedia of Materials : Science and Technology, in Plastic Deformation: Constitutive Description.*

Lesuer, D.R. 2000. Experimental Investigations of Material Models for Ti-6Al-4V Titanium and 2024-T3 Aluminum, in The Federal Aviation Administration William J. Hughes Technical Center COTR is William C. Emmerling

Li Q, L.M., Deng Z. 2001. Analysis of internal slip in a two-roll cross wedge rolling process. *Trans NAMRI*:9–16. Liechti, A.B.K.M. 2001. *Mechanics of Materials: Pearson Prentice Hall.*

Lindholm, U.S..Yeakley., L.M. 1968. High Strain Rate Testing: Tension and Compression. *Experimental Mechanics* 8:1-4.

Ling, Y. 1996. Uniaxial True Stress-Strain after Necking. *AMP Journal of Technology*.

Love, A.E.H. 1944. A treatise on the mathematical theory of elasticity. *Dover Publications*: 428.

M.Vanderhasten, L.Rabet and B.Verlinde. 2005. AME High Temperature deformation of Ti6Al4V at low strain rates. 195-200.

Mackerle, J. 2005. Finite element modelling and simulating of bulk material forming. *Computer-Aided Engineering and software* 23.

Minting Wang, X.L., Fengshan Du, Yangzeng Zheng. 2005. A coupled thermal–mechanical and microstructural simulation of the cross wedge rolling process and experimental verification. *Material Science & Engineering* 391:305–312.

Nazia Tasneem. 2002. Study of wave shaping techniques of Split Hopkinson Pressure Bar using finite element analysis. Thesis by Nazia Tasneem, Osmania University.

Pater, Z. 2006. Finite element analysis of cross wedge rolling. *Material Processing Technology* 173: 201–208.

P. F. Bariani, G.B., S. 2001. Corazza, Enhancing performances of SHPB for determination of flow curves. *Manufacturing Technology* 50:153-156.

Pochhammer, L. 1876. Über die Fortpflanzungsgeschwindigkeiten kleiner Schwingungen in einem unbegrenzten istropen Kreiszylinder. *J. reine angew. Math* 81:324-336.

Qiang Li, Michael Lovell. 2007. Cross wedge rolling failure mechanism and industria application. *Int. J Adv. Manuf Technology* 37:265-278.

Qiang Li, M.R.L., William Slaughtera, Kaveh Tagavib. 2002. Investigation of the morphology of internal defects in cross wedge rolling. *Jourmal of material processing Technology* 125–126, 248–257.

Qiang Li, Michael R. Lovell. 2004. The establishment of a failure criterion in cross wedge rolling. *Int. J Adv. Manuf Technology* 24: 180–189.

Shu Xuedao, L.C., Zhao Jing, Hu Zhenghuan. 2007. Theoretical and experimental study of varying rule of rolling-moment about cross-wedge rolling. *Material Processing Technology* 187–188, 752–756.

Sia Nemat-Nasser, Wei-Guo Guo, Vitali F. Nesterenko,S.S Indrakanti, Ya-Bei Gu. 2001. Dynamic response of conventional and hot isostatically pressed Ti-6Al-4V alloys: experiments and modeling. *Mechanics of Materials* 33:425-439.

Songwon Seo, Oakkey Min, Hyumno Yang. 2005. Constitutive equation for Ti-6Al-4V at high temperatures mesured using the SHPB technique. *International Journal of Impact Engineering* 31:735-754.

William D. Callister, J. 2003. Material Science and Engineering An Introduction. *Sixth Edition ed.: John Wiley & Sons, Inc.*

Woei-Shyan Lee, Chi-Feng Lin. 1998. High-temperature deformation behaviour of Ti6Al4V alloy evaluated by high strain rate compression tests. *Journal of Material Processing Technology* 75:127-136.

Yamion Dong, Michael Lovell., Kaveh Tagavi. 1998. Analysis of interfacial slip in cross-wedge rolling: an experimentally verified finite-element model. *Material Processing Technology*.

Yamion Dong, Kaveh A.Tagavi., Michael R. Lovell, Zhi Deng. 2000. Analysis of stress in cross wedge rolling with application to failure. *Mechanical Science* 1233-1253.

Yamion Dong, Kaveh A.Tagavi, Michael R. Lovell. 1998. Analysis of interfacial slip in cross-wedge rolling: a numerical and phenomenological investigation. *Material Processing Technology*.

Yingbin Bao , T.W. 2005. On the cut-off value of negative triaxiality for fracture. *Engineering Fracture Mechanics* 72:1049–1069.

Ying Fu Qiang, Pan Bo Song. 2007. Analysis on temperature distribution in cross wedge rolling process with finite element method. *Journal of Materials Processing Technology* 187–188, 392–396.

Z. Pater , A.G., W. Wero´nski. 2006. Cross-wedge rolling by means of one flat wedge and two shaped rolls. *Material Processing Technology* 177:550–554.